CHAOTIC ELECTRON TRANSPORT IN SEMICONDUCTOR DEVICES

by

WILLIAM CHRISTIAN SCANNELL

A DISSERTATION

Presented to the Department of Physics
and the Graduate School of the University of Oregon
in partial fulfillment of the requirements
for the degree of
Doctor of Philosophy

June 2010

University of Oregon Graduate School

Confirmation of Approval and Acceptance of Dissertation prepared by:

William Scannell

Title:

"Chaotic Electron Transport in Semiconductor Devices"

This dissertation has been accepted and approved in partial fulfillment of the requirements for the Doctor of Philosophy degree in the Department of Physics by:

Stephen Kevan, Chairperson, Physics
Richard Taylor, Advisor, Physics
Robert Zimmerman, Member, Physics
Stephen Gregory, Member, Physics
David Johnson, Outside Member, Chemistry

and Richard Linton, Vice President for Research and Graduate Studies/Dean of the Graduate School for the University of Oregon.

June 14, 2010

Original approval signatures are on file with the Graduate School and the University of Oregon Libraries.

An Abstract of the Dissertation of

William Christian Scannell   for the degree of   Doctor of Philosophy

in the Department of Physics   to be taken   June 2010

Title: CHAOTIC ELECTRON TRANSPORT IN SEMICONDUCTOR

DEVICES

Approved: _____

Dr. Richard P. Taylor

The field of quantum chaos investigates the quantum mechanical behavior of

classically chaotic systems. This dissertation begins by describing an experiment

conducted on an apparatus constructed to represent a three dimensional analog of a

classically chaotic system. Patterns of reflected light are shown to produce fractals,

and the behavior of the fractal dimension D_F is shown to depend on the light's ability

to escape the apparatus.

The classically chaotic system is then used to investigate the conductance properties

of semiconductor heterostructures engineered to produce a conducting plane relatively

free of impurities and defects. Introducing walls that inhibit conduction to partition

off sections considerably smaller than the mean distance between impurities defines

devices called 'billiards'. Cooling to low temperatures enables the electrons traveling

through the billiard to maintain quantum mechanical phase. Exposure to a changing electric or magnetic field alters the electron's phase, leading to fluctuations in the conductance through the billiard. Magnetoconductance fluctuations in billiards have previously been shown to be fractal. This behavior has been charted using an empirical parameter, Q, that is a measure of the resolution of the energy levels within the billiard. The relationship with Q is shown to extend beyond the ballistic regime into the 'quasi-ballistic' and 'diffusive' regimes, characterized by having defects within the conduction plane.

A model analogous to the classically chaotic system is proposed as the origin of the fractal conductance fluctuations. This model is shown to be consistent with experiment and to account for changes of fine scale features in MCF known to occur when a billiard is brought to room temperature between low temperature measurements.

An experiment is conducted in which fractal conductance fluctuations (FCF) are produced by exposing a billiard to a changing electric field. Comparison of D_F values of FCF produced by electric fields is made to FCF produced by magnetic fields. FCF with high D_F values are shown to de-correlate at smaller increments of field than the FCF with lower D_F values. This indicates that FCF may be used as a novel sensor of external fields, so the response of FCF to high bias voltages is investigated.

CURRICULUM VITAE

NAME OF AUTHOR: William Christian Scannell

PLACE OF BIRTH: Thousand Oaks, California

DATE OF BIRTH: September 11, 1970

GRADUATE AND UNDERGRADUATE SCHOOLS ATTENDED:

> University of Oregon, Eugene, Oregon
> California State University Fresno, Fresno, California
> Cal Poly San Luis Obispo, San Luis Obispo, California
> Moorpark College, Moorpark, California

DEGREES AWARDED:

> Doctor of Philosophy in Physics, 2010, University of Oregon
> Master of Science in Physics, 2004, University of Oregon
> Bachelor of Arts in Physics, 2002, University of Oregon
> Associate in Arts in Physics, 1991, Moorpark College

AREAS OF SPECIAL INTEREST:

> Quantum Chaos in Nanoscale Devices
> Electron Transport in Solid State Devices
> Physics Education

PROFESSIONAL EXPERIENCE:

> Graduate Research Assistant,
>   University of Oregon, 2003 – 2009
> Graduate Teaching Fellow,
>   University of Oregon, 2002 – 2003

GRANTS, AWARDS AND HONORS:

NSF GK12 Fellowship, University of Oregon, 2003/2004

NSF GK12 Fellowship, University of Oregon, 2004/2005

NSF GK12 Fellowship, University of Oregon, 2005/2006

NSF GK12 Fellowship, University of Oregon, 2007/2008

Departmental Honors, University of Oregon, 2002

Student Athlete of the Year, Moorpark College, 1991

Academic All American, Moorpark College, Wrestling, 1991

PUBLICATIONS:

M.S.Fairbanks, T. P. Martin, **B.C. Scannell**, C. A. Marlow, H. Linke, R. P. Taylor
Measuring hybridization in GaINAs/InP electron billiard arrays
Submitted to *Physica E* (August 2009)

M.S.Fairbanks, **B.C. Scannell**, T. P. Martin, R. Montgomery, S. A. Brown, R. P. Taylor
Toward chaotic electron transort in bismuth nanocluster wires
Submitted to *Physica E* (August 2009)

T. P. Martin, M. S. Fairbanks, **B. C. Scannell**, C. A. Marlow, H. Linke, and R. P. Taylor
Investigation of electronic wavefunction hybridization in $Ga_{0.25}In_{0.75}As/InP$ arrays
Submitted to *Applied Physics Letters* (August 2009)

B C Scannell, B Van Dusen and R P Taylor
An Optical Demonstration of Fractal Geometry
Bridges Banff conference proceedings 2009 Tarquin Books

R.P.Taylor   T.P.Martin,   A.P.Micolich,   D.Jonas,   C.Boydston,
B.C.Scannell, M.Calverley
Fractal Analysis of Rorschach Inkblots
Submitted to *Leonardo* 2009

M.S.Fairbanks, T. P. Martin, C. A. Marlow, **B. C. Scannell**,
S.A.Brown, R.P.Taylor
Chaotic Electronic Transport in Nonocluster Wires
http://meetings.aps.org/link/BAPS.2009.MAR.C1.182

M.S. Fairbanks, G.J. Kearns, **B.C. Scannell**, A Loftus, R.P.Taylor,
J.E. Hutchinson
**Electron   Transport   in   Quasi-1D,   DNA-Templated
Nanoparticle Arrays**
http://meetings.aps.org/link/BAPS.2009.MAR.Q36.9

T.P. Martin, C.A. Marlow, **B.C. Scannell**, M.S. Fairbanks, H. Linke,
S.A. Brown, R.P.Taylor
**Chaotic Scattering in nano-electronic systems: from
billiards to clusters**
International Journal of Nanotechnology **6** No.3/4 2009

B.C. Scannell, T.P. Martin, M.S. Fairbanks, H. Linke, C.A. Marlow,
T.M. Fromhold, C.V. Brown, K. Ishibashi and R.P. Taylor
**Quantum Conductance Fluctuations in Semiconductor
Devices**
Current Applied Physics, Volume 8, Issues 3-4, May 2008, Pages
332-335

A.P. Micolich, **B.C. Scannell**, M.S. Fairbanks, T.P. Martin, and R.P.
Taylor
**Comment on Drip Paintings and Fractal Analysis
by K. Jones-Smith, H. Mathur and L.M. Krauss
(arXiv:0710.4917v2 [cond-mat.stat-mech])**
arXiv:0712.1652v1 [cond-mat.stat-mech] 2007

R.P. Taylor, R. Guzman, T.P. Martin, G.D.R. Hall, A.P. Micholich, D.
Jonas, **B.C. Scannell**, M.S. Fairbanks and C.M. Marlow
Authenticating Pollock Paintings Using Fractal Geometry
Pattern Recognition Letters, Volume 28, Issue 6, 15 April 2007, Pages
695-702

T.P.Martin, **B.C.Scannell**, M.S.Fairbanks, R.P.Taylor, A.P.Micolich, D.Jonas
Pollock's Patterns: Recent Developments
Fractals Research 2006 ISBN:0-9791874-2-7

T.P. Martin, **B.C. Scannell**, C.A. Marlow, R.P. Taylor, H. Linke, I. Shorubalko and L. Samuelson
Series Summation of Fractal Fluctuations in Electron Billiards
Physica E: Low-dimensional Systems and Nanostructures, Volume 34, Issues 1-2, August 2006, Pages 600-603

C.A. Marlow, R.P. Taylor, T.P. Martin, **B.C. Scannell**, H. Linke, M.S. Fairbanks, G.D.R. Hall, I Shorubalko, L. Samuelson, T.M. Fromhold, C.V. Brown, B. Hackens, S. Faniel, C. Gustin, V. Bayot, X. Wallart, S. Bollaert and A. Cappy
Unified Model of Fractal Conductance Fluctuations for Diffusive and Basllistic Semiconductor Devices
Physical Review B Volume 73, 195318, May 2006

ACKNOWLEDGEMENTS

To begin, I would like to thank my advisor, Dr. Richard Taylor, without his patience, advice and expertise this work would not have been possible. His wide range of interests enabled me to learn far more about the world we live in than I would have imagined possible. I would also like to thank my committee, Dr. Steve Kevan, Dr. Steve Gregory, Dr. Robert Zimmerman, and Dr. David Johnson for their support, feedback and availability throughout this work. Additionally, there are four men who have been both excellent mentors, and become even better friends: Dr. Dan Deponte (who is no ordinary genius), Stan Micklavzina (who taught me physics demonstrations could be much more than 'edutainment'), "The magnificent, wonderful yet humble" Don Fiel and "Shopper" Bob Weiss. Dean Livelybrooks, Catherine Hayden and Anae Rosenburg and their work with the NSF GK-12 program provided a very rewarding experience. In addition to his work in setting up our lab, as well as providing many fruitful discussions, I'd like to thank Dr. Adam Micolich for providing the data sets on the undoped billiard system.

Dr. Colleen Marlow and Dr. Ted Martin, both helped to " show me the ropes" of low temperature physics experimentation. Significant thanks go out to Dr. Matt Fairbanks, who has been a wonderful friend and an excellent research collaborator, spending many long hours in the lab and putting up with my 'off-color' and perhaps

To Gretchen...

TABLE OF CONTENTS

LIST OF FIGURES

LIST OF TABLES

CHAPTER I

INTRODUCTION

Introduction

In 1970 Ya.G. Sinai introduced an amazing dynamical system that has come to be known as the Sinai billiard.[1] The term billiard is used to describe the motion of a 'particle' traveling in a bounded region. The particle travels in straight line paths until reflecting off a boundary. Energy is conserved, and reflections are specular, in that the angle of reflection is equal to the angle of reflection. The Sinai billiard is composed of a square with central circle removed, thus the boundaries are the walls making up the square, and the circular scatterer. Sinai was able to show that this billiard was chaotic, meaning that a particles trajectory was critically sensitive to initial conditions.

The Sinai Cube experiment discussed later in this chapter was funded by the M.J. Murdock Foundation, Partners in Science Program, which provides high school science teachers the opportunity to work in a research laboratory and bring some of the knowledge gained back to the classroom. It was a great pleasure to work on this project with Ben Van Dusen who performed all of the ray tracing procedures discussed in that section.

Quantum chaos is the field that investigates the quantum mechanical dynamics of classically chaotic systems, such as the Sinai billiard. In that spirit this dissertation will begin with the description of an experiment in which a three dimensional analog of the Sinai billiard was constructed. In that experiment the *particles* are replaced with light. Light exhibits the properties of the theoretical particle of Sinai's billiard in that it travels in a straight path an undergoes specular reflection off of smooth, shiny surfaces. The resulting patterns are then analyzed and shown to reproduce themselves on increasingly small length scales, i.e. the patterns are *fractal.* Fractal patterns often emerge from systems that exhibit chaos, in fact, in 1988 Bleher *et al.* showed that providing two holes in which the particle could exit, or 'opening' the Sinai billiard resulted in phase space diagrams (velocity angle *vs.* position) that were fractal[2]. Prior to describing the experiment on the "Sinai Cube" this chapter provides some background information on fractal geometry, leading to another, more general link between chaos and perhaps the most famous fractal, the Mandelbrot set.

Chapter II describes the fabrication of mesoscopic billiards defined on semiconducting heterostructures, as well as the experrimental apparatus used to make measurments. The term mesoscopic refers to size scales that are large compared to atomic size scales, such as the Bohr radius, yet quite small compared to macroscopic length scales, such as a baseball. The de Broglie wavelength of the elctrons traversing these billiards is much smaller that the billiard dimensions, so the electron transport will be treated semi classically. That chapter concludes with some of the background

physics necessary for analysis, as well as the technique used to determine the fractal dimension, D_F, that is used to characterize the fractal conductance fluctuations, FCF, that result when the billiard is exposed to a varying external magnetic field.

In Chapter III the quantum chaos of the Sinai billiard is investigated, followed by the introduction of an empirical parameter Q, which is a measure of the energy level resolution within a billiard. The relationship of the fractal scaling to Q is then shown to extend beyond the ballistic regime (i.e. billiards) into the quasi-ballistic and diffusive regimes, in which at least one of the device dimensions is smaller than the typical distance between material impurities. Extension to the quasi-ballistic regime utilized data provided by Dr. J.P. Bird. Data for the diffusive regimes was measured and provided by Dr. K. Ishibashi, Dr. C.V Brown, and Dr. R.P. Taylor. That chapter also introduces a model in which material impurities, including remote ionized donors act analogously to the Sinai billiard and are the origins of the observed FCF.

Chapter IV describes an experiment designed to test the model described in Ch. III. In that experiment the billiard is brought to an intermediate temperature T_i between electronic measurements of magnetoconductance fluctuations (MCF).[1]

Chapter V describes an experiment in which FCF are produced by exposure to a varying an external electric field. The sensitivity of the FCF to both electric and magnetic fields is compared, and it is shown that the FCF with high values of D_F

---

[1]The term MCF is used to indicate that the FCF have been produced by an external magnetic field. In that sense the MCF are a subset of FCF.

de-correlate at smaller increments of applied field, and thus are more sensitive to external fields than the FCF with lower values of D. That chapter then charts the effects of applying relatively large bias voltages to a billiard.

Chapter VI provides some concluding remarks, including discussion about a new heterostructure our collaborators in Sydney, Australia have recently developed. Magnetic Field sweeps taken by Dr. Adam Micolich's group were provide to us for fractal analysis. This chapter discusses the predictions of the model described in Ch.III on these data sets and presents the results of that analysis.

<u>Fractal Dimension</u>

Nature abounds with fractal scaling patterns. Few would contest Mandelbrots classic argument *"Clouds are not spheres, mountains are not cones, coastlines are not circles, and bark is not smooth, nor does lightning travel in a straight line"*[3]. Today, researchers find fractal geometry a useful description of a wide variety of phenomena, as anyone can verify on the internet within a few minutes using their favorite search engine. One is likely to find a variety of subjects using fractal geometry to describe anything from pulmonary vessels to river systems to a wide range of artwork.

Often when one thinks of fractals, however, the images that come to mind are those of exact fractals, in which the pattern is exactly repeated at increasingly fine length scales. Such patterns generated by repetitive application of mathematical formulae. With the use of computer simulations, truly beautiful images can be generated. Two

canonical examples of these iteratively generated exact fractals are the Koch snowflake

and the Sierpinski gasket. In the case of the Koch snowflake, a line segment is divided

into thirds. The middle third of the line is replaced by two equal length segments

angled to form the top of an equilateral triangle. In the next iteration of this process

each of the 4 new segments is replaced by a 1/3 replica of the parent segment according

to the same procedure [4]. At each iteration step the overall length of the curve is

increased by a factor of 4/3. This curve can be characterized by the fractal dimension,

D_F, as follows.

If one takes a line segment and chops it into N identical length segments L, the

line is reduced by the scaling factor $L = 1/N$. If one similarly segments a square,

the scaling factor can be described by $L = 1/\sqrt{N}$, for a cube the analogous process

yields $L = 1/\sqrt[3]{N}$. This this expression can be generalized to a D dimensional object

by the expression $L = 1/\sqrt[D]{N}$. Thus, each of the N copies of the have a length L and

there are $N = 1/L^D = L^{-D}$ segments of the original object. This gives the fractal

dimension of self similar objects as $D_F = \log(N)/\log(1/L)$. For the Koch snowflake,

there are 4 copies scaled down by a factor of 1/3 giving $D_F = \log(4)/\log(3) \approx 1.26$.

A similar process can be used to generate the Siepinski gasket. Starting with an

equilateral triangle, cut out an inverted triangle that has been scaled down by a

factor of $L = 1/2$ leaving $N = 3$ smaller copies of the original triangle. Thus for the

Sierpinski gasket $D_F = \log(3)/\log(2) \approx 1.58$. Objects well described by Euclidian

geometry will have integer values of D. For instance a straight line will have $D = 1$,

while a filled square will hold $D=2$. An object is said to be fractal if the quantity D_F

holds a non integer value. Fractals generated by such recursive processes are members

of a class of fractals known as Iterated Function Systems (IFS).
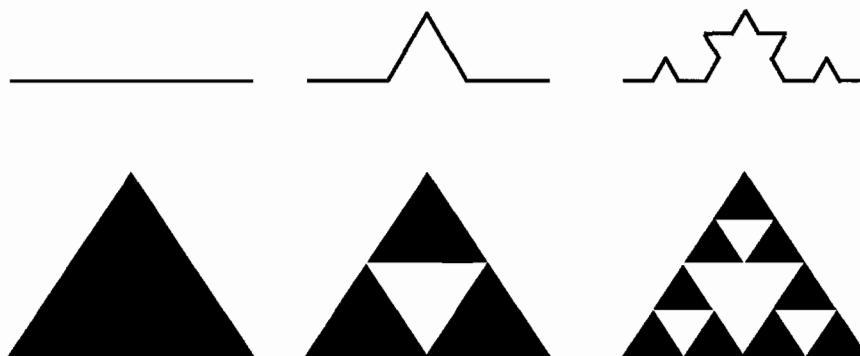
Figure 1.1. Three iterations of the Koch Snowflake and Sierpinski gasket. The starting point and first two iterations of the generation processes of the (top) Koch snowflake and (bottom) Sierpinski gasket.

Figure 1.1 shows the original 'seed' image (a line segment, and an equilateral

triangle) followed by the first two iterations of each of the Koch snowflake and the

Sierpinski gasket respectively. An intuitive feel for what D_F actually characterizes can

be rather difficult to grasp. One possible interpretation that works well for coastlines

or curves such as the Koch snowflake is that D_F can be viewed as a measure of the

crinkliness of the curve, or its lack of smoothness. This interpretation serves well for

as a description of D_F provided that it is the edges of a pattern that result in the

fractal scaling. But such a description is lacking an intuitive feel for filled patterns

such as the Sierpinski gasket.

While analytic determination of D_F is fitting, or at least possible, for fractals

generated via IFS, difficulty arises when one encounters a fractal produced by natural

processes. To estimate D_F for these processes, typically one employs the box counting procedure which is shown schematically in Fig. 1.2. In this procedure one superimposes a grid of squares (boxes) of length L on a two dimensional image of the object in question and counts the number of boxes that contain a piece of the object, N, represented as colored boxes in Fig. 1.2. The box size is then decreased and the counting of filled boxes is repeated until a suitably large range of L has been spanned. One can then produce a scaling plot in which $\log N$ is plotted as a function of $\log(1/L)$ and D is determined by the slope of the curve. In this scenario an object is said to be fractal if $1 < D_F < 2$, provided that the expression $N \propto L^{-D_F}$ holds for at least 1 order of magnitude.[5]

Fig. 1.3 shows an example of the scaling plots of the Sierpinski gasket and the Koch curve. When plotted in this manner, it is convenient to interpret the $\log(1/L)$ axis as describing the box size as ranging from coarse scaling, in which just a few boxes cover the image to fine scaling where the number of boxes necessary to cover the image becomes quite large.

In this way, one can picture the value of D_F as a measure of the relative amount of fine scale structure of the pattern. For instance, in Fig. 1.3 the Koch curve (bottom inset) does not seem to have as much complexity at fine scales as the Sierpinski gasket (top inset). The fact that the Sierpinski gasket fills more fine scale boxes is readily evident in that N is larger for the Sierpinski gasket than the Koch curve at the fine scale end of the plot while both curves are anchored at nearly the same coarse scale
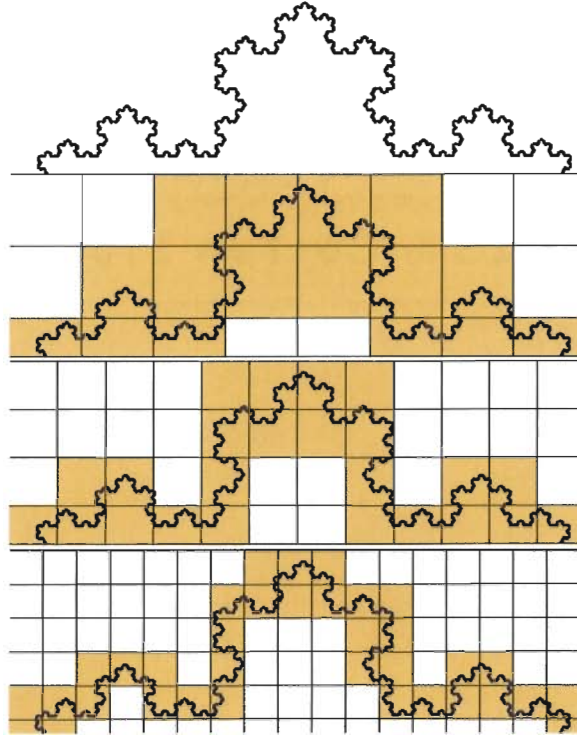
Figure 1.2. A schematic representation of the box-counting procedure used to determine D_F.

value. In some sense this implies that one can view D_F to be a measure of the ability

of the object to occupy space at fine scales.
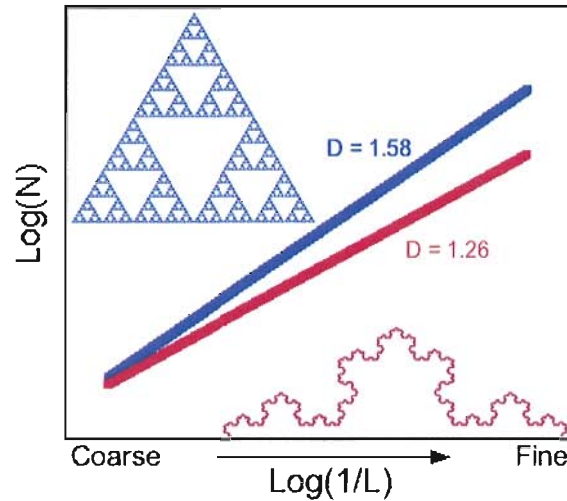
Figure 1.3. Scaling plots of the Koch snowflake and Sierpinski gasket. Scaling plots have been generated by the analytic value of the fractal dimension of the Sierpinsk gasket (top scaling plot with $D_F = 1.58$ and inset) and the Koch snowflake (bottom scaling plot with $D_F = 1.26$ and inset).

<u>The Mandelbrot Set</u>

The Iterated Function Systems in the previous section offer an appealing and straightforward description of the fractal dimension D_F. These also exhibit exact or strict self similarity, in that identical images are reproduced at various length scales. Such fractals are often referred to as classical or linear fractals. However, such a process is certainly not the only means of producing fractals. Probably the most famous fractal is that which was first observed by Benoit Mandelbrot in 1980 and has since become known as the Mandelbrot set. Illustrated in Fig. 1.4, this striking image is the result of a rather simple algorithm. This image was created using a modified version of Dr. Robert Zimmerman's code provided in Ref. [6].

Consider the expression $z_{i+1} = z_i^2 + c$ with $z_0 = 0$. The complex number c

is defined to be a member of the Mandelbrot set if and only if the sequence of values $z_0, z_1, z_2, \cdots$ remains bounded. The sequence of values $z_0, z_1, z_2, \cdots$ is called the *orbit* of z_0. Here is an example of a non-linear mapping that upon iteration produces a fractal. The Mandelbrot set exhibits both exact and statistical self similarity. Statistical self similarity occurs when the pattern follows the same statistical relationship at different length scales.

Near the so called Misiurewicz points, the pattern holds exact self similarity [4, 7]. This is illustrated in Fig. 1.5 where the image has been magnified around the two left hand buds. Misiurewicz points are defined as those values of c in which the initial point $z_0 = 0$ is *preperiodic*. In other words, the values $z_0, z_1, z_2, \cdots$ become bounded because they become traped in a periodic orbit that does not include the point $z_0 = 0$. A periodic orbit occurs when output of the iteration process repeats itself. For instance, suppose an iteration process produced the values $z_0, z_1, z_2, z_0, z_1, z_2, z_0, z_1, z_2, \cdots$ this process would be said to have a periodic orbit of period 3. As a simple example consider the value $c = -2$ and the first few iterations of the algorithm $z_{i+1} = z_i^2 + c$:

$$z_0 = 0$$

$$z_1 = z_0^2 + c = 0^2 + (-2) = -2$$

$$z_2 = (z_1)^2 + c = (-2)^2 - 2 = 2$$

$$z_3 = (z_2)^2 + c = (2)^2 - 2 = 2$$

This value of c is quickly placed on a rather trivial orbit of the value 2.
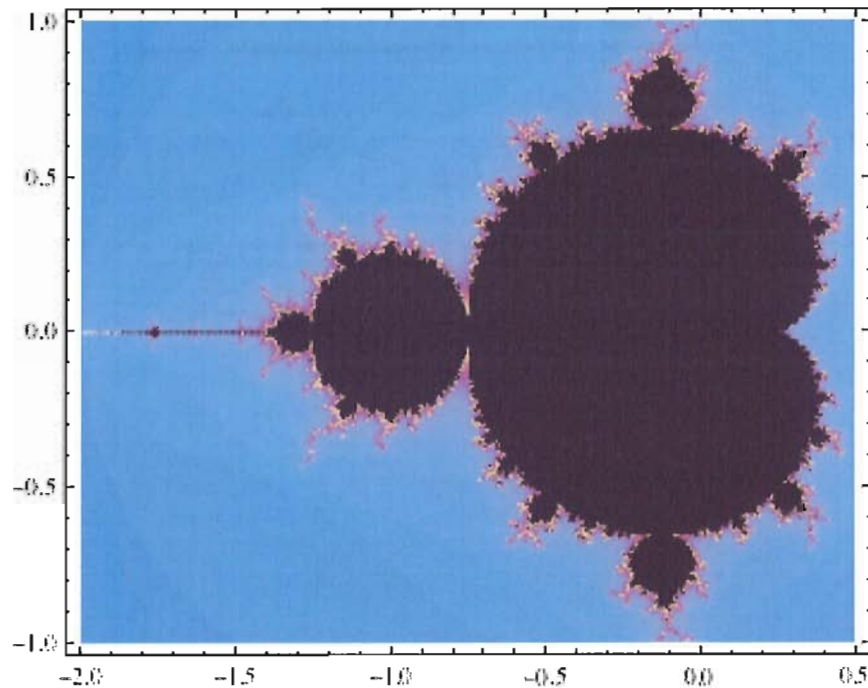
Figure 1.4. The Mandelbrot Set is the collection of points c lying in the complex plane which remain finite in the mapping of $z_{n+1} = z_n^2 + c$ with the starting point $z_0 = 0$
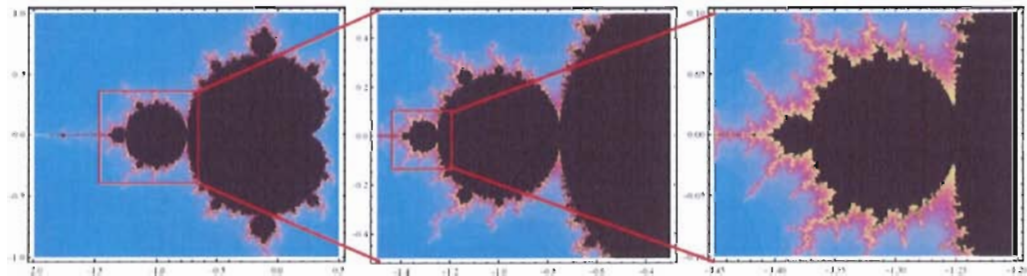
Figure 1.5. Magnification of the Mandelbrot set. Zooming in on the front two buds of the Mandelbrot set

Statistical self similarity of the Mandelbrot set can be seen if one zooms in near the region of $c = -0.75$, as illustrated in Fig. 1.6. There are many smaller copies of the buds. However, each copy is slightly different. Compare, for instance, the dendrites

extending off of the small buds on the left hand side of the valley to those on the right. Although these buds are similar, they are not exact copies, as the branching takes on different forms on each side of the central valley. The location of this valley is the transition point from the period 1 bud (main cardioid shaped bud at the very right) to the period 2 bud (boxed in the leftmost panel of Fig. 1.5). The associated period number is a measure of the number of points in a particular c's orbit around 0. For instance, consider the orbit of the choice $c = -1$.

$$z_0 = 0$$

$$z_1 = 0^2 - 1 = -1$$

$$z_2 = (-1)^2 - 1 = 0$$

$$z_3 = -1$$

The orbit oscillates between the points 0 and 1, it is said to be a period two orbit. Since this orbits around z_0 it is not preperiodic and thus is not a Misiurewicz point. This particular choice of c lies in the large bud just to the left of the large heart shaped area. In fact, all of the parameters c that lie in that region have orbits of period 2, similarly those choices of c that make up the heart shaped region are have orbits of period 1. Note that this region is essentially the same region that has been magnified in the central panel of Fig 1.5. This illustrates that, strictly speaking, the areas near the Misiurewicz are said to be *asymptotically* self similar. This simply means that the strict self similarity does not become readily apparent upon the first

magnification or rotation, but after a few iterations of the magnification and rotation in the neighborhood of these points, the set converges to one that is strictly self similar.
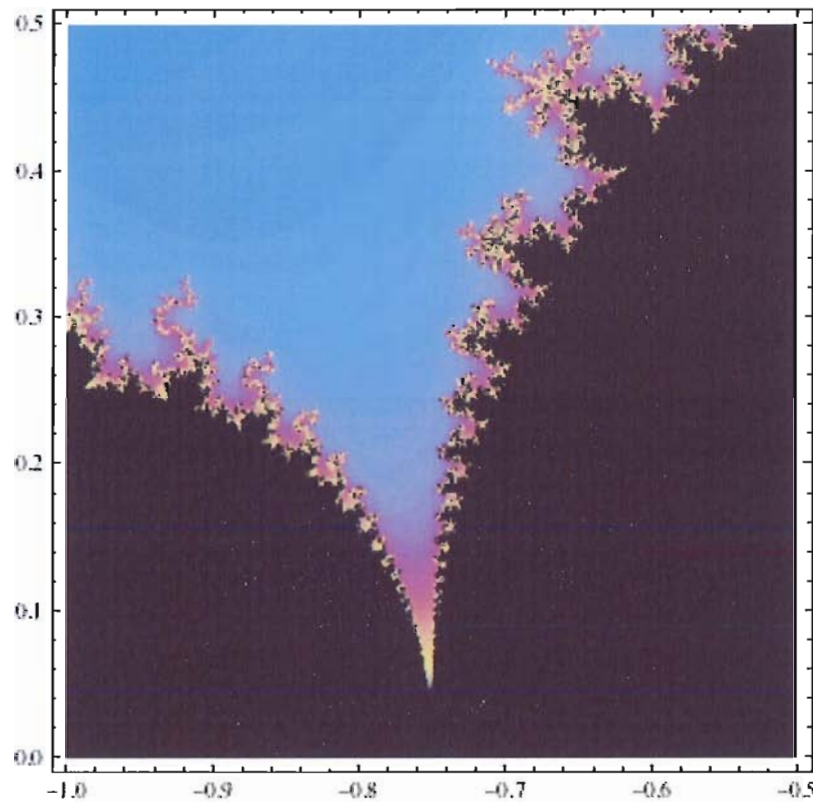
Figure 1.6. Magnification of the Mandelbrot set near $c = 0.75$ showing statistical self similarity

Chaos

Introducing the constraint that the coordinate z and parameter c be real valued provides a considerable amount of insight into the link between chaos and fractal geometry. A deterministic system is said to exhibit chaos if the long term behavior is both non periodic and critically dependent upon initial conditions [8]. Perhaps

$x \rightarrow x^2 + c$ for real values of x and c is the simplest example of non linear iteration. Figure 1.7 shows the first 50 iterations of this expression for values of c chosen as c =-1.1, -1.2, -1.3, and -1.7. For the value of $c = -1.1$, the orbit has period 2 from the onset. The choice of $c = -1.2$ also settles on an orbit of period 2 after a few transients, however, for $c = -1.3$, the orbit is of period 4. Finally, the choice of $c = -1.7$ reveals no pattern to the orbit, it is chaotic.
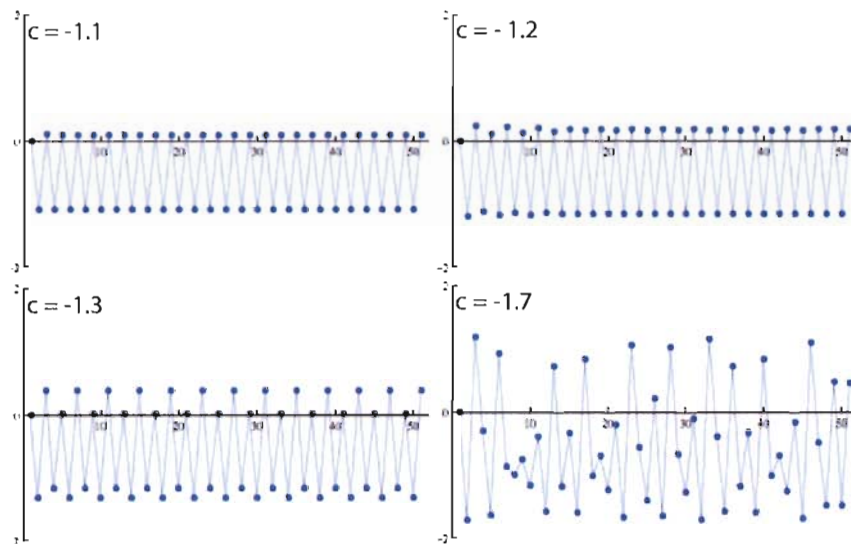
Figure 1.7. The first 50 iterations of the quadratic iterator $x_{n+1} = x_n + c$ plotted against iteration number for chosen values of c.

This raises an interesting question. What happens in the final state after all the transients, or temporary deviations, have died down? To visualize this, the first 100 values of the iteration are computed, and the transients are ignored by plotting only the last 25 points. Such a plot is called a final state diagram, and Fig. 1.8 is the final state diagram of the quadratic iterator $(x \rightarrow x^2 + c)$ for values of c ranging from -2 to 0.25. This plot is also often referred to as a bifurcation diagram, as it continually

divided into two branches. Notice the structure at $c \approx -0.75$. The plot splits into two branches, indicating the orbit has transitioned from period 1 to period 2. Each of these two branches split into two branches near $c \approx -1.25$, which themselves split into two more branches near $c \approx -1.35$. By the time c reaches the value of $c = -1.5$ the orbit has become chaotic and there does not appear to be any fixed number of clear branches.
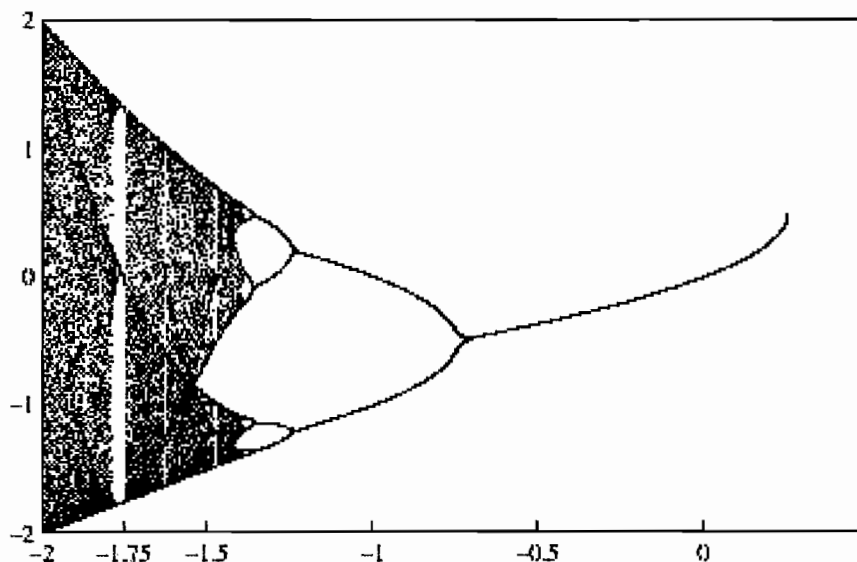
Figure 1.8.. Final state diagram of the quadratic iterator.

However, closer inspection the region $c \approx -1.8$ reveals that in the midst of this chaos, there is underlying order. In this plot, the first 1000 iterations were performed, and the last 250 have been plotted over the very small range of c. In fact, this real space analog of the Mandelbrot set provides a roadmap of the path from order to chaos. This fact would be interesting enough if it were limited to the relation of

the Mandelbrot set to the quadratic iterator. However, this path from order to chaos through sharp bifurcations can be found in many natural systems, with applications to systems ranging from biological to ecologic, to social sciences, to economic origins.[9–11]
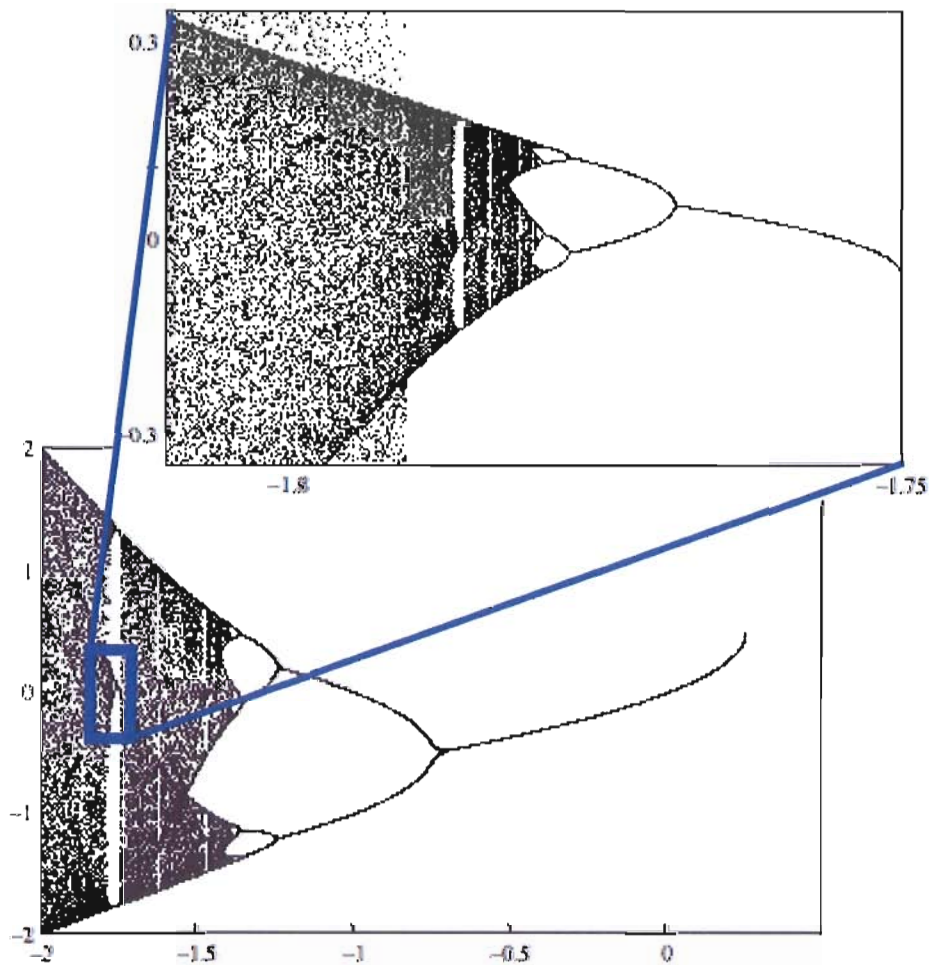
Figure 1.9. Magnification of the quadratic iterator final state diagram. The box indicates the region magnified in the upper right hand corner, revealing that, in the midst of chaos, there is underlying order.

This, of course, is not the whole story. Figure 1.10 shows the same bifurcation diagram directly above the Madelbrot set, aligned to match real values of the parameter

c. The location where the bifurcation diagram first splits into two branches is precisely where the large period 2 bud Mandelbrot set splits off from the main cardioid. In fact, all of the distinct features along the main axis (real c) of the Mandelbrot set can be associated with a bifurcation in the final state diagram. Thus the universal route from order to chaos is embedded in the Mandelbrot set.
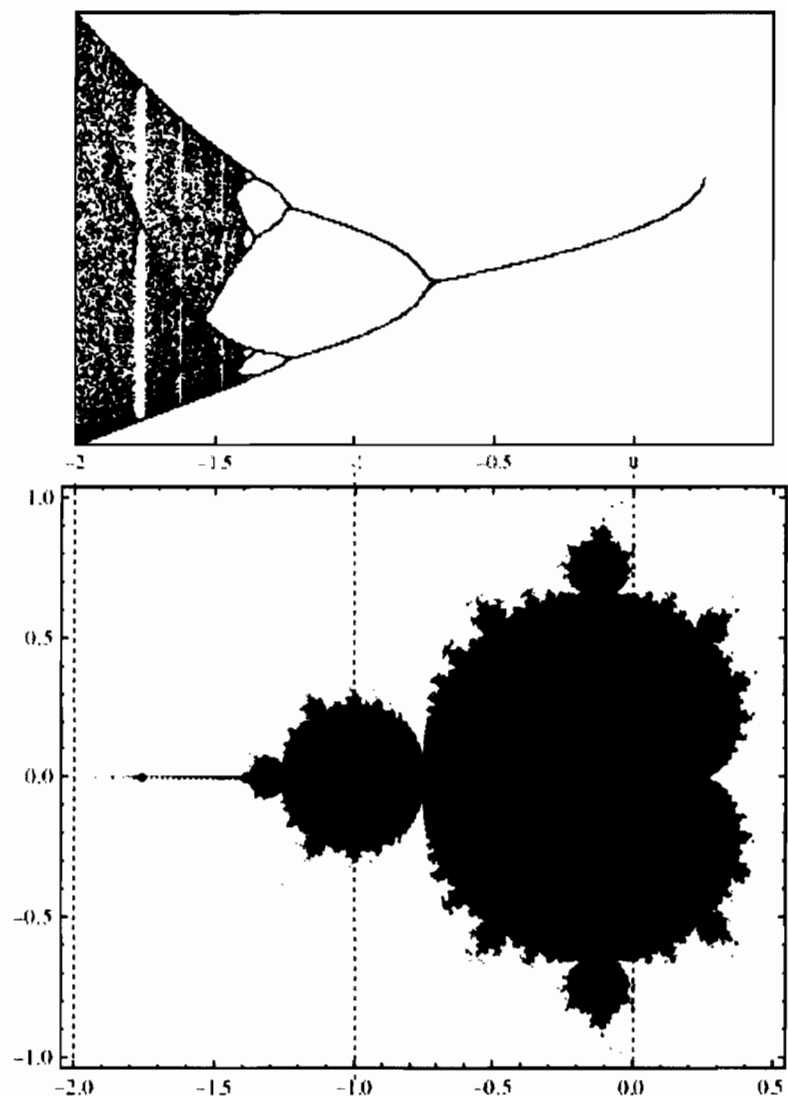
Figure 1.10.. Comparison of the quadratic iterator and the Mandelbrot set.

The Sinai Billiard

In the previous section the mixture of simple and chaotic orbits was shown to produce a fractal. A natural question that arises is how can this be accomplished physically? Figure 1.11 illustrates the transition from regular to mixed (chaotic and regular) dynamics that emerge as a result of altering device geometry. In Fig. 1.11 (a) two trajectories that have similar initial conditions traverse the empty billiard and remain close to one another. In Fig. 1.11 (b) the same two initial conditions are seen to rapidly diverge as they encounter the circular scatterer. It is the presence of the circular scatterer that introduces chaotic trajectories into the Sinai billiard and for that reason the terms Sinai scatterer or Sinai diffuser will be used interchangeably throughout this dissertation to refer to the circular scatterer. The circular scatterer introduces non-linearity, and the walls produce iteration, thus representing a physical analogue of the Mandelbrot set.

Aside from a few trivial cases, the closed billiard illustrated in Fig. 1.11 (b) will develop purely chaotic trajectories. However, introducing openings in the billiard walls allows for the possibility of a set of trajectories that are free to escape the billiard without ever striking the Sinai scatterer. This results in a mixture of stable and chaotic dynamics in the phase space of the billiard [2]. It is the mixed phase space that is predicted to produce fractal trajectories [12], specifically those fractal trajectories will lie at the boundary between the stable and chaotic orbits in the phase space of the billiard.[13]
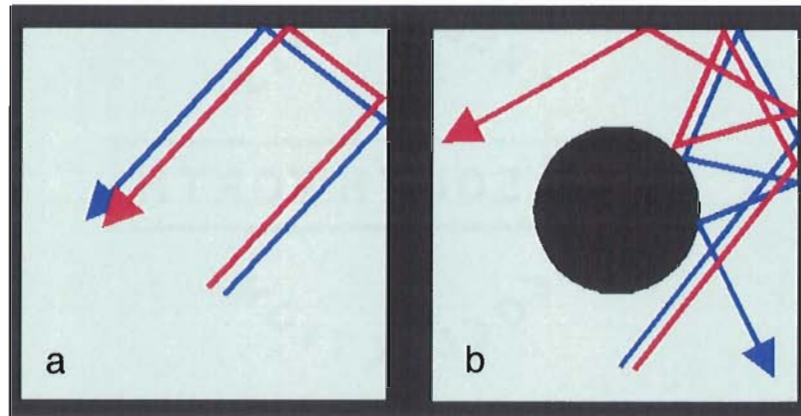
Figure 1.11. Schematic of the Sinai billiard. a) A square billiard exhibits regular dynamic trajectories in which similar initial conditions do not diverge. B) Introducing a circular scatterer (Sinai diffuser) creates trajectories that are exponentially sensitive to their initial conditions, thus introducing chaos to the system.

Figure 1.12 schematically show an 'open' Sinai billiard (a) along with its analog, an 'infinite horizon' Sinai billiard. Infinite horizon billiards are billiards in which there are channels that permit a traversing particle to travel through and never reflect off of the billiard walls. The infinite horizon billiard shown in panel (b) is sometimes referred to as a Lorentz gas. In 1905, Lorentz used a similar model, to describe the diffusive motion of electrons traveling through metals. In his model the scattering spheres were randomly distributed under the constraint that they could not touch one another [14]. Figure 1.12 schematically illustrates that two trajectories with similar initial conditions can rapidly diverge after reflecting off of the Sinai scatterer(s). The presence of the circular scatterers introduces non-linearity in the trajectories and reflection off of the walls (in a) or other scatterers (in b) iterates this process. In this

manner, both billiards (a) and (b) can be viewed as physical manifestations akin to the Mandelbrot set.
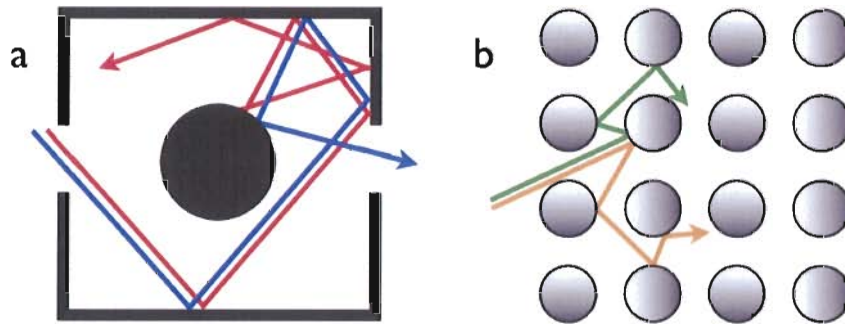
Figure 1.12. Schematic of the Open and infinite horizon Sinai billiard. a) Opening the billiard to allow escape leads to a mixed phase space. b)The equivalent infinite horizon Sinai billiard. In both cases trajectories that started with similar initial conditions rapidly diverge.

While the open Sinai billiard meets the requirements of having a mixed phase space, the details of some basic properties of this billiard, such as how does scatterer size, or the opening size, effect the dynamics are not well charted. With this in mind, and our labs dedication to physics education, we set out to develop a simple demonstration suitable for use in the classroom. There are many examples of demonstration apparatuses showing chaotic scattering that produces fractal patterns[15–17]. Replicating the apparatus of Ref. [15], a light scattering system consisting of four reflective spheres stacked in a pyramid formation was built.

In this experiment, the top three openings created by the stacked configuration are illuminated with colored light. The fourth (bottom) opening is used to capture

an image of the pattern created by the iterated reflections. A photograph of this apparatus is shown in on the left hand side of Fig. 1.13. In this apparatus light is used to play the role of a particle that travels in straight lines and reflects specularly. A 'Sinai cube' was built to investigate the influence of walls on this sort of system. Using front surface mirrors to avoid secondary reflection, the cube is constructed with openings at the upper corners, this apparatus is shown in the right hand side photograph of Fig. 1.13 without the top mirror in place. A reflective sphere is suspended from the top mirror creating the Sinai cube. Three of the top corners are illuminated with colored light, in the fourth corner, a camera is used to capture the image created by the light's repeated reflection off of the central Sinai diffuser. Three different Sinai diffuser sizes were used, the diameter of the largest sphere is approximately the same as the side length of the cube. This is the sphere that can be seen in the photograph on the right hand side of Fig. 1.13. The smallest sphere's diameter is roughly 1/3 of the side length and can be seen in Fig. 1.14 (d).

Figure 1.13. Photograph of the stacked sphere configuration (left) and the Sinai cube apparatus (right).

This image of the Sinai cube is presented again in Fig. 1.14 (a) to emphasize the effect of placing the top mirrored surface onto the cube. In Fig. 1.14 (b) the top of the cube has been set in place and a photograph was taken in an otherwise darkened room. This shows the unaltered image from the fourth (unlit) opening.

Figure 1.14 (c) illustrates the diverging trajectories that result from reflection off of the Sinai scatterer. These images are a top down view of the cube (the top has been removed). The Sinai scatterer has been supported from below. Laser light has been sent in parallel to the bottom plane of the cube through a small hole. The incoming beam is seen to reflect off the sphere in (c) resulting in rapidly diverging trajectories of the two initially close paths. In (d), the sphere has been removed and trajectories that initially began close together remain close to one another until they finally are able to escape the cube. It should be noted that in the photographs, shown in (c) and (d), the color of the laser beam has been altered to illustrate the distinction of the separate paths.

Ray tracing techniques were performed by Ben Van Dusen, using a 3D modeling program called Cinema4D to model both the stacked sphere and Sinai cube images. Figure 1.15 (a) shows the image of the reflections on the Sinai diffuser obtained from the unlit opening of the Sinai cube in which the diffuser diameter is roughly 1/3 the wall width. Consider one of the blue colored regions of either Fig. 1.15(a) or (d). If the viewer were to shine a laser pointer at one of these blue regions from the viewing opening, the light would enter the opening and reflect off the central scatterer in (a),
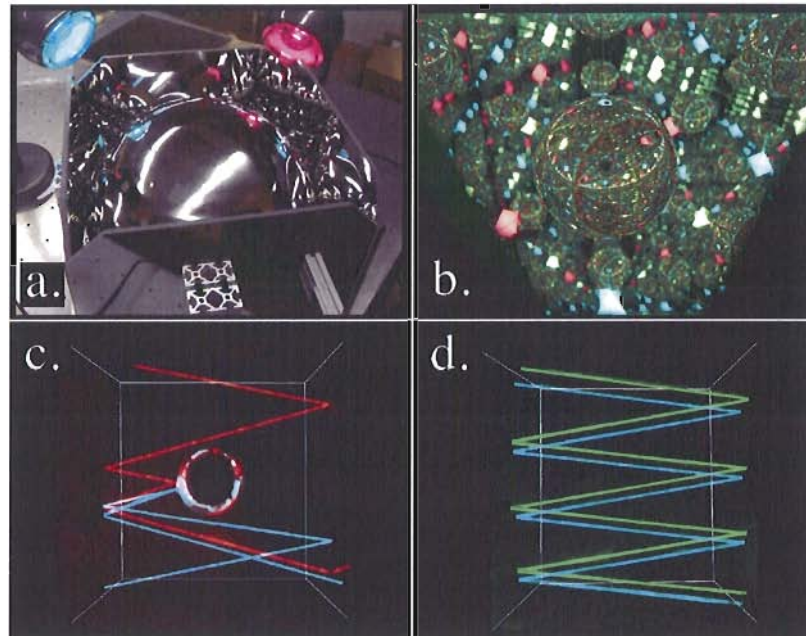
Figure 1.14. The Sinai cube (a) before the top mirror is set in place. (b) The image obtained from the unlit opening of the Sinai cube. Reflections of laser light sent into the Sinai billiard with (c) and without (d) the Sinai scatterer in place.

or one or more of the stacked spheres in (d). After a potentially large number of reflections, the light would finally exit the apparatus through the opening associated with the blue light. Thus each of the colored regions is an indication of the initial opening through which the light entered. Of course, the black regions represent the unlit opening, and are black simply because the photograph was taken in a darkened room. This is the essence of the ray tracing procedure, each ray of light that enters the camera aperture is traced back to the opening that ray emerged from. The ray tracing model of the Sinai cube is shown in Fig. 1.15(b). Experimental (d) and modeled (c) images of the stacked sphere configuration are shown in the bottom panels.

The boundary of each colored colored region of the image obtained by the stacked
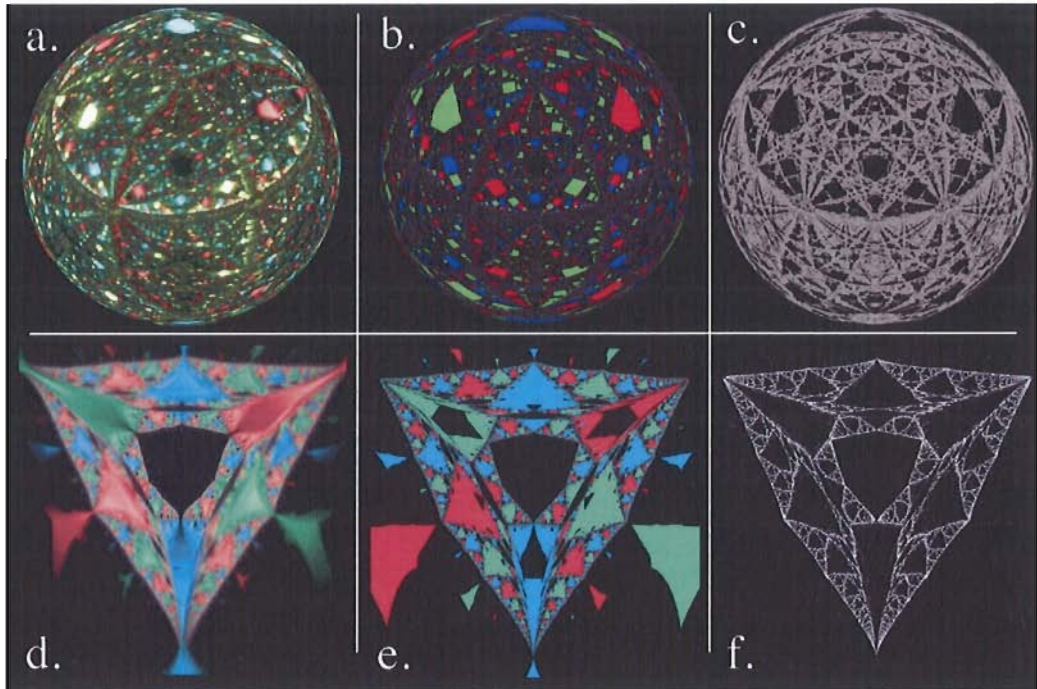
Figure 1.15. Photograph of the reflections off of the (a)Sinai scatterer and (d) Stacked Spheres. Ray tracing Model of the (b)Sinai scatterer and (e) Stacked Spheres. Edge detection analysis of the (d)Sinai scatterer and (f) Stacked Spheres

spheres is proposed to be a 'Wada' boundary. A Wada boundary is a particular kind of fractal that can arise when there are three or more means of escape. The means of escape are termed 'basins'. Any point on the boundary of a Wada basin is also on the boundary of all the other basins [13, 15]. Thus, it is the boundary of these colored regions that were shown to be fractal [15]. For that reason, an edge detection procedure is used to trace out these boundaries. Results of the procedure for the ray tracing diagrams are shown in panels (c) and (f) of Fig. 1.15. Edge detection was performed on both the experimental and the modeled images of each apparatus in order to verify the application of the ray tracing procedures.

A box counting analysis was performed on both sets of edge detected images. The box count of the stacked spheres was in agreement with the reported value of $D_F = 1.6$. Consistent results were also obtained between the experimental and modeled images of the Sinai cube. Scaling plots have been combined in Fig 1.16. The 33% filled Sinai cube simulation and experiment (upper solid and dashed lines respectively), while the lower solid line depictis the value ($D_F=1.6$) of the stacked sphere configuration (lowest solid line).
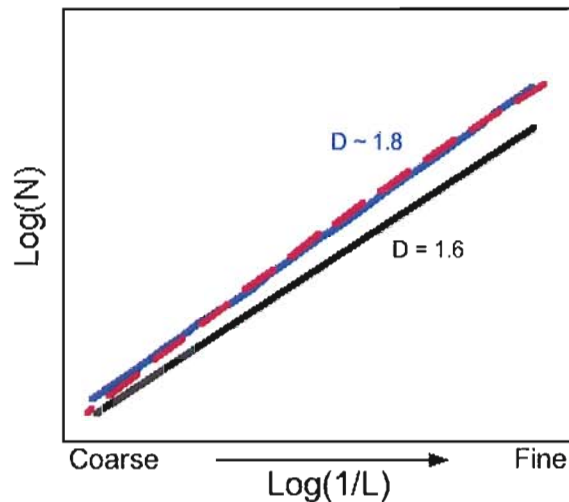
Figure 1.16. Scaling plots of the Sinai cube and stacked sphere images. The lower solid line depicts represents the scaling plot of the stacked sphere configuration.

Having confirmed that the ray tracing procedure delivers results consistent with experiment, the next step was to examine the effect of the size of the scatterer on the resulting trajectories inside the Sinai Cube. The ray tracing procedure allows for better resolution than the experiment and more freedom in altering the scatterer size. In the physical experiment we are limited to 3 commercially available scatterer sizes,

whereas the ray tracing procedure allows a simple means of altering both the scatterer size and location. In Fig. 1.17, D_F is plotted against scatterer position (blue squares, top axis) as the location of the scatterer is shifted from the center of the cube until it is touching one of the cube walls. This plot indicates that the D_F value is independent of the location of the sphere. This allows a bit of freedom when suspending different sized scatterers from the center of the top wall of the cube. Each of the three mirrored spheres was then suspended from the center of the cube and photographs were taken and analyzed as previously discussed. The results are plotted in Fig. 1.17 (bottom axis) with red squares. The ray tracing model was applied again in order to fill in the gaps in the data set that arose due to the small range of commercially available sphere sizes. These data are plotted in the green triangles. The result was that the value of D_F seems also to be independent of the size of the scatterer, within the error associated with the procedure. Having determined that the value of D_F was not influenced by either the location nor the size of the scatterer, the next step was to investigate the role of the opening size.

This was accomplished by using the ray tracing model with slightly different geometry. Rather than having triangular openings in the top corners of our device, square openings in the middle of the faces of the four vertical walls of the cube are used. This allows us the further advantage being able to adjust opening sizes independently of one another. Figure 1.18 plots the results of D_F as the viewing opening (labeled front open) as well as the entrance size (labeled side open) is varied.
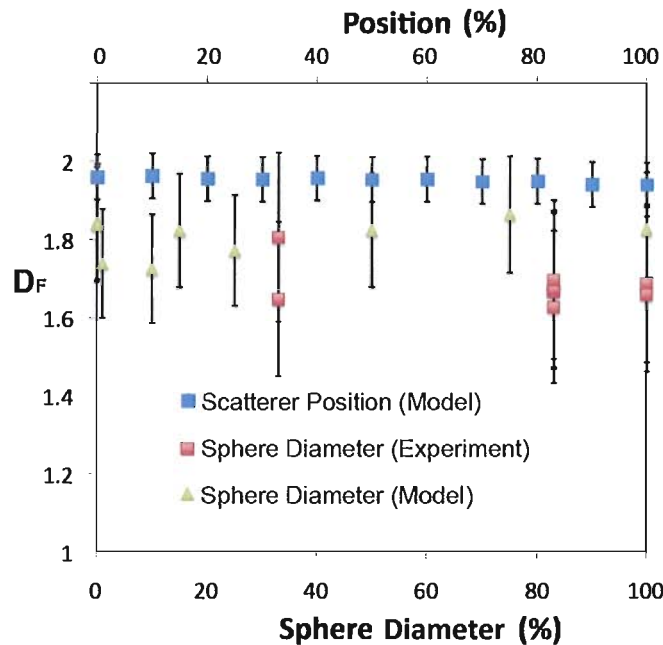
Figure 1.17. Altering Sphere location and diameter in the Sinai cube seems to have no effect on the value of D_F. Position (blue squares) was changed in the simulation by gradually moving the scatterer from the center to touching one of the cube walls. Scatterer size was altered both experimentally (red squares) and in simulation (green triangles)

Percent open is a measure of the percentage of trajectories that escape the cube without ever reflecting off a wall. One interpretation is that as the opening becomes a larger percentage of the wall size, the area in which the light can reflect off of the surface of the wall diminishes. It is interesting to note that the surface obtains the maximal value of $D_F = 1.71$ when both of the openings have an area of about 20% of the wall size.

A modified version of the Sinai cube has been built and was on display at the Portland Museum of Art, and was the subject of a presentation at Bridges Banff 2009. Figure 1.19 shows the new and improved Sinai Cube in which the bottom four

Dimension vs % open of side
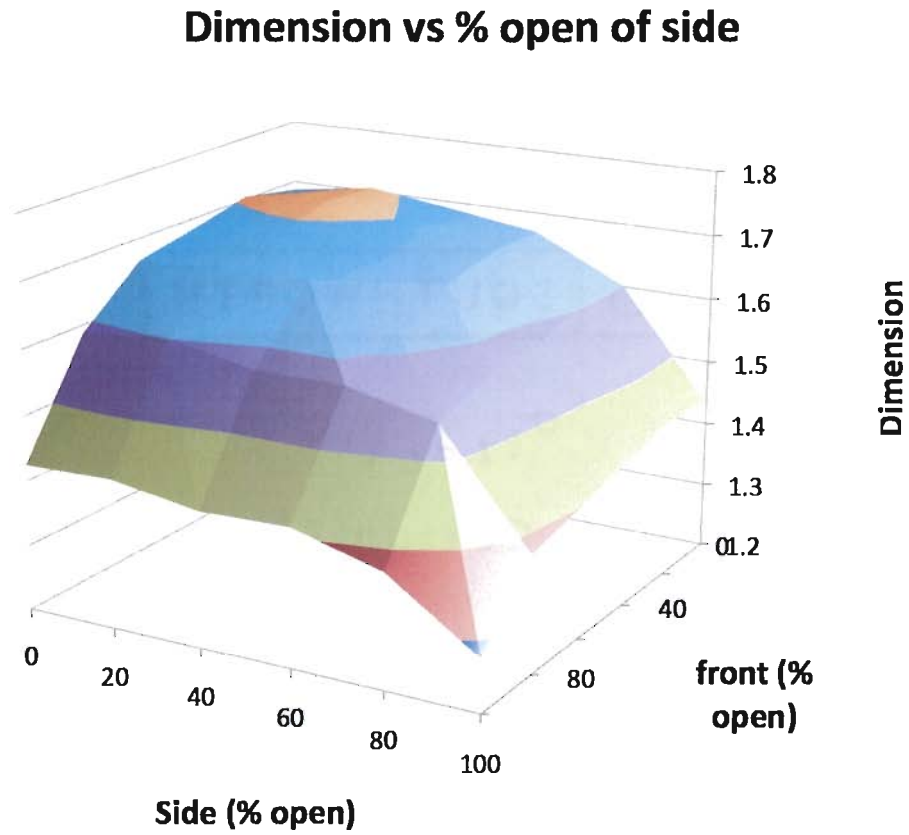
Figure 1.18. D_F plotted against relative opening size in the front and side walls of the Sinai Cube

corners of the cube are fitted with LEDs with individual on-off control. Viewing is achieved through two portals placed at the top corners of the front of the cube, and an image of this view is also presented due to its aesthetic appeal.
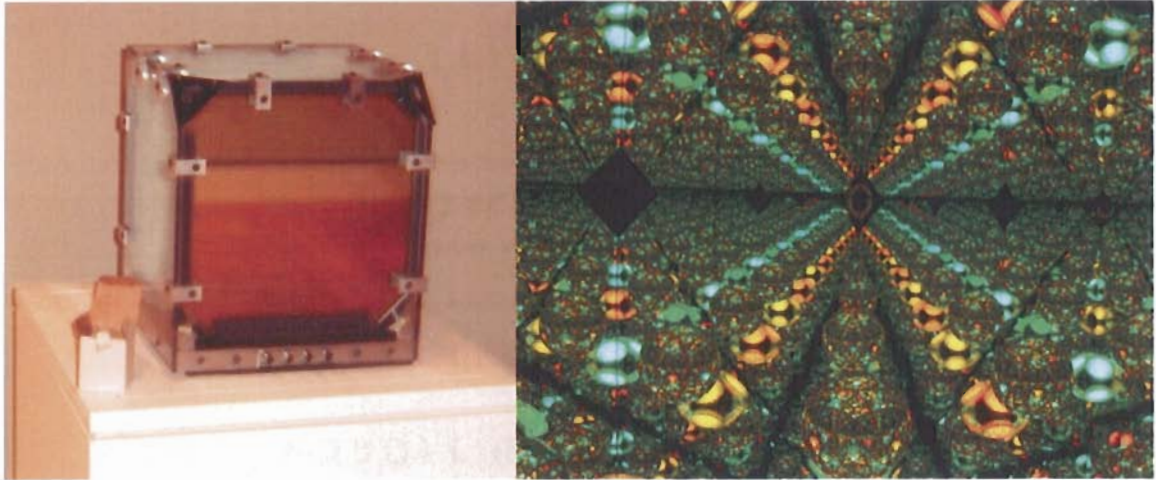
Figure 1.19. Left: The Sinai Cube (version2) on display at the Portland Museum of Art. Right: The inside of the cube as seen from one of the two viewing portals.

Conclusions

This chapter has shown that the open Sinai billiard supports chaotic, fractal dynamics. Experiments on two physical realizations of the Sinai cube were presented. In these analogous experiments, light was used to play the role of the Sinai's theoretical particle which conserves energy and exhibits spectral reflection. It was shown that the fractal dimension, D_F can be tuned by adjusting the availability of escape. This was done by adjusting the size of the openings to the billiard.

CHAPTER II

BILLIARD FABRICATION AND MEASUREMENTS

Introduction

The previous chapter was devoted to a classical description of fractal dynamics that arise due a system that contains both stable and chaotic dynamics. In later chapters that discussion will be extended to investigate the influence of chaos on the conductance properties of mesoscopic devices. To investigate this role it makes sense to start with the cleanest systems possible. This will help avoid inadvertently ascribing properties that may be sample specific, such as impurities or material defects, to the dynamical system as a whole. To accomplish this the electron billiard will be used. Following a brief overview of some of the background physics, this chapter focuses on the fabrication and measurement techniques utilized in the experiments to follow.

Background Physics

Effective Mass

Epitaxial growth allows for the deposition of a regular lattice that approaches a perfect crystal. It is possible to treat the conduction of electrons through a

semiconductors crystalline structure as free electrons negotiating through a dielectric. In this semiclassical, picture the periodicity of the lattice is accounted for by the use of Bloch states in which the wavefunction is written as the product of a plane wave and function that holds the same periodicity as the lattice itself. This then, results an " effective mass " of the the electron, m*. Semiclassically then, conduction is limited only by lattice imperfections and vibrations, which both tend to promote electron scattering [18, 19]

Two Dimensional Electron Gas

A two dimensional electron gas (2DEG) can be realized by sandwiching a layer of low bandgap semiconductor material between two layers of wider bandgap materials. The sandwiching of the materials confines electrons in a quantum well, typically to the lowest bound state, and electrons are free to move only in the x-y plane defined by the interface.

Confining the motion to two dimensions produces a constant density of states. Consider a large two dimensional k-space area Ω_{2d} containing a large number of k-space points. This will support wave vectors given by $k_x = 2\pi n_x/L$ and $k_y = 2\pi n_y/L$, where the $n_i(i = x, y)$ are integers. These wavevectors satisfy the plane wave of the form $\psi \sim e^{i\mathbf{k}\cdot\mathbf{r}}$ subject to the boundary conditions that $\psi(x, y) = \psi(x + L, y) = \psi(x, y + L)$. Then the number of allowed values for $\vec{k}$ can be estimated as simply the volume of k-space (Ω_{2d}) divided by the volume per k-space point.[20]

$$\frac{\Omega_{2d}}{(2\pi/L)^2} = \frac{\Omega_{2d}L^2}{4\pi^2} = \frac{\Omega_{2d}A}{4\pi^2} \tag{II.1}$$

Where A is the real space area under consideration. In two dimensions the ground state will consist of N electrons occupying a region of k-space bounded by a circle of radius k_F. That is to say all wave vectors whose magnitude is less than k_F are occupied. The area of this "Fermi circle" is $\Omega_{2d} = \pi k_F^2$, giving the number of allowed values for **k** as:

$$\frac{\Omega_{2d}A}{4\pi^2} = \frac{\pi k_F^2 A}{4\pi^2} = \frac{k_F^2 A}{4\pi} \tag{II.2}$$

Each allowed k value has 2 electron levels (one for spin up, one for spin down) so the number of electrons N contained in the real space area A is

$$n_s \equiv \frac{N}{A} = \underbrace{2}_{\text{for spin}} \frac{k_F^2}{4\pi} = \frac{k_F^2}{2\pi} \tag{II.3}$$

The associated Fermi momentum is $p_F = \hbar k_F$ leading to the Fermi Energy (E_F) being directly proportional to the electron density (n_s) and given by:

$$E_F = \frac{\hbar^2 k_F^2}{2m^*} = \frac{\pi \hbar^2 n_s}{m^*} \tag{II.4}$$

This relationship is particularly useful in that measurement of n_s is fairly simple at low temperatures(described below), thus allowing for a nearly direct measurement of the Fermi energy during each experimental magnetic field sweep. The Fermi

momentum also leads to an associated wavelength given by the de Broglie relation $\lambda = h/p$ and is:

$$\lambda_F = \frac{h}{p_F} = \frac{h}{\hbar\sqrt{2\pi n_s}} = \frac{2\pi}{\sqrt{2\pi n_s}} = \sqrt{\frac{2\pi}{n_s}} \qquad (II.5)$$

Similarly the Fermi velocity is $v_F = p_F/m^*$. Knowing the Fermi velocity is useful in determining another important length scale, the average distance an electron can travel before scattering off of an impurity, lattice defect or vibration, and thus losing its initial momentum. This characteristic length is known as the mean free path ℓ_μ. This distance is given by $\ell_\mu = v_F \tau$. Here τ is the momentum relaxation time and is related to the mobility (μ). The mobility is defined to be the ratio of the electron's drift velocity to the associated electric field by the expression $\mu = \frac{e\tau}{m^*}$ [18, 20]. The phase coherence length (ℓ_ϕ) is the distance an electron can travel and maintain it's quantum state and thus phase information and is determined by the relation $\ell_\phi = v_F \tau_\phi$, where τ_ϕ is a measure of the average length of time an electron can be expected to maintain its phase. Discussion of the measurement and determination of τ_ϕ will be provided later in this chapter.

Once a plane for electrons to traverse (the 2DEG) has been created, billiards are then defined in the plane by establishing device boundaries. The billiards primarily used in this dissertation are defined by wet etching a $Ga_{0.25}In_{0.75}As/InP$ heterostructure shown schematically in the left panel of Fig. 2.1. This process removes the region of the 2DEG that defines the wall boundaries, leaving behind a billiard connected to

the bulk of the 2DEG, (often referred to as the Hall bar) by a narrow constriction ($\sim$100 nm) called the quantum point contact (QPC).
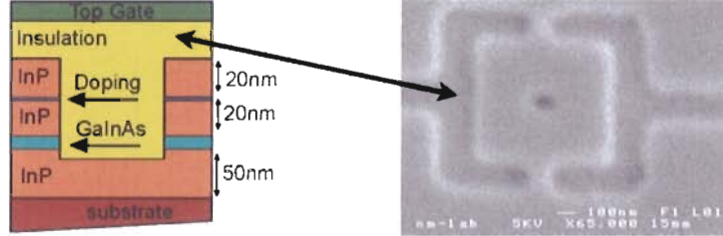
Figure 2.1. Left: Schematic of the GaInAs/InP heterostucture. Right: Scanning electron micrograph of the Sinai Billiard. The scale bar indicates 100 nm. The QPC's provide a source and drain for current through the device and are each $\sim$100 nm. The central Sinai scatterer has a diameter of 100 nm.

On the right hand panel of Figure 2.1 is a scanning electron micrograph of the electronic Sinai billiard. The scale bar in the micrograph indicates 100 nm, and the walls defining the billiard are $\sim$ 1μm in length. Dr. Theodore Martin performed an extensive analysis on the depletion of the 2DEG near the etch interface due to screening and trap states [21, 22]. The basis of this work was to model the confinement potential in the 2DEG as having a flat bottom with nearly parabolic sides. The form of this "bathtub" potential can be written as :

$$V(E_F, x) = \begin{cases} 0, & |x| \leq \dfrac{d}{2} \\[2em] \dfrac{1}{2}m^*\omega_0^2\left(|x| - \dfrac{d}{2}\right)^2, & |x| > \dfrac{d}{2} \end{cases} \tag{II.6}$$

Here both ω_0 and d will depend on E_F, and both are used as fitting parameters to numerically solve Schrödinger equation using the finite difference method. The

value of d, which will vary with E_F, is the active width of the billiard. The details of Dr. Martin's analysis can be found in his dissertation and subsequent publication [21, 22]. Using those depletion measurements reduces the active are in this billiards to $\sim 0.4\mu\text{m}^2$

Mobility measurements, as described above, reveal a mean free path of $\ell_\mu \sim 3.5\mu\text{m}$. This places the system in the so called ballistic regime, defined by the condition that $\ell_\mu > W, L$ where W and L are the width and length of the device respectively. Traditionally there are two other regimes of transport considered in mesoscopic systems. The diffusive regime $(\ell_\mu < (W, L))$ and the quasi-ballistic regime $(W < \ell_\mu < L)$ have also been used to investigate electron transport, and a schematic of all three regimes is shown in Fig 2.2

At this point it is worthwhile to define some nomenclature that will be used throughout this dissertation. The term 'device' refers to the object upon which electrical measurements are to be made. This term (device) will be used somewhat synonymously with the term 'billiard'. Typically, in the GaInAs/InP heterostuctures schematically shown in Fig. 2.1 there are three devices (or billiards) etched into the Hall bar. The term 'Hall bar refers to the 'bulk' of the 2DEG. This is the portion of the 2DEG that current is passed through, and is considerably larger than the device (i.e. billiard) dimensions. The term sample refers to the entire mesa of the heterostructure, as well as the electronic 'chip' it is attached to that enables connections to macroscopic leads.
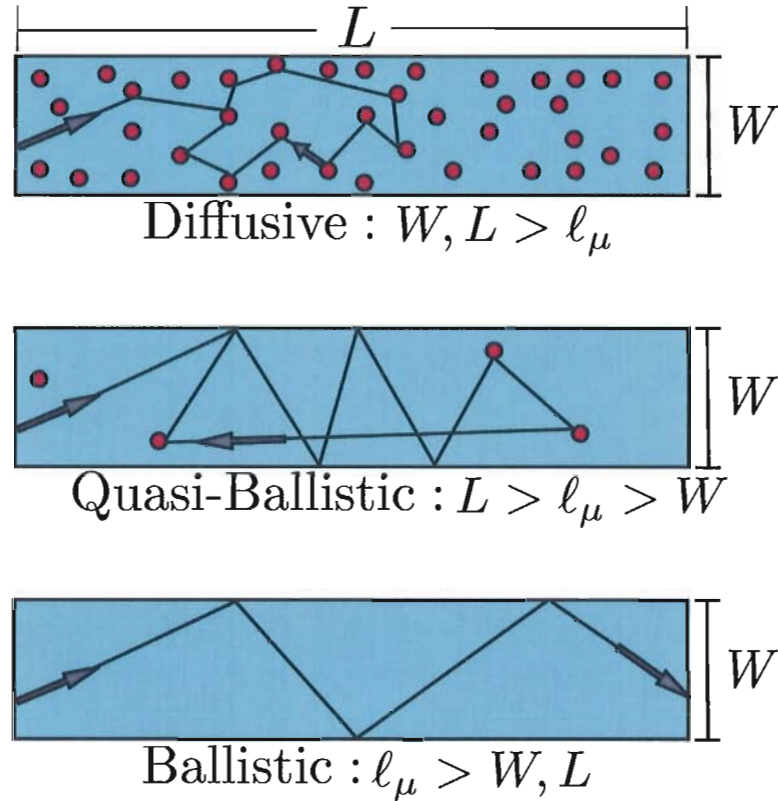
Figure 2.2. Schematic representation of (top) the diffusive (middle)quasi-ballistic and (bottom) ballistic regimes of transport.

The electron's Fermi wavelength is $\lambda_F \sim 30$nm which is smaller than W and L for the Sinai billiard. Under this condition, it takes over 20 λ_Fs to span the width of the billiard. Thus electron transport can be treated as wave packets traveling along classical trajectories as illustrated in Fig2.3. For this reason this is referred to as the semi-classical transport regime.

The fact that $\ell_\mu > (W, L)$ further dictates that it is unlikely that there will be an impurity within the plane of our billiard. This should ensure a very clean system (as compared to the diffusive regime) with which to investigate the influence of chaos
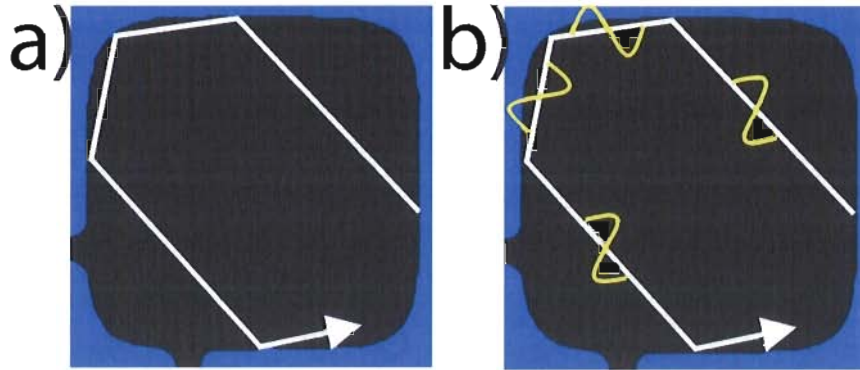
Figure 2.3. a) one possible classical trajectory through a billiard. b) illustration of the semi-classical picture, in which the Fermi wavelength λ_F is much smaller that device dimensions, allowing one to view the traversal of an electron wave packet following the classical trajectory.

in electronic transport. To probe the quantum interference effects, the conductance through the billiard is monitored while a magnetic field perpendicular to the 2DEG is swept. Sweeping the magnetic field will alter the phase of the electrons. This wil alter the conductance through the billiard via quantum interference of the electron wavefunctions traveling through the device. An example of these magnetoconductance fuctuations (MCF) is shown in Fig. 2.4. In this plot the conductance (G) through the Sinai billiard (Fig.2.1 b) is plotted against the the magnetic field (B) swept at a rate of 0.5mT every 3 seconds.

The first thing that one often notices is that the MCF are symmetric with respect to the sign of the the external field. This is clear evidence that the fluctuations are not noise. The MCF are both repeatable and robust as illustrated in Fig. 2.5. The MCF shown in that figure were taken, again with 0.5 mT resolution, nearly a month apart. The blue trace ($B01$) was the first magnetic field sweep taken during an
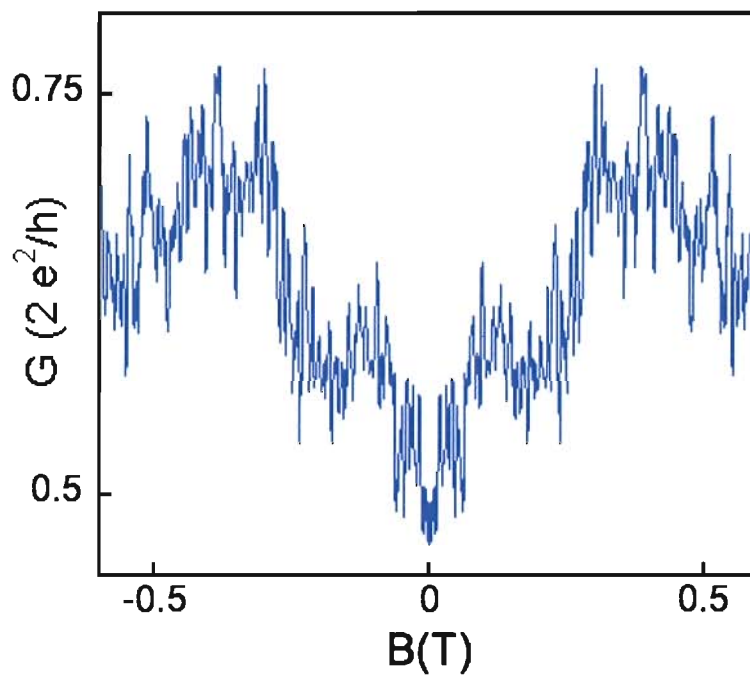
Figure 2.4. Conductance fluctuations in the Sinai billiard as the Magnetic Field is swept.

experiment. Following that sweep, many more field sweeps were conducted including a run taken at 12 K. The red sweep (B39) was taken at the end of the nearly month long experiment.
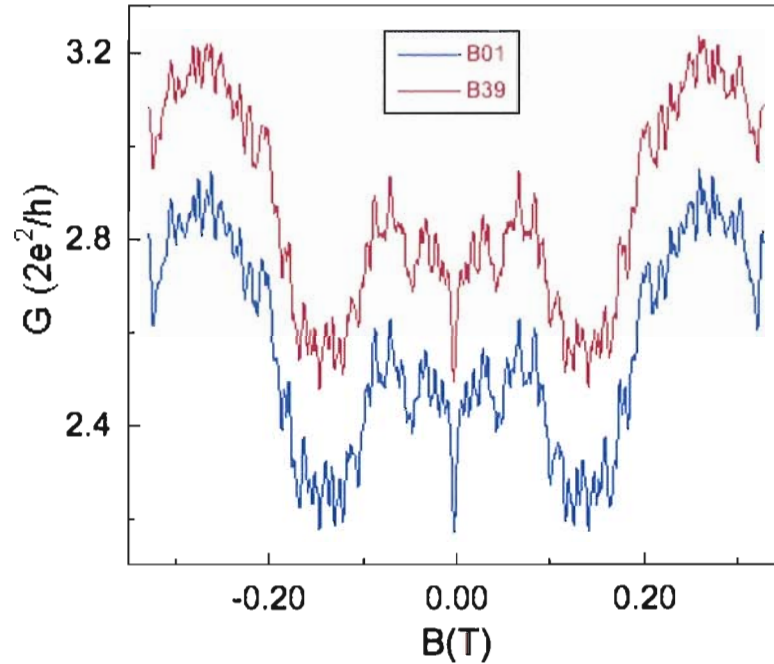
Figure 2.5. Magnetoconductance Fluctuations of a square billiard (on device H1) taken roughly 30 days apart. The blue trace labeled B01 was taken nearly a month before the red trace, labeled B39. During this experiment, the device was kept at temperatures at or below 12K.

The Aharonov-Bohm Effect

Transport in the ballistic regime is often characterized by quantum interference effects, provided the electron is able to maintain phase coherence while traveling through the billiard. The quantum interference effects can be modeled using the Aharonov-Bohm effect. Fig. 2.6 (a) shows two possible equal length trajectories through a billiard that an electron wave can split into. In the absence of an external magnetic field, these waves will maintain the same phase and will always constructively interfere.
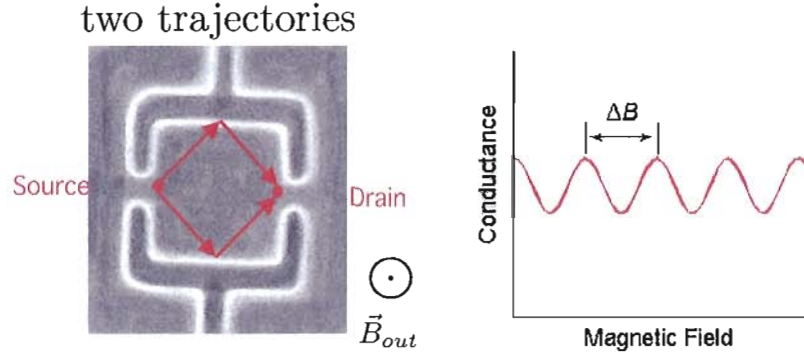
Figure 2.6. Aharonov-Bohm effect illustrated with a single pair of trajectories. (a) an illustration a single pair of trajectories through a billiard. (b) schematic of periodic conductance fluctuations resulting from varying an eternal magnetic field.

If, however, a magnetic field is applied perpendicular to the plane of travel, the associated magnetic vector potential $\vec{A}$ introduces a difference in phase depending on the path taken. The presence of $\vec{A}$ transforms the total momentum according to $\vec{p} \rightarrow \vec{p} - \dfrac{e}{c}\vec{A}$ and it is the total momentum that appears in the electrons phase term $\phi = \omega t - \vec{k} \cdot \vec{x}$. A magnetic field oriented out of the page results in a counter clockwise orientation of $\vec{A}$. This means that after entering the billiard, a wave packet traveling in the upper arm of Fig. 2.6(a) will gain phase while a wave packet on the lower arm will lose phase. This in turn will result in either constructive or destructive interference at the exit depending on the relative strength of the phase difference, which will be proportional to the magnetic flux enclosed by the two paths.

$$\Delta \phi = \frac{e}{\hbar}\Phi_M = \frac{e}{\hbar}BS \tag{II.7}$$

where S is the area enclosed by the loop. As the magnetic field B is swept this

conductance through the billiard will oscillate with a period given by $\Delta B = \dfrac{\hbar}{eS}$ as shown in Fig. 2.6(b).

In 1959 Aharonov and Bohm introduced this observable effect of the Vector Potential $\vec{A}$'s influence on the trajectory dynamics [23]. Extending this picture to include the more realistic situation of many possible loop trajectories through the billiard, results in the situation schematically shown in Fig 2.7(a).
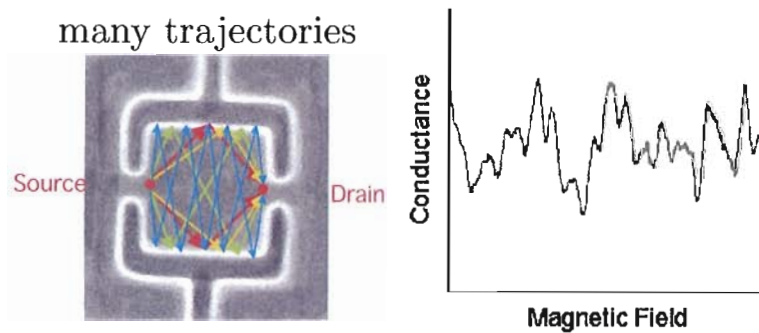
Figure 2.7. Aharonov-Bohm effect illustration with many pairs of trajectories. (a) an illustration many pairs of trajectories through a billiard. (b) aperiodic conductance fluctuations resulting from varying an eternal magnetic field.

There are many loop trajectories enclosing many different areas of flux. The interference that results is a superposition of the many different associated periods. Thus there are aperiodic fluctuations in the conductance as shown in the example of Fig. 2.7(b). The MCF arise from the distribution of many possible electronic trajectories through the billiard and, as such, are sensitive to the specific configuration of any scattering sites that mat be present in the billiard. The extreme sensitivity to the precise scattering site positioning allows the MCF to be used as a probe of the scattering dynamics of the billiard. It is worth noting here that an externally applied

magnetic field is not the sole means that such conductance fluctuations can result. The conductance through the billiard is dictated by the scattering potential defining the possible electron paths. Another means of accomplishing the potential is altering the Fermi energy at the 2DEG [24, 25]

Spectral Analysis

Viewing the conductance fluctuations as resulting from a superposition of many waves, whose periods enclose many different areas of magnetic flux, raises the natural question: What is the frequency spectrum associated with these fluctuations? More specifically, How can the frequency spectrum be related to the fractal dimension? Spectral analysis of the trace provides the answer to both of these questions. Spectral analysis delivers the power spectrum of the trace, which is a measure of the contribution of frequencies (in inverse Tesla) responsible for producing the MCF [26]. This is accomplished by Fourier transform, which decomposes the trace into a sum harmonic frequencies. Our Spectral analysis procedure follows an algorithm developed by Dr. Matthew Fairbanks for use on the MCF in our lab. In essence, it is a discrete Fourier transform since our trace is limited to a finite number of data points. Typically the range of interest is from $B \sim$-0.5 T to $B \sim 0.5$, and has a 0.5mT resolution. Noise is reduced by assigning a window size w, running a Fast Fourier Transform (FFT) over the data in the window, then moving the window across the data in steps of size $s = w/2$. At each step the FFT is repeated, and finally the average FFT of all windows stepped through the trace is taken. The output of this analysis, called the

power spectrum $S(f)$, is the (averaged) squared amplitude of each Fourier component

[8]. The trade off for the reduction in noise is the potential sacrifice of low frequency

components, for example setting w too small results in a smaller number of data

points contributing to the FFT, thus contributions that have large periods in ΔB

may not be counted. In practice, choosing a w that corresponds to $\sim 1/3$ of the data

set provides a reasonable compromise. Figure 2.8 is an example of an MCF trace and

a plot of its power spectrum.
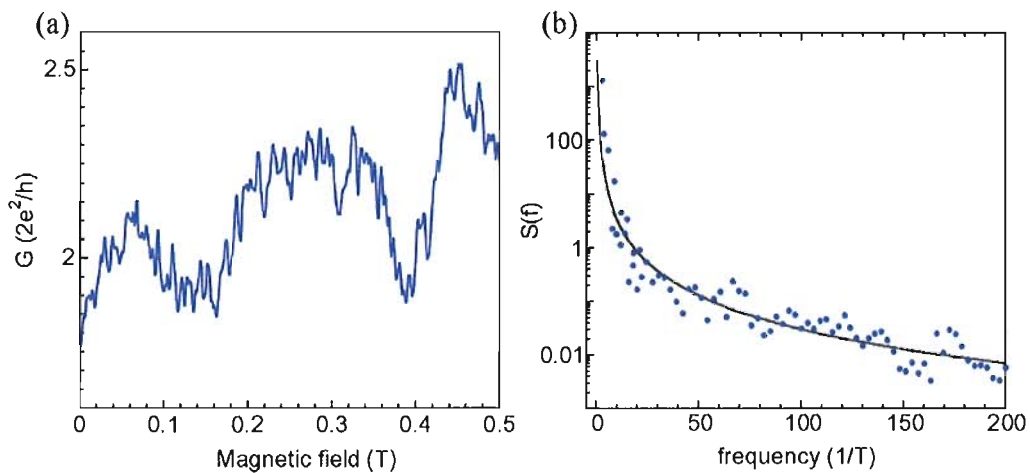
Figure 2.8. a) Magnetoconductance Fluctuations and b) the results of their spectral analysis.

The power spectrum shown in Fig. 2.8 shows a power law behavior $S(f) \propto 1/f^\alpha$

depicted by the solid line which has been added as a guide to the eye. A power

spectrum that has $1/f^\alpha$ is defined to be fractal for values of α that range between

$1 \leq \alpha \leq 3$ [26]. For historical reasons, one typically employs the use of the Hurst [1]

---

[1]Hurst was a hydrologist and contemporary of Mandelbrot, together they did some pioneering work on water reservoir design based on the feeding rivers scaling properties, It was Mandelbrot who labeled this exponent H [3, 4, 8]

exponent to relate the spectral exponent α to the Fractal Dimension D_F. The Hurst exponent is used to quantify the 'smoothness' of a curve. The spectral exponent is related to H by $\alpha = 2H + 1$. the fractal dimension is similarly related by $D_F = 2 - H$. Thus the power law behavior can be used to answer the question of how the frequency spectrum can be related to D_F by the expression

$$H = \frac{\alpha - 1}{2} = 2 - D_F \Rightarrow D_F = \frac{5 - \alpha}{2} \tag{II.8}$$

Spectral analysis is appealing in that it offers a straightforward interpretation of the MCF. For instance, since the power of a contributing frequency is proportional to α^{-1}, a large α implies a small contribution from high frequency fluctuations. However, there tends to be more scatter in the power spectrum plots than the associated scaling plots that arise from the box-counting technique. In practice, to generate a value of α for a particular trace, a box count is performed and the value of α is assigned according to Eq. II.8. The guide to the eye in Fig. 2.8 is an example of this process, also serving as an illustration of the relationship between D_F and α.

Variational Method

The fractal dimension, D_F, offers a parameter to quantify the statistics of the fractal nature of the MCF and leads to a straightforward translation to the spectral exponent α. However, a traditional box count, as described in Chapter I, is not possible for the MCF because the box sizes required would have different units in the x and y directions. To conduct a box count that does not take this into account would

result in a D_F that is dependent upon the relative aspects of G and B. To combat

this unwanted ambiguity, we employ the *Variational Method* [27] in which essentially

the G and B are normalized such that $G_{min} = B_{min} = 0$ and $G_{max} = B_{max} = 1$. This

ensures that a "square" box is obtained despite the mismatched units. This process

is illustrated in Fig. 2.9.
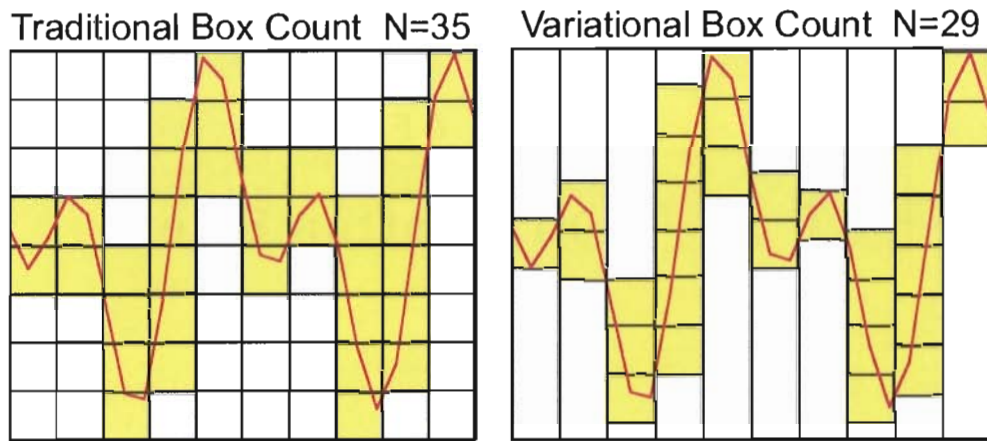
Figure 2.9. (a) Schematic representation of a single iteration of the box counting procedure illustrating that a box-count will often overestimate the box coverage of the profile. In this case it takes $N = 35$ boxes to cover the trace. (b)Variational method at the same iteration level. The same profile measured with the variation method, showing a more accurate covering requiring only $N = 29$ boxes to cover the same trace.

The added advantage of this method is that it can minimize errors associated

with"overcounting" that can result due to an arbitrary choice of the location of the

grid of boxes to be counted [27]. This error is overcome in the variational method. At

each iteration of the box counting procedure, the length of the MCF trace is divided

into equal length segments of ΔB. The number of filled boxes $N(B)$ is then the

minimum number of these boxes necessary to cover the entire trace. As with the

traditional box counting procedure described in Chapter I, the fractal dimension D_F is obtained from the slope of the scaling plot ($\log [N(\Delta B)]$vs $\log[\Delta B]$).

Low Temperature Measurement

Cryostat System

As mentioned previously, in the semiclassical regime, resistance to electron transport is limited by both lattice defects and lattice vibrations. Measurements are made at low temperatures to reduce the possibility of phonon scattering (lattice vibrations), additionally, measurements require the application of external electromagnetic fields. To achieve this we use an Oxford Instruments Low Loss Dewar (LLD). The LLD is a liquid helium cryostat equipped with a superconducting solenoid, and is shown schematically in Fig. 2.10 This system can achieve sub-Kelvin temperatures with the use of a ^{3}He Heliox-VL Insert. The insert allows base temperatures routinely as low as 240 mK and is operational to temperatures as high as 100 K. The superconducting solenoid sits at the bottom of a bath of liquid Helium (LHe) during operation and is capable of producing magnetic fields as high as 8 Tesla (10 T with the λ plate system). The magnet's power supply (IPS 120-10) allows for selection of the current polarity, and the range of accessible fields at 4.2 K (LHe temperature) are $\pm$ 8 T, with 0.1 mT resolution. The LLD is schematically represented in Fig. 2.10.

As indicated by the name Dewar, the LLD is essentially a very large, and very high quality thermos. An outer vacuum chamber (OVC) surrounds an inner chamber
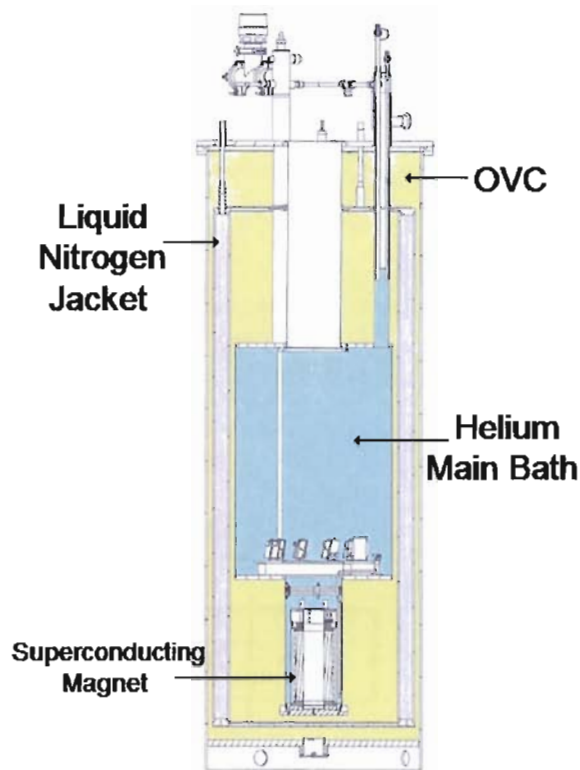
Figure 2.10. Cross section of the Oxford Instruments Low Loss Dewar. The L^4He main bath (blue) is surrounded by an outer vacuum chamber (labeled OVC, shown in yellow) and a liquid nitrogen jacket (pink) to reduce heat conduction.

that is to be kept out of thermal equilibrium with the surroundings. The OVC (shaded yellow) is evacuated to pressure of $\sim 10^-6$ mbar to minimize conduction between the outer chamber wall and the inner bath. OVC evacuation typically requires several days of pumping prior to cooling down. Radiative heat transport is an important consideration here, since radiative heat power scales with T^4, and the absolute temperature difference between the outside of the OVC and the main bath is $\sim$300 K. For this reason further shielding is provided by the liquid Nitrogen (LN$_2$)

jacket which has been shaded pink in the schematic. The solenoid is shown at the bottom of the ^{4}He bath and is superconducting at L^{4}He temperatures.

The Heliox-VL insert is shown schematically in Fig 2.11. In operational mode, the sample is mounted onto the sample stage at the bottom of the inner vacuum chamber (IVC). The IVC is then pumped down to $\sim 10^{-3}$ mbar. The IVC serves to protect the sample as the insert is immersed into the LHe, but more importantly, it isolates the sample from the (relatively) warm bath allowing base temperatures to be reached and maintained. A small amount[2] of exchange gas (^{4}He) is introduced into the IVC after pumping it down to allow conduction between the interior of the IVC and the main bath for the initial cool down. However, this gas is eventually absorbed by a small charcoal sorption pump inside the IVC that begins to absorb gas below ~ 30K. The insert is lowered into the LLD through a central port in the lid of the LLD. The combination of a set of baffle plates and a sliding seal minimize the boil off of excessive LHe during this process. By slowly lowering the IVC through use of the block and tackle mounted above the LLD, the insert can be cooled to nearly LHe temperature rather slowly without excessive LHe boil off. This is done by forcing the ^{4}He gas that has boiled off of the main bath through the insert. Once the IVC has been lowered into the magnet, the sample is located in the center of the solenoid, in operating position.

---

[2]Colloquially a sparrows fart

Cooling to Base Temperature

The insert is equipped with a sealed chamber of ^{3}He that spans from the top of the insert (labeled ^{3}He dump in Fig 2.11) through to the IVC. It terminates at the ^{3}He pot which resides just above the sample stage, which is in thermal contact via a cold finger. At room temperature, the ^{3}He is gaseous and most of it is contained in the ^{3}He dump. To ensure this is the case, a second sorption pump (^{3}He sorb), is in contact with the ^{3}He is equipped with a heater.

Reaching base temperature requires condensing the ^{3}He. This is accomplished by cooling the "1K Plate" that is mounted roughly 10 cm above the ^{3}He pot. The 1K plate is wrapped with a coil of metal tubing known as the pickup tube. One of the open ends of the pickup tube runs down the outside of the IVC canister where it is immersed in the LHe of the main bath. This tubing runs into the IVC, where it passes through a needle valve. After being wrapped several times around the 1K plate and lower portion of the ^{3}He chamber, it then travels up the remainder of the insert to a vacuum port. A rotary vacuum pomp is connected to the pump line, and is attached to the outside of the insert. Opening the needle valve reduces the vapor pressure of the L^{4}He in the pickup tube. This in turn reduces the boiling point of the L^{4}He, allowing the temperature at the 1 K plate to be reduced to ~ 1.5 K. The boiling point of ^{3}He is $\sim$3.2 K, and since the pickup tube and the copper 1K plate is thermally anchored to the ^{3}He chamber, the ^{3}He begins to condense and collect in the ^{3}He pot. Use of the heater attached to the ^{3}He sorb ensures that the sorb outgases, and all

the ^{3}He is available for condensation. The condensation process typically takes about 30 minutes. The usual practice is to ensure that the temperature at the ^{3}He pot has remained constant for several minutes, Ideally, this is close to 1.2 K but in practice it is difficult to achieve temperatures much lower than $\sim$ 1.5 K at the ^{3}He pot. In this range, the temperature is monitored by a Cernox sensor.
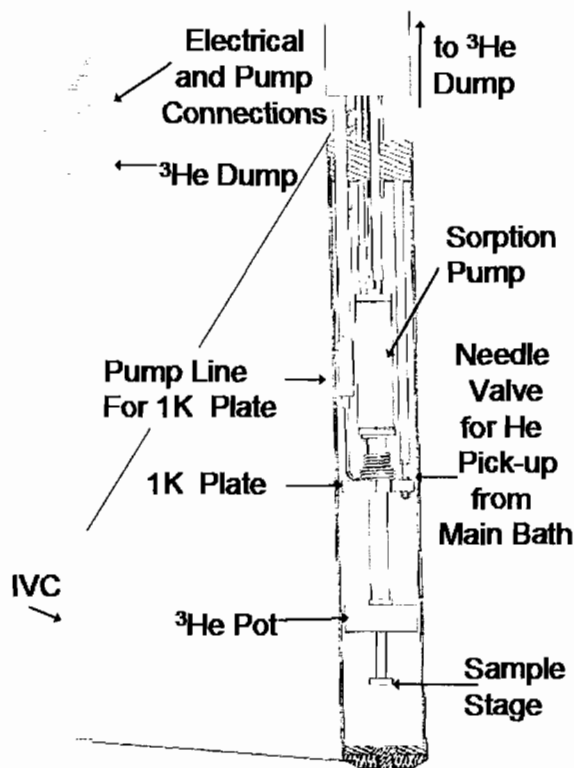
Figure 2.11. Schematic of the ^{3}He Heliox insert (left) as well as a magnified cross sectional view revealing the components of the inner vacuum chamber.

Once all the ^{3}He has been condensed, the heater is shut off and allowed to cool below 30 K. At this point, the ^{3}He sorb begins to pump, reducing the ^{3}He vapor pressure, which lowers the boiling point of the L^{3}He to our base temperature of $\sim$ 240 mK. Experience has shown that for an efficient cool down, the ONLY thing

that should changed during this process is to switch temperature monitoring from the Cernox sensor to the RuO_2 resistance sensor which is capable of measuring the sample temperature with a resolution of 1 mK from base to nearly 1.5K. This is accomplished by simply flipping a switch, any other valves or knobs should be left alone for the half-hour or so necessary to reduce the L^3He temperature to base. Much time has been wasted trying to adjust the pumping rate of the ^4He via the needle valve during and after condensation, with poor results. The sample is able to come to equilibrium with the ^3He pot because the wires that are used to make electrical measurements are wrapped around the cold finger that separates the sample stage from the ^3He pot.

<div align="center">Temperature Control</div>

Base temperature of 240 mK can routinely be achieved, and will remain stable for several days at a time. At this point, a considerable amount of the ^3He has vaporized and it is necessary to recondense, which will raise the sample temperature to $\sim 2K$. Full magnetic field sweeps typically take ~ 8 hours, so the length of time at base is adequate for quite a few magnetic field sweeps. As will be shown in Chapter IV, warming the sample even a few Kelvin has no effect on the electronic transport through the billiards measured for this dissertation.

The insert is equipped with 2 heaters that can be controlled with the ITC503 Accessory Heater Controller. When the desired temperature is below 1.4 K, the previously mentioned ^3He sorb heater is put to use. This controls the temperature

at the sorb, and thus its pumping rate, which in turn adjusts the temperature at the ^{3}He pot. Temperatures above 1K up to 100 K are controlled by a heater affixed to the ^{3}He pot which directly warms the pot. In either case, the controller's function is to come as close as possible to the desired temperature. This establishes a steady state in which the heat provided is exactly matched by the heat lost to the system surroundings. This is accomplished through standard PID control. In brief, this allows for the heater voltage to be continuously varied depending on: the proportional value of the current to desired temperatures (**Proportional** control); the calculated sum of recent residual errors (**Integral** action); and the rate of change in the recent errors (**Derivative** action). The PID values are fed into the control as a feedback loop. During the experiment described in Chapter IV, a wide range of temperatures were used. Trial and error found that PID values of 7.0, 1.0, 0.2 respectively work within a few % for temperature ranges of 500 mK to 12 K.

Electrical Measurements

All electronic measurements were performed in the constant current configuration depicted schematically in Fig 2.12 unless otherwise noted. Each Stanford Research 830 lock-in amplifier (SR830) has been color coded in Fig. 2.12 for ease of description of their associated measurements. The gold rectangles around the perimeter of each sample are called 'Ohmic contacts', or 'contact pads'. They provide good electrical contact to the 2DEG (specifically the Hall bar). Electric contact between the Ohmic

pads and the 'chip'(not shown) is made by wire bonding[3] the Ohmic contacts to the 'chip' (not shown) contact pads. When a sample is to be measured, it is attached to the sample stage at the bottom of the insert. In the orientation of Fig. 2.11 the sample would attach upside down to the sample stage. The chip is a 14 pin (male) electrical connector that plugs into the sample stage, where it remains held in place by friction.

In Fig. 2.12, the Ohmic contact pads have been numbered according to a typical sample stage mounting. The sample stages used in the experiments described here utilize 14 of the 18 available connections on the stage mount, two of these are not in use, leaving 12 connections to the mesa with two "spare" ohmic contacts on the sample stage. This labeling scheme closely matches a typical measurement in the Taylor lab and is briefly described below. Faint shadowing in the center of the left hand optical microscope image reveals the location of the devices. The billiards are of suffciently small size that they canot be optically resolved. The length of that segment of the Hall bar is roughly 300μm limiting better optical resolution. Labels with arrows pointing to the location of the device have been color coded to match their associated lock-in amplifier. Note that in this configuration, the left most device (Device 1) is not being measured.

A 37 Hz AC signal (Amplitude 0.1V) is sent out via the sine out port of the blue lock-in and sent through the 100 MΩ resistor, then the 10 kΩ resistor before

---

[3]Essentially extremely small scale welding

sourcing the Hall bar at pin 17. Pin 6 is connected to ground, providing the drain. These connections are made via short BNC coaxial cables whose shield is at common ground. The 100 MΩ resistor is much larger than the device resistances ($\sim$ few kΩ) and serves to limit the current applied to the devices. Ohm's law gives the current as $I = \dfrac{1 \times 10^{-1}V}{1 \times 10^{8}\Omega}$ =1 nA. Despite this small magnitude of current, which minimizes electron heating in the devices, signal to noise ratio is on the order of 100:1. ($eV_{drop} \leq k_B T$). The constant current configuration then allows for voltage drops across the device to be translated to changes in conductance.

The remaining three SR830s are phase locked to the AC source (blue SR830). The four terminal differential voltage is measured between the central pins of the BNC cables connected to the SR830. This configuration of the SR830 ignores shield signal, so stray signals (i.e. noise) are not picked up. The leads connecting the SR830s to the sample are all twisted pairs of BNC cables eliminating stray loop area, similarly the wiring internal to the insert consists of twisted pairs. The yellow SR830 is used to measure the voltage drop across the 1 kΩ resistor. The SR830 is phase sensitive and thus can measure both real and complex components of the signal. The phase angle is generally less than 1 ° indicating that the impedance is resistive. Current applied to the Hall bar is then given by dividing the the quadrature sum of the X and Y values of the voltage drop on the yellow SR830 by the known 10 kΩ resistance.

In addition to providing the signal, the blue SR830 in Fig.2.12 is set up to monitor the voltage drop from pin 2 to pin 3. This value, when divided by the measured current
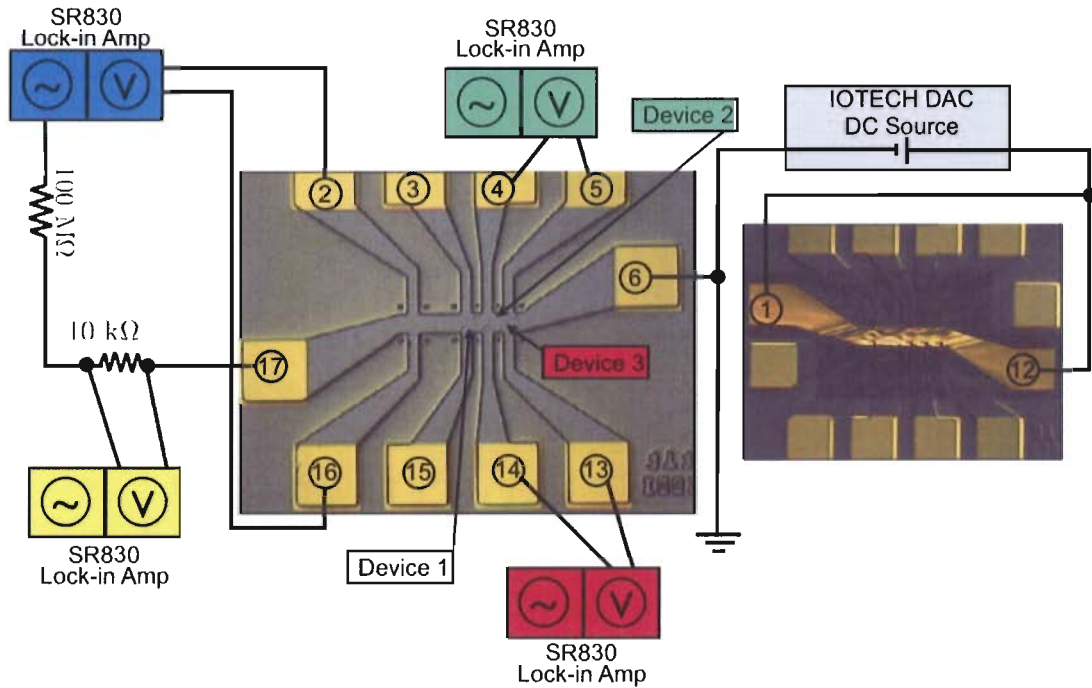
Figure 2.12. Schematic of the electronic setup in the constant current configuration. Lock in amplifiers have been color coded for ease of description in the text. The two optical microscope images show the mesa before (left) and after an insulating layer and Ti/Au top gate were deposited (right). Device labels are color coded to match the monitoring lock-in, in this configuration no measurement is made on Device 1.

gives the classical Hall resistance (R_H) [18, 19]. This constitutes the simple method of obtaining the carrier density n_s previously mentioned, since at low magnetic fields the classical Hall resistance is given by:

$$R_H = \frac{1}{n_s B} \tag{II.9}$$

On the right hand side of Fig. 2.12 is an image of the sample after the insulating PMMA layer and the Ti/Au top gate has been deposited. The IOTECH DAC is used to source a stable DC voltage to the topgate. The use of the top gate allows tuning of

n_s and thus E_F in the 2DEG. The drain for the current is provided through common ground with the signal.

The green (red) SR830 measures the voltage drop across device 2 (3) through pin 4 an 5 (14 an 13). In order to measure across all three devices on this Hall bar, sacrifice of the R_H measurement must be made. This is rarely a problem, however, since at a particular gate voltage, the value of n_s will be the same. Data collection from the SR830s and control of the magnet power supply are automated by use of LabVIEW. Incidentally, Fig. 2.12 may be used as reference for electronic measurements since the color coding was chosen to mach the labels on the physical SR830s as well as the most recently modified LabVIEW programs.

Experimental measurement of the mobility (μ) can be performed by measuring the longitudinal resistance (R_L) from pin 2 to pin 3. This measurement, coupled with n_s can be used to find μ according to $\mu = \dfrac{1}{en_s R_L} \dfrac{W}{L}$, where W is the width of the Hall bar and L is the distance over which the voltage drop determining R_L is measured.

<center>Determination of τ_ϕ</center>

The purpose of delaying this discussion until this point was to illustrate the regime of the MCF over which the "Correlation Field Analysis" is performed. For this it is necessary to display MCF over a longer range of B. The onset of this regime occurs when the magnetic field is high enough to produce a marked increase in average period of fluctuation. This can be seen quite clearly in Fig. 2.13. The MCF in that figure can be seen to take on a different character at $B \sim 0.6T$ and appear to be

"stretched out" from that point on to higher fields. This is a consequence of the trajectories entering the so called "skipping orbit" regime, defined to occur once the applied magnetic field has the effect of producing trajectories that skip around the edge of the device. This behavior is in not a consequence of being in the ballistic regime, it can also be seen in the high field MCF of a quasiballistic wire (Fig. 3.11), and diffusive Wire B (Fig. 3.10) in the next chapter, illustrating that this behavior extends across all three regimes considered.

In Fig. 2.13 the skipping orbit regimes begins at roughly $2B_{cyc}$ which has been designated by the dashed line. The term B_{cyc} is called the cyclotron field and is defined to be the B field at which a cyclotron orbit just fits inside the billiard. The cyclotron orbit is defined as a circular trajectory of an electron exposed to a magnetic field. The radius of this orbit will depend on the applied field, and their relationship can be found by application of Newton's second Law. Making use of the fact that the applied magnetic field is normal to the plane of the 2DEG, and equating the Lorentz force of the to the centripetal force gives:

$$e\, v_F\, B_{cyc} \;=\; m^* a_c = \frac{m^* v_F^2}{r_{cyc}} \tag{II.10}$$

$$B_{cyc} \;=\; \frac{m^* v_F}{e\, r_{cyc}} = \frac{\hbar k_F}{e\, r_{cyc}} = \frac{\hbar}{e\, r_{cyc}}\sqrt{2\pi n_s} \tag{II.11}$$

Of course this relationship between B_{cyc} and r_{cyc} holds for any B and r, particularly in the skipping orbit regime, this allows dropping the subscript cyc when convenient.
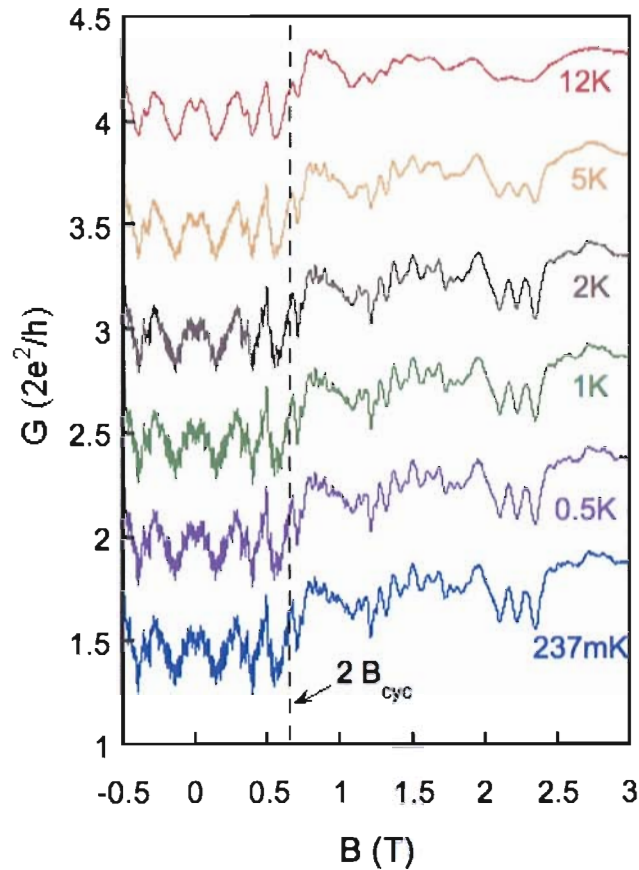
Figure 2.13. Full field traces of a billiard taken at various temperatures, the temperature ranges from (top to bottom) 12K to 237mK. The magnetic field ranges from $B = -0.5T$ to $B = 3.5T$. traces have been offset for clarity

According to the The Aharonov-Bohm effect the coherent area that is pierced with magnetic flux is that which is enclosed by the trajectories. Figure 2.14 schematically shows that area to be composed of N semicircles in the skipping orbit regime. In that figure r_{cyc} is set to be the radius of a circle circumscribed in the billiard. This means that Fig. 2.14 depicts a situation in which $B > B_{cyc}$. The area enclosed by the

N semicircles is $A_{encl} = \frac{1}{2}N\pi\, r_{cyc}^2$. Again this will hold for any r or B provided that $r \leq r_{cyc}$, allowing the freedom to drop the subscript cyc when convenient.
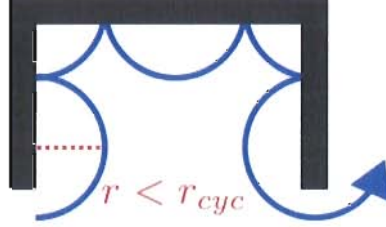
Figure 2.14. Schemeatic of the skipping orbit regime which occurs when $r > r_{cyc}$. Where r_{cyc} is defined as the radius of an inscribed circle that will just it inside a billiard

If the phase is to remain coherent in the skipping orbit regime then

$$\ell_\phi = \frac{1}{2}(2\pi r_{cyc})N \quad \Rightarrow \quad \pi r_{cyc} = \frac{\ell_\phi}{N} \tag{II.12}$$

Combining Eq. II.12 with the above expression for A_{encl} gives:

$$A_{encl} = \frac{1}{2}N\pi\, r_{cyc}^2 = \frac{1}{2}N\left(\frac{\ell_\phi}{N}\right)r_{cyc} = \frac{1}{2}\ell_\phi\, r_{cyc} \tag{II.13}$$

With the aid of $\ell_{phi} = v_F\,\tau_\phi = \frac{\hbar k_F}{m^*}$ and rearrangement of Eq.II.11 to obtain r_{cyc} this can also be expressed as

$$A_{encl} = \frac{1}{2}\ell_\phi\, r_{cyc} = \frac{1}{2}\left(\frac{\hbar k_F}{m^*}\tau_\phi\right)\left(\frac{\hbar k_F}{e\, B_{cyc}}\right) \tag{II.14}$$

Relating this enclosed area to the characteristic magnetic field scale B_c and noting that it is now convenient to drop the cyc subscripts gives:

$$B_c(B) = \frac{h}{e}\frac{1}{A_{encl}} = \frac{2\pi\hbar}{e}\left(\frac{2m^*e\,B}{\hbar^2 k_F^2 \tau_\phi}\right) = \frac{2m^*}{\hbar\, n_s\, \tau_\phi}B \tag{II.15}$$

A quantitative description of the change in the MCF character when in the skipping orbit regime is obtained by using the trace's conductance as a function of applied field $G(B)$ to define the field's correlation function as:

$$F(\Delta B) = \langle [G(B) - \langle G(B) \rangle] [G(B + \Delta B) - \langle G(B) \rangle] \rangle \qquad \text{(II.16)}$$

The half width of this correlation function evaluated at $\Delta B = 0$ defines the characteristic field scale B_c. That is:

$$F(B_C) \equiv \frac{F(0)}{2} = \frac{\langle [G(B) - \langle G(B) \rangle]^2 \rangle}{2} \qquad \text{(II.17)}$$

combining the definition of B_c (Eq. II.17) with the above expression that relates B_c to the enclosed areas of the trajectories gives:

$$B_c(B) = \frac{2m^*}{\hbar\, n_s\, \tau_\phi} B \Rightarrow \tau_\phi = \frac{2\, m^*}{\hbar\, n_s\, (B_c/B)} \qquad \text{(II.18)}$$

The expression B_c/B is then obtained by the linear portion of a B_c vs. B plot.

CHAPTER III

CONDUCTANCE FLUCTUATIONS IN SEMICONDUCTOR BILLIARDS

Introduction

The MCF data traces of the Wires $A-E$ presented in this chapter were collected by collaborating groups and provided to the Taylor lab for fractal analysis in preparation of Ref. [28]. The analysis of the wire data presented here represents this authors contribution to that work. Data for both Wire A and Wire E were measured by Dr. Koji Ishibashi's group at Osaka University. Dr. Ishibashi is now the chief scientist at the Advanced Degree Laboratory of the RIKEN research institute in Japan. The data pertaining to Wire B was provided by Dr. Carl Brown's group at Nottingham Trent University in Nottingham U.K. The data sets from Wire C were provided by Dr. Jon Birds group from the University at Buffalo in New York. This data was taken while Dr. Bird was a member at RIKEN working under DR. Ishibashi. The data from Wire D was taken by Dr. Richard Taylor during his work at the University of Nottingham, in Nottingham U.K.

The previous chapter focused on the fabrication of semiconductor devices and the measurement techniques used during experiments. This chapter will couple these the ideas with more material presented in Chapter I to investigate the conductance

fluctuations that arise as a result of exposing the semiconductor devices to an applied external magnetic field. This chapter begins by investigating the classically chaotic system of the Sinai billiard in a regime governed by quantum mechanics, this is the essence of Quantum Chaos.

Charting α

Having found a reliable way to quantify the spectral exponent α that characterizes the quantum interference effects in the billiard, the next question to address is how to best chart α. Of particular interest will be a means to chart α as parameters that could influence the quantum interference are altered. Since the MCF have semiclassical origins, one would expect that making the system more classical would have a profound effect on α. An easy way to make the device more classical is to raise the temperature. In order to observe wave interference, the waves must maintain a constant phase relationship with respect to one another. Raising the temperature increases the likelihood of electron-phonon interactions. The electron-phonon and electron-electron interactions result in scattering that destroy the electrons ability to maintain phase information and are referred to as "phase-breaking" events. Figure 3.1 displays this effect. MCF were taken in the same billiard at different temperatures. The bottom (blue) trace, taken at base temperature (239 mK) has a spectral exponent $\alpha = 1.98$. As the temperature is increased visual inspection indicates that the high frequency contribution falls off. This is supported with a measurement of α, as values

of α increase to $\alpha =2.00$ in the second coolest temperature (green trace $T= 500$mK) to $\alpha = 2.00$. The purple trace ($T = 2$ K) has an α value of 2.22, followed by the orange trace (T = 8K) with $\alpha = 2.42$, and finally when the system is warmed to 12K (red trace) the α value rises to 2.62. This indicates making the system more classical results in an increase in the spectral exponent.
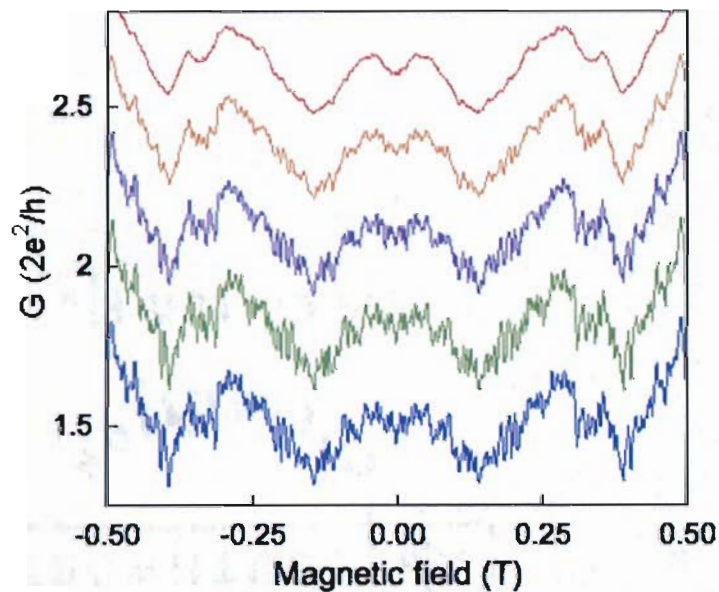
Figure 3.1. MCF at various temperatures. The evolution of the MCF structure in the same billiard as temperature is raised from (bottom to top) 239mK (blue) 500 mK (green), 2K (purple), 8K (orange) and 12K (red). α values are 1.98 (blue), 2.00 (green), 2.22 (purple), 2.42 (orange) and 2.62 (red).

In a similar manner, Fig. 3.2 shows what happens to the MCF as the device is made more quantum. In this plot, the only difference between the two billiards producing the MCF is their size. MCF were taken at base temperature, both billiards have the same geometry, and the devices are on the same Hall bar allowing for simultaneous

measurement. The area of the billiard corresponding to the red trace is ~ 6 times smaller than that of the blue trace, thus is the more quantum (λ_F closer to device dimensions). Corresponding α values are (top) blue trace $\alpha = 2.42$, and (bottom) red trace $\alpha = 2.84$.
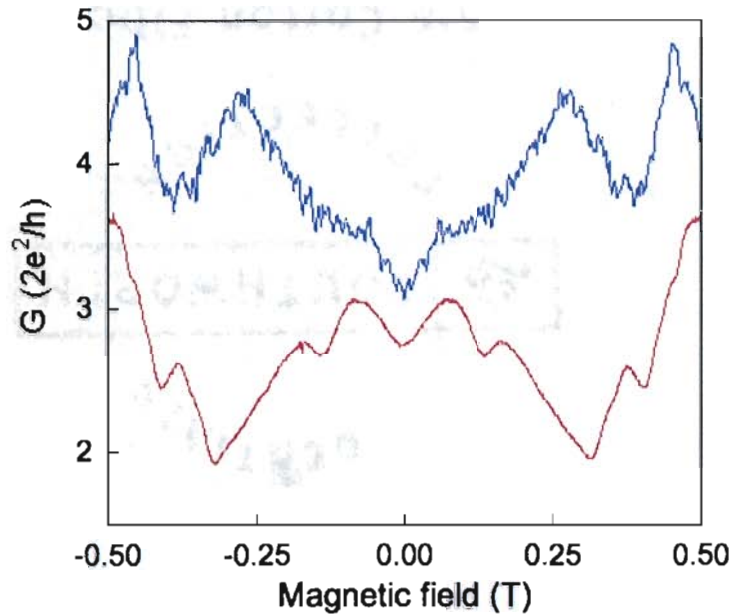
Figure 3.2. MCF of billiards with different areas. Two billiards on the same Hall bar, with the same geometry, at the same temperature. The blue (top) trace has a larger area than the bottom (red) trace. The associated alpha values are $\alpha = 2.42$ for the larger device(blue) and $\alpha = 2.84$ for the smaller device (red).

Comparison of Fig. 3.1 and Fig. 3.2 reveals an interesting effect. In each case, moving from the bottom trace to the top trace is an observation of making the device more and more classical. Yet this has the opposite effect on the spectral exponent in each case. This is an apparent dilema. Reducing the billiard area (making it more quantum) results in an increase in α as does increasing the temperature (making

it more classical). Of course these results are perfectly reasonable when looked at independently, and there is the possibility that varying these parameters (A and T) just have different effects on α. This seems to indicate that α should be charted with a parameter that encompasses both of these effects. To accomplish this, the empirical parameter Q is introduced. Q is defined as the ratio of the average energy level spacing to the average energy level broadening in the billiard.

$$Q = \frac{\Delta E_S}{\Delta E_B} = \frac{2\pi\hbar^2/m^*A}{\sqrt{(\hbar/\tau_\phi)^2 + (k_BT)^2}} \tag{III.1}$$

Here the average energy spacing is given by the term $\Delta E_S = 2\pi\hbar^2/m^*A$ which will chart alterations of two variables, the effective mass (m^*) and the conducting area of the billiard (A) [28, 29]. The form of this term can be understood in the context of dividing the energy of the highest occupied level (the Fermi Level) and dividing that by the number of occupied levels [29]. [1]Assuming that all levels up to (and including) the Fermi level are degenerately filled gives:

$$\Delta E_S = \frac{E_F}{\#\text{ of } e \text{ per state}} = \frac{\hbar^2 k_F^2/2m^*}{\frac{1}{2}N_e} = \frac{\hbar^2 2\pi n_s}{\frac{1}{2}n_sA} = \frac{2\pi\hbar^2}{m^*A} \tag{III.2}$$

A is determined by the active billiard area (accounting for depletion), and m^* is a known parameter that will depend on the heterostructure material.

The average energy broadening, ΔE_B, is given by the quadrature sum of the thermal broadening and the intrinsic smearing of energy levels that occur as a result

---

[1]ΔE_S is a common parameter in MCF studies and is often referred to as simply Δ, see for instance [30]

of scattering events that destroy phase and thereby limit the lifetime of the quantum state.[28, 29] Thus $\Delta E_B = \sqrt{(\hbar/\tau_\phi)^2 + (k_B T)^2}$ can chart alterations in the phase breaking time τ_ϕ or the temperature T. T is known and controlled during a given measurement (as described in Ch. II). The remaining parameter, τ_ϕ, is a measure of the average length of time an electron maintains its quantum mechanical state (i.e. its phase information). For this reason it is often also referred to as the "phasebreaking" or "de-phasing" time. Further discussion about the origin of these events and measurement of τ_ϕ is provided at the close of Chapter II.

Figure 3.3 displays the charting of the spectral exponent α against the empirical parameter Q. The data points represent 16 different billiards, labeled $a - p$. In total there were 161 MCF traces analyzed to construct this '$Qcurve$'. The minimum value of the Q curve occurs at $Q = 1$. This is precisely where $\Delta E_S = \Delta E_B$ and can be described as the situation where energy levels can just begin to be resolved. Q reconciles the apparent dilemma that arose in attempting to push the extremes of the semi classical description of the MCF. Increasing temperature T reduces Q through the ΔE_B term, and α starts to rise up the steep left hand side of Q. Decreasing the area, increases Q via the ΔE_S term and α tends to rise up the less steep, right hand slope. Q is not a measure of the semiclassical nature, but more a measure of the discreteness of the quantum states. For instance, $Q = 0$ would imply that either $\Delta E_S = 0$ or $\Delta E_B \to \infty$. Either increasing ΔE_S, or reducing ΔE_B results in better resolution of the energy levels.

Values of $Q < 1$ can be interpreted as more classical. For instance, raising the temperature will have the effect of allowing the ΔE_B term to dominate. Similarly values of $Q > 1$ correspond to the system being more quantum in nature. Engineering a very small device (decreasing A) or a system with a long phase coherent time (extending τ_ϕ) will each allow the ΔE_S to dominate.
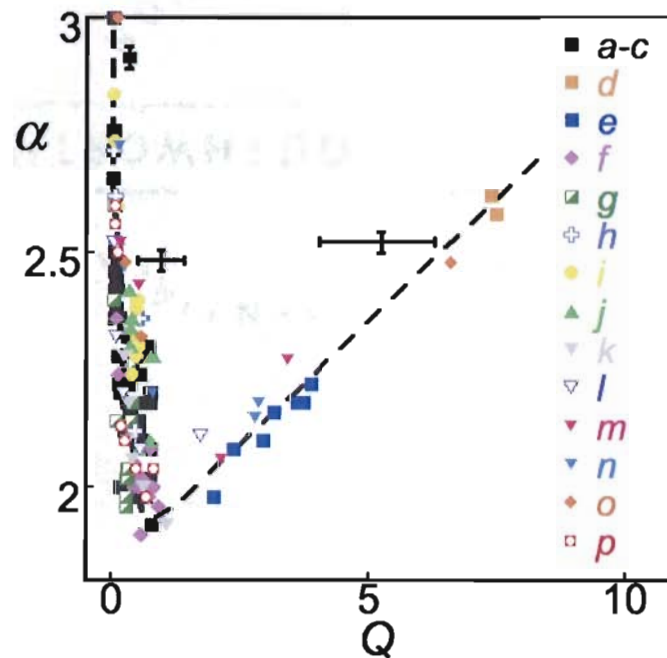
Figure 3.3. α values plotted against Q for 16 billiards representing 161 MCF. The dashed line is provided as a guide to the eye.

This would be strong evidence that the central Sinai scatterer is indeed responsible for producing the chaos that resulted in the fractal conductance fluctuations, *if* all 16 of these billiards were Sinai billiards. However, the devices used to construct the Q curve in Fig. 3.3 were of various geometries. Figure 3.4 illustrates the range of geometries used. All billiards are defined using the etched method, billiards $a - k$ are

etched into the GaInAS/InP heterostructure while billiards labeled $l - p$ have been etched into GaInAs/InAlAs, in those billiards the InAlAs takes on the same role as the InP in the GaInAs/InP heterostructure. MCF for billiards $l - p$ were measured and provided to us by our collaborator B. Hackens at the Université Catholique de Louvain, Belgium [31].
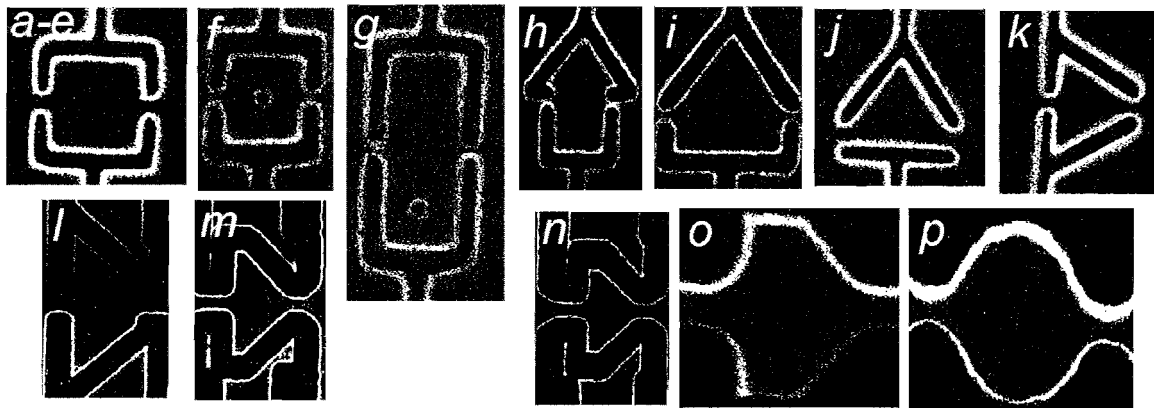
Figure 3.4. Scanning Electron Micrographs of the billiards used to construct the Q curve. Devices labeled $a - k$ are billiards the GaInAs/InP billiards and devices $l - p$ are GaInAs/InAlAs billiards

Inspection of Fig. 3.4 indicates that only 1 of the 16 billiards used to construct the Q curve in Fig. 3.3 is a Sinai scatterer. Additionally only two (including the Sinai billiard) had a circular scatterer etched out of the billiard. Yet all the 16 devices shown in Fig. 3.4 are seen to follow the same trend when the spectral exponent of the 161 MCF traces are charted against Q. This stands in contrast to predictions of other researchers, that the geometry of the wall configuration should play a major role in quantum interference effects such as fractal conductance fluctuations (FCF)[12, 32].

In Ref. [12], Ketzmeric was able to show that the MCF would be fractal *if* the

phase space was mixed, purely stable billiards would not produce fractal MCF. Stable dynamics can lead to power law behavior, but typically have $\alpha > 3$ and thus are not fractal.[2] [12, 33]. And yet only two of the devices in Fig. 3.4 (labeled f and g) had a Sinai diffuser etched away. In particular most of the geometries in that figure should promote stable dynamics. Ketzmeric also predicted that the spectral content of the MCF would depend *critically* on the exact form of the profile.[12]. Perhaps then it is not the geometry of the billiard walls that produces the chaos, but rather the steepness of the wall profiles. In fact, Ketzmeric agued that it was the 'softness' of the potential energy profile of the billiard that led to a mixed phase space [33]. This suggests comparing two sets of billiards with the same wall geometry, but different potential profiles. The MCF taken by prior members of the Taylor lab was used for this comparison [29]. Before discussing the results of that analysis, it is useful to discuss the differences between the two systems being compared. Figure 3.5 shows a schematic representation of the two billiard definition scenarios.

In the AlGaAs/GaAS system the billiard is electrostatically defined by a patterned surface gates. This is illustrated in Fig. 3.5 (a). In the surface gated method (AlGaAs/GaAs), the billiard walls are defined by applying a negative voltage to the surface gates, depleting the region of the 2DEG immediately below them. In contrast to this, in the etched method (GaInAs/InP), the 2DEG is physically removed leaving behind a trench which is later filled in with insulating PMMA. This is schematically

---

[2]$\alpha = 3$ corresponds to $D = 1$, a smooth line

shown in Fig. 3.5 (b). In each panel of Fig. 3.5, the corresponding location of the cross sections is denoted with the blue line in the top down view of these schematic "billiards".
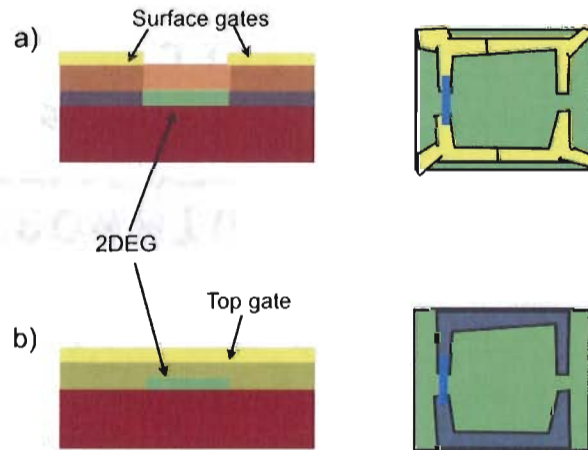
Figure 3.5. Schematic representation of billiards defined with a) surface gates and b) etching away the 2DEG. In the surface gate method the 2DEG is depleted by application of a negative voltage whereas in the etched method, portions of the 2DEG are physically removed to define the billiard wall. On the right hand side of is a top-down of the schematic billiard with a blue line illustrating the location of the cross sectional view.

The main advantage of the AlGaAs/GaAs system is that with clever engineering, the surface gates can be created in such a way as to have control over which portions of the billiard are depleted. In this way one can then ground some portions of the billiard to turn off desired features. For instance it is possible to create a Sinai billiard in the surface gated method that allows one to turn on or off the central scatterer to directly measure the effect of its presence on the MCF in the billiard.[34] This comes at the cost of device fidelity. The difference in billiard definition has a direct

influence on the potential energy profile at the billiard boundaries. Electrostatically depleting the 2DEG results in a billiard with softer walls. The role of the device walls is of particular interest. In 1996 Ketzmeric published a paper illustrating that systems with soft walls create phase space (velocity vs. position) with a mixture of regular (stable) and chaotic orbits that generically generate fractal trajectories.[12] In the surface gated system the soft walls could therefore contribute to the chaotic nature of the fractal trajectories.

The advantage of the etched system is that it produces harder walls. Producing harder walls offers reliable control of the device geometry. This system can then be used to investigate the role of the walls themselves, as well as the shape of the billiard the hard walls produce. Figure 3.6 Illustrates the difference in the potential profile of the billiard wall depending on the method used to define the walls. In Fig. 3.6 (a) the cross sections of the potential energy, E, are shown for both billiard definition methods. This cross section is taken across the center of the billiard and maps the E as a function of the distance of the center of the billiard denoted by $X = 0$. Both methods illustrate a "bathtub" profile, yet the surface gated method (AlGaAs/GaAS, dashed line) is much shallower than the etched method (GaInAS/InP, solid line).

Comparison of the gradient of the potentials reveals that the GaInAs/InP system's profile is nearly an order of magnitude steeper at an energy of $E_F = 10$meV [22, 28]. This difference is even greater at lower values of E_F. The reason for the dramatically steeper profile is understood to be a consequence of the fact that the surface gates are
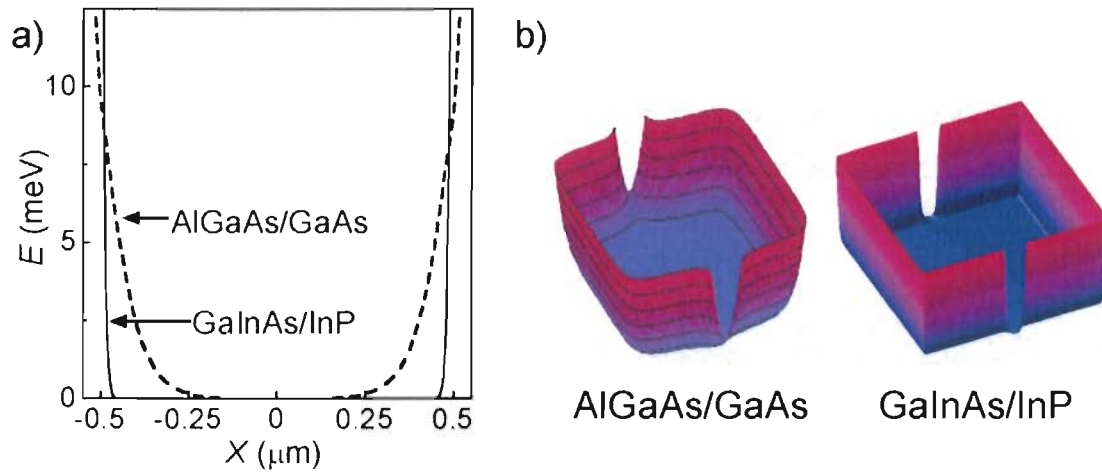
Figure 3.6. Simulation of the potential profile in the InGaAs/InP and AlGaAs/GaAs square billiards. a) cross section of the potential energy E as a function of the distance from the center of the billiard (denoted by $X = 0$). This cross section is taken across the central region of the square, the profile of the GaInAs/InP billiard is depicted with a solid line while the AlGaAs/GaAs profile corresponds to the dashed line. b) 3D model of the potential energy profiles of each system.

more remote than the surface charge of the etched boundary [28]. Figure 3.6 (b) shows a 3D simulation of the potential profiles that define a billiard by the surface gated (left) and etched (right) methods. In these simulations ionized donor and surface charge effects are included as Poisson's equation is solved throughout the billiard utilizing an iterative relaxation method to solve Poisson's equation on a discrete grid. These simulations were produced by T.M. Fromhold, further details on this method can be found in Ref. [35].

There were 5 square billiards defined in the etched (GaInAs/InP) heterostructure. This led to 67 MCF traces whose α values were determined. These were compared to 49 MCF traces taken on 9 AlGaAS/GaAs billiards. As indicated in Fig. 3.7 this Q curve was constructed using billiards defined on both heterostructures. The

blue squares represent α values obtained from the etched system. The red cirles depict α values corresponding to MCF taken in billiards defined on a GaAs/AlGaAs heterostructure. The dashed line is the same guide to the eye that was provided in Fig. 3.3. All of the 116 α values of the 14 devices analyzed on the two different heterostructures lie on the *same* Q curve. Clearly the structure of the MCF does NOT depend on the potential profile as predicted [12].
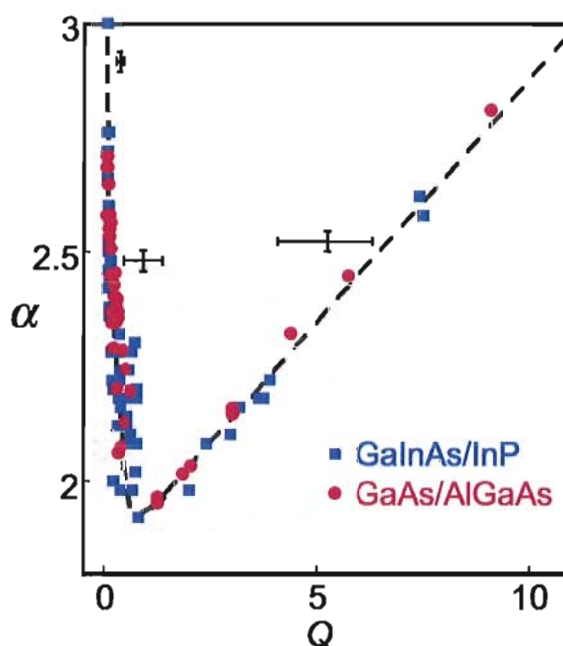
Figure 3.7. The Q curve: the specral exponent α plotted against the empirical parameter Q defined as the ratio of the average energy spacing to the average energy broadening. The dashed line is provided as a guide to the eye.

This prompts a natural question, what then is producing the chaos required for a mixed phase space? If the chaos is not induced by the wall geometry or potential profile, that only leaves something within the billiard itself to produce the chaos. One explanation is that perhaps these clean billiard systems are not quite as clean as

initially advertised. It is plausible that material induced disorder is playing a much more prominent role than was considered. Both of these systems utilize modulation doping to separate the donated electrons from their donors. This was intended to provide a clean 2DEG without significant scattering from ionized donors [19]. Perhaps modulation doping was not as successful as intended. Perhaps the ionized donors still induce some scattering in the 2DEG. Scattering significant enough to promote chaotic trajectories. Is it possible that modulation doping was successful in increasing mobility, but unsuccessful in the sense that ionized impurities, though remote, remain a dominant source of scattering? This question is addressed by deliberately looking for devices in which the material induced disorder is present within the plane of electron travel.

Charting α in Diffusive and Quasiballistic Wires

The idea that remote ionized donors create small disturbances in the otherwise smooth plane of the billiard has been well documented[36–39]. While this scattering is reduced significantly with modulation doping, it is not eliminated. The result is that these ionized impurities create small perturbations in the otherwise smooth plane of the billiard. This roughens the potential, creating a rolling landscape through which the electron waves travel. The "hills" in this landscape are small, and lead to small angle scattering. It is estimated that roughness of the landscape is an order of magnitude smaller than E_F [36]. In Ref.[28] we proposed that the role of the

billiard walls is to repeatedly reflect the electron waves through this roughened terrain. This process iterates the small angle scattering, thereby amplifying the effect. This model should also hold for quasiballistic and diffusive wires. This section presents an experimental investigation of conductance fluctuations measured on four diffusive wires and a quasi-ballistic wire

Table 3.1 lists the electron transport parameters of the wires considered in this investigation. The measurements used to obtain the listed parameters are described in detail elsewhere [40–45]. Traditionally, wires are categorized into three transport regimes: the diffusive regime (defined by the condition $\ell_\mu < (W, L)$ where W and L are the width and length of the devices conducting channel), the quasi-ballistic regime ($W < \ell_\mu < L$) and the ballistic regime ($\ell_\mu > (W, L)$) [46].

Device	Regime	$L(\mu m)$	$W(\mu m)$	$\ell_\mu\ (\mu m)$	T (K)	τ_ϕ (ps)
A	Diffusive	2	0.30	0.050	1.5 - 4.2	2 - 6
B	Diffusive	1.3	0.60	0.041	4.2 - 50	0.1 - 0.5
C	Quasi-Ballistic	30	0.55	0.97	0.04 - 4	125
D	Diffusive	10	0.26	0.030	4.2 - 37.5	0.2 - 0.3
E	Diffusive	3.5	0.96	0.36	1.4	7

Table 3.1. Details of the wires: regime, wire length (L), lithographic width (W), mean free path (ℓ_μ), temperature range (T) over which device measurements were made and phase coherence time(τ_ϕ)

Wire A is an n^+-GaAs (Ref .[42]) diffusive wire ($W, L, > \ell_\mu$), so it does not have "remote" ionized donors. Rather the dopants are situated within the conduction channel. The wire is made of a layer of Se doped GaAS sandwiched between layers of

undoped GaAS, and was grown using metal organic chemical vapor deposition. The wire was defined by electron beam lithography (EBL) and dry etching techniques.

A consequence of the 'in plane' dopants is that scattering off of the impurities will lead to large angle specular scattering as opposed to the gentle soft angle scattering described in the 2DEG billiards. This is a marked difference in the level of scattering induced by the impurities. The MCF are shown in Fig. 3.8. This data was taken and provided to us by K. Ishibashi, a collaborator at Osaka University, in Osaka, Japan [42]. The reason for the mean conductance $G(B) - G(B = 0)$ being plotted in arbitrary units is that our collaborators no longer had access to the raw data files, and were only able to supply us with an rather high resolution copy of their original plot. This required development of a program that would digitize the data. The full range of magnetic field was known, thus the $B(T)$ axis is accurate. The MCF of Fig. 3.8 are taken at temperatures (top to bottom) of 1.52 K (blue), 2.92 K (red), 4.2 K (green) and 62K (tan) as indicated in the label. The structure of the 62K (bottom, tan trace) is attributed to the geometry of the wire and is illustrative of the classical background trend.

A box count, using the variational method, was conducted on each trace and the resulting scaling plot for the 4.2 K trace is shown in Fig 3.9. The fractal dimension D_F is obtained from the slope of this line, over the relevant region. The range of the fractal region indicated by the labels B_U and B_L which represent the upper and lower cut-offs respectively. B_U ensures that the box counting statistics are accurate
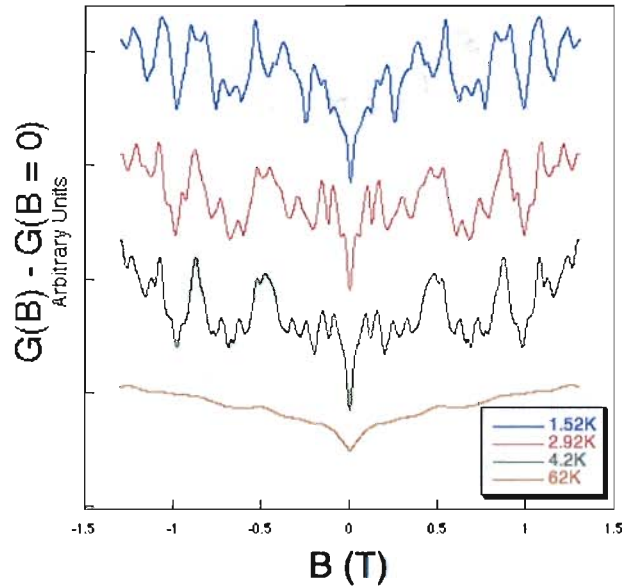
Figure 3.8. MCF of diffusive wire A taken at various temperatures. Temperatures are indicated by the label.

by establishing the largest box size used to determine D_F. Considering box sizes that are too large will result in an over estimation of D_F, as it is likely that any trace will occupy most or all large boxes. Traditionally B_U is picked such that the largest box size requires no less than 49 squares to cover the trace. B_L is determined by the period of the smallest features in the MCF. Estimation of this period is a matter of locating fine scale features in the MCF, and calculating the peak to peak difference in B. If small scale fluctuation have peaks at B_1 an B_2 then those fluctuations have period $\delta B = |B_1 - B_2|$ The log of this value sets B_L, $B_L = \log[\delta B]$

Wire B is a MBE grown n+GaAs diffusive wire defined by EBL followed by reactive-ion etching [41]. MCF of this device were taken by C. V. Brown, a collaborator at Nottingham Trent University, U. K. and provided to us for analysis. Figure 3.10
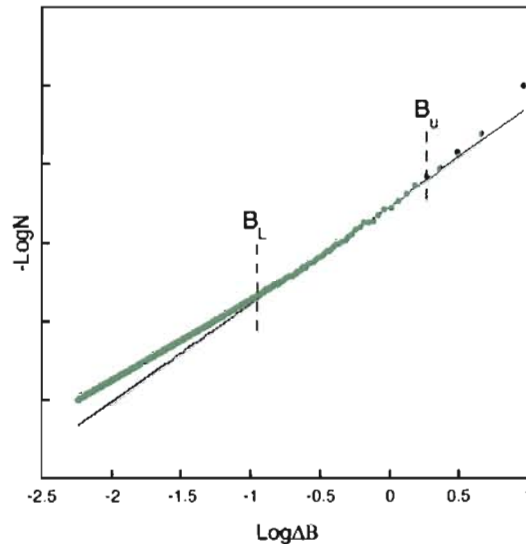
Figure 3.9. Scaling Plot of diffusive wire A. B_U and B_L indicate the upper and lower cut-offs respectively.

shows the MCF (left) and fractal analysis (right) of this wire. Traces were taken at (top to bottom) 4.2 K , 12 K and 20 K. The traces have been vertically offset for clarity. In each trace, the actual zero field conductance was $G(0) = 8.5(2e^2/h)$. Again the complexity of the fluctuations reduces as the temperature is increased.

In the main portion of the right hand side of Fig. 3.10 is the (color matched) scaling plot for each of the 3 temperature's shown on the left. These plots have also been vertically offset for clarity. Only the fractal region is shown here (i.e. between B_L and B_U), though this spans for nearly 1.5 orders of magnitude, a rather long scaling range for physical fractals [5]. The D_F values, obtained by the slope of these plots are 1.53 (red, 4.2 K), 1.39 (blue, 12K), and 1.26 (red, 20 K). Since $\alpha = 5 - 2D_F$,

the trend of decreasing D_F with increasing temperatures translates to an increase in α with an increase in temperature, consistent with the trend observed in the billiards.

The inset in the scaling plots (Fig. 3.10 right) shows the results of spectral analysis on the 4.2 K (red) trace. The scatter is typical for spectral analysis, and as such, in practice the α value is usually obtained through D_F. The solid line is a fit to power law $1/f^\alpha$ with α value of 1.94 obtained by the expression $\alpha = 5 - 2D_F$.
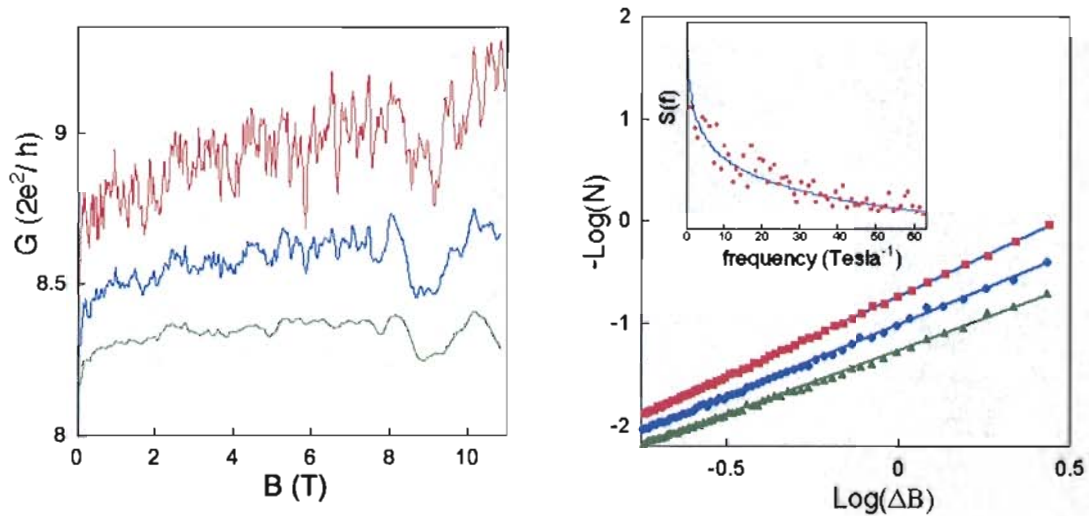
Figure 3.10. Left: MCF and analysis of diffusive Wire B. Temperature ranges from (top to bottom) 4.2K (red), 12K (blue) and 20K (green) traces have been vertically offset for clarity. Right: color matched scaling plots for Wire B at various temperatures (offset for clarity). Inset: spectral analysis of the 4.2K conductance trace showing a fit for the spectral exponent α given by $\alpha = 5 - 2D_F$ with D_F determined using the box-counting technique.

Wire C is a quasi-ballistic wire ($W < \ell_\mu < L$) that is defined by wet etching a two-dimensional electron gas (2DEG) formed at the interface of a GaAs/AlGaAs heterostructure grown using molecular beam epitaxy (MBE) [40]. Fig. 3.11 (left) shows MCF taken at four different temperatures for this wire. These MCF were

taken by J. P. Bird, a collaborator now at the University at Buffalo, New York, and provided to us for fractal analysis. The temperatures are (top to bottom) 42mK (blue), 246 mK (orange), 622 mK (green) and 910 mK(yellow).[3] Once again the MCF have been offset for clarity. The zero field conductance for each trace (top to bottom) is 42 mK, $G(B = 0) = 2.70$ $(2e^2/h)$, 2.50 $(2e^2/h)$ for the 246mK (orange) trace, 2.44 $(2e^2/h)$ for the 622 mK (green) trace, and 2.41 $(2e^2/h)$ for the bottom (910mK) trace. Again, as in the other two regimes, complexity of the MCF seems to fall off as temperature is increased.

On the right hand side if Fig. 3.11 shows the scaling plots for the color matched traces on the left of that figure. These have also been offset for clarity. The D_F value is obtained as the slope of each line. D_F values are 1.60 for the 42 mK (blue), 1.49 for 246 mK (orange), 1.41 for 622 mK (green), and 1.33 for the 910 mK (yellow) scaling plot. The inset shows the results of spectral analysis of the 246 mK (orange) trace. The solid line shows a fit to $\alpha = 2.02$, obtained by combining the scaling plot D_F value and $\alpha = 5 - 2D_F$

Wire D is also an n^+ GaAs diffusive wire. Eleven traces of the MCF of this wire were measured by R. P. Taylor while still at the University of Nottingham, in Nottingham, U.K. [44]. Temperatures ranged from 4.2 to 37.5 K. Wire E (also diffusive) was fabricated using MBE techniques in which the undoped GaAs layer is sandwiched between to Si doped AlGaAs layers and defined by EBL. Three traces

---

[3]These MCF were obtained using a dilution refrigerator, capable of reaching much lower temperatures than our ^{3}He system
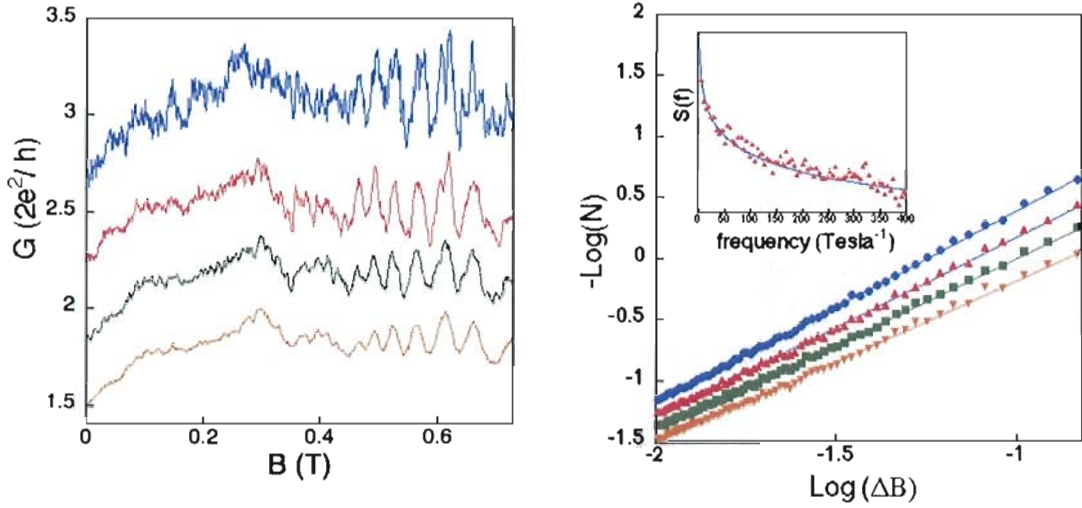
Figure 3.11. Left: MCF at various temperatures for the quasi-ballistic wire. (Wire C)Traces have been vertically offset for clarity. Temperature ranges from (top to bottom): 42mK, 246mK, 622mK, 910mK. Right: Scaling plot for device C at various temperatures. The slope of each line gives the fractal dimension (D_F) of the associated conductance trace. Temperatures are(top to bottom) 42mK, 246mK, 622mK and 910mK. Traces have been vertically offset for clarity. Inset: Spectral analysis of the T = 246mK conductance trace showing a fit for α, given by $\alpha = 5 - 2D_F$ with D_F determined using the box-counting technique.

of this wire were taken at 1.4 K. In this wire the experimenters [43](K. Ishibashi, our collaborator from Japan) modified the MCF by illuminating the sample with an LED. It is well documented that illumination has the effect of increasing the electron concentration.[19, 47–49].

Figure 3.12 plots the spectral exponent α for all wires listed in Table 3.1. Wires A to D all show an increase in α as the temperature is increased, similar to the billiards measured above. This plot only shows the data for temperatures below 30 K. The reason for this is that in all cases temperatures above 30 K led to smoothly varying MCF which no fine scale features, leading to $\alpha = 3$ (corresponding to D_F

=1). Although all wires show the increasing trend with increasing temperature, they certainly do not have the same slope, which would indicate that α is rising with T in the same manner. Similar to the results discussed with the billiards, this seems to indicate that a parameter other than T is better suited to chart the evolution of α.

This is further supported by the plot of Wire E (purple squares). These MCF were all taken at the *same* temperature ($T = 1.4$ K) and yet α changes. The change in α for Wire E can be understood by considering the area that is contributing to the MCF. Illuminating the wire increases E_F from 57.2 meV (dark) to 59.7 meV (long illumination). Increasing the carrier density means that more of the dopants donate their electrons, adding more impurities to induce scattering. This in turn will change the fine scale features of the MCF.
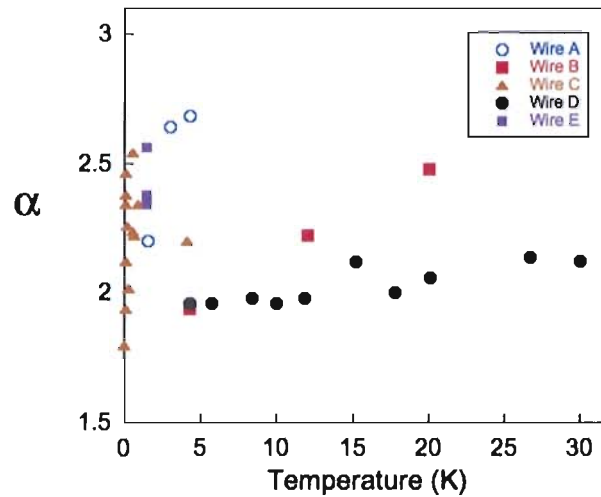
Figure 3.12.. α *vs.* T for the quasiballistic wire and the 4 diffusive wires.

This raises an interesting question: What is the relevant area associated with

these wires? In the billiards it was logical to use the active area of the billiard which was found by accounting for depletion. However in the wires this logic fails. This is due to the fact that in these regimes ℓ_μ is always smaller than at least one of the wire dimensions (L, W). In fact Wire C is 30 μm long and the electrons cannot possibly maintain phase over that entire distance. To find the relevant area we turn to Q. However before that can be done it is necessary to determine the length over which an electron can be expected to maintain it's phase. This length is called the phase-breaking length and is determined from the expression: $\ell_\phi = v_F \tau_\phi$. The Fermi velocity (v_F) is readily obtained from the Fermi energy (E_F), and τ_ϕ is obtained by the correlations field analysis discussed in Chapter II

Using Q to Determine the Wire Area Contributing to the MCF

If the Q curve holds over these regimes, then once a value for α is determined, the value of Q can ascertained by finding the area A that contributes to the MCF. All other material properties that appear in Q are known. In this process, it is assumed that the Q curve *does* hold. In principle 2 values of Q correspond to nearly all values of α. Given the relevant parameters of these regimes, it is safe to assume that these will lie on the steep side of Q $(Q < 1)$.

Wire E was the starting point. Once the α value was known, different areas that are physically reasonable are inserted into Eq. III.1 to see if they would put the α value onto the Q curve. When a suitable area is found, that value is labeled A_E.

If the process that was used to obtain A_E also places the remaining wires on the Q curve, than the original assumption that the wires would lie on Q is supported and justified.

The MCF from Wire E are shown in Fig. 3.13. This data set was also supplied to us as a rather high resolution image of the published plot and thus needed to be digitized. Both data sets are shown as an illustration of the effectiveness of the digitizing algorithm. The top (red) trace was taken while the wire was kept dark. The middle (green) trace was taken after a short illumination which increased the carrier density. E_F was estimated to increase from 57.2 meV to 57.7 meV. The bottom (blue) trace was taken after a longer illumination which gave the highest E_F of 59.7 meV. Application of the variational method box counting procedure yields D_F values of (top to bottom) 1.31 (red), 1.33 (green) and 1.22 for the bottom (blue) trace. Conversion to α provides a more intuitive feel for what is happening according to the high frequency content of the MCF. These values, (again top to bottom) are 2.37 for the top (red) trace, 2.33 for the middle (green) trace to 2.56 for the bottom (blue) trace.

With α values at hand, the next step in the process was to try various methods until obtaining an area A_E that would put this wire on Q for all three traces in Fig. 3.13. Figure Fig 3.14 displays the results of 5 different methods that were tried to obtain the area contributing to the MCF in wire E. The Q curve shown here is the same guide to the eye shown in Fig. 3.7. It is interesting to note that the wire area (red
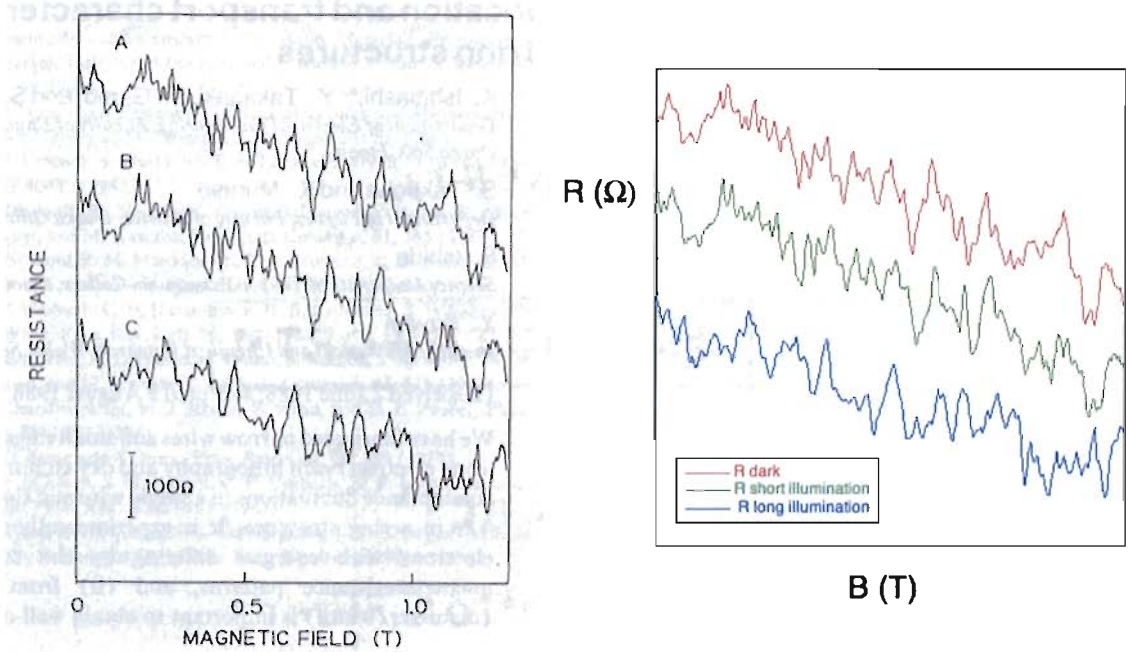
Figure 3.13. MCF of Wire E. The original rather high resolution image supplied to us alongside the results of our digitizing program. traces have been offset for clarity

squares) does actually place the points reasonably close to the Q curve (dashed line). However this process was ruled out as it seems to be physically unreasonable since ℓ_μ is roughly 10 times smaller than the length of the wire. This however introduced the idea that perhaps "phase coherent polygons" should be considered. The phase coherent triangle method (purple triangles) produced the smallest areas. This was an equilateral triangle whose perimeter was equal to the phase coherence length ℓ_ϕ.

The next smallest area was produced by a "polygon" method. The area of a

regular k sided polygon is given by [50]:

$$\text{Area}_k = \frac{kP^2}{16\tan(\frac{\pi}{k})} \tag{III.3}$$

Where P is the perimeter of the k sided regular polygon. Using Eq. III.3 with the perimeter set by ℓ_ϕ allows the area of a phase coherent k sided polygon $A_{\phi,k}$ to be calculated.

The next method was to determine the area for regular polygons whose side length was fixed by the mean free path ℓ_μ. This was done replacing the perimeter in Eq. III.3 with the relation $P_k = ka_k$. Where P_k is the perimeter of a regular polygon with k sides of length a_k. Setting the side lengths to be no longer than $a_k = \ell_\mu$ allows for calculation of the polygons area $A_{\mu,k}$ based on the idea that the side lengths should be $\sim \ell_\mu$. Areas were calculated using both of these methods. The upper bound on contributing polygons was chosen by the condition $A_{\phi,k} \approx A_{\mu,k}$ for the same number of sides k. The lower bound was set by the smallest possible regular polygon with perimeter ℓ_ϕ, a triangle. The area then used to determine Q was the average area of all polygons with k sides or less that met the criteria $A_{\phi,k} \approx A_{\mu,k}$.

The results of the polygon method are indicated in Fig. 3.14 by the brown diamonds. Other more self explanitory methods were tried, those being ℓ_ϕ^2 prompted by the fact that the Polygon method actually scales the term ℓ_ϕ^2, which can be seen by equating the perimeter P to ℓ_ϕ in Eq. III.3. The Q values obtained with this choice of area are displayed as green circles in Fig. 3.14. Finally, the value obtained by the product
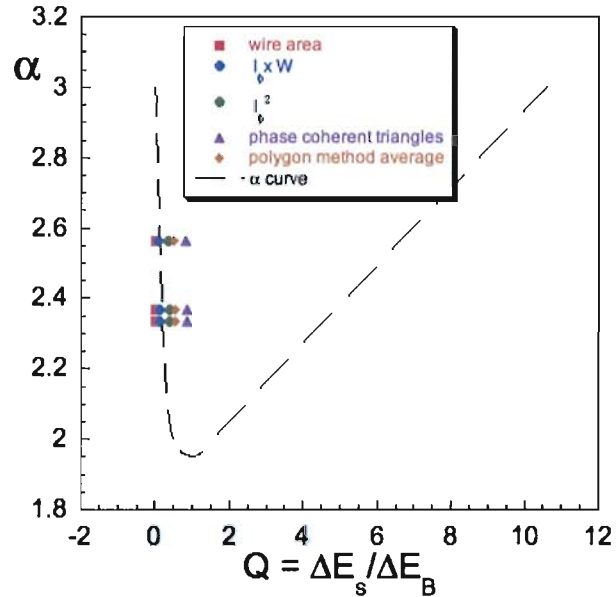
Figure 3.14. Illustration of 5 methods tried to obtain the relevant area contributing to the MCF of Wire E.

of ℓ_ϕ and the wire width W was tried, these values of Q are indicated by the blue circles.

Because both ℓ_ϕ^2 and $\ell_\phi \times W$ gave adequate results and should translate to the remaining wires in a physically realistic manner (i.e. unlike the total wire area) the method that was settled on was a hybrid "phase coherent polygon" method and $\ell_\phi \times W$. In this hybrid method the area relevant in Q is chosen as a "phase coherent subregion" which is defined to be the minimum between $\ell_\phi \times W$, and ℓ_ϕ^2. The results of this choice of area in determining Q are shown in Fig. 3.15 (left). The dashed line is the same guide to the eye provided in Fig.3.7. This choice of method for determining the area places the wires on the same Q curve as the billiards. To emphasize this, on

the left side of Fig. 3.15 is a plot of the α values for all billiard geometries shown in Fig. 3.4 as well as the α values for the wires.

The α values of all the geometries of Fig. 3.4 as well as those of all the wires listed in Table 3.1 are plotted against Q in Figure 3.15
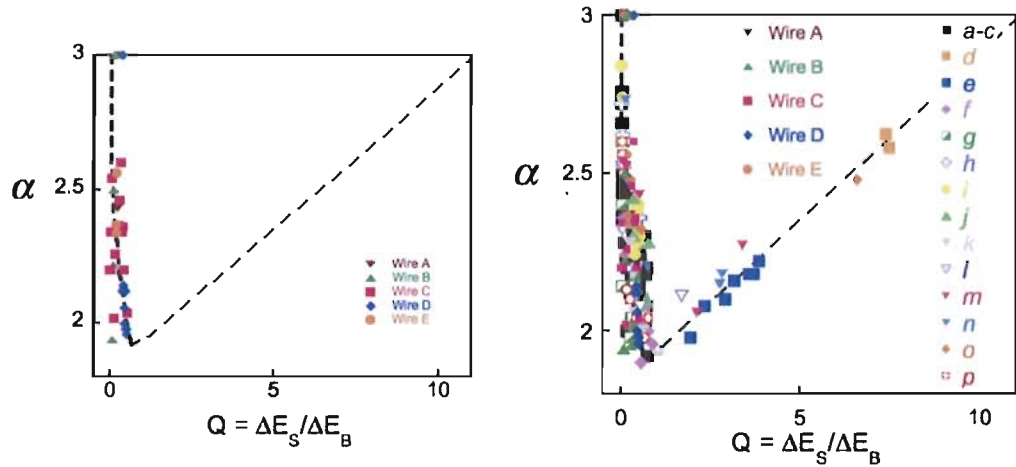
Figure 3.15. Left: α values for Wires $A - E$ plotted against Q value obtained using the phase coherent subregion method. The dashed line is the *same* guide to the eye used in Fig. 3.7. Right: Q curve will all device geometries shown in Fig. 3.4 as well as wires A-E

Conclusions

This Chapter began by introducing the Sinai billiard as a device that would exhibit both stable and chaotic trajectories. It was expected, by analogy to the classically chaotic system, that this billiard would lead to fractal conductance fluctuations due to a mixed phase space. Indeed it did, however it was shown that 10 other billiards defined in the same heterostructure produced FCF as well. Furthermore 5 additional billiards defined in a similar heterostructure were also shown to produce FCF. On top of that, when the α values associated with the FCF were plotted against the empirical parameter Q, All 161 FCFs were shown to lie on the same curve. The striking result that all the α values lie on the same Q curve was contrary to predictions[32, 51], and rules out billiard wall geometry as the origin of the chaos necessary to produce the FCF.

Other researches have predicted that the MCF would be sensitive to the potential energy profile of the billiard walls [12]. However, etched walls were shown to generate hard potentials [22], thus eliminating soft wall induced chaos. Especially in light of the fact that the 9 soft walled and 5 hard walled square billiards together produce an additional 116 MCF traces in which the associated α values lie on the same Q curve

This led to the proposal that perhaps the 'clean' billiard systems were more prone to material induced scattering than suspected. Remote, or modulation doping provides a buffer layer between the donor atoms and the 2DEG in an effort separate the electrons from their donors, thereby reducing scattering by the ionized impurities

left behind (the donors). It was proposed that these ionized impurities altered the potential landscape producing small angle scattering that is iterated by reflections off the billiard walls. Devices in which material induced scatterers lie in the plane of conduction were shown to produce MCF whose α values lie on the same Q curve. This supports the proposal that the origin of the chaos in the devices IS material induced scattering. The role of the walls is to iterate this process. The iterated non linear behavior then exhibits fractal scaling patterns, akin to the examples presented in Chapter I.

CHAPTER IV

THERMAL CYCLING

Introduction

The previous Chapter focused on charting the spectral exponent α, which characterizes the statistical nature of the magnetoconductance fluctuations. Specifically, the empirical parameter $Q = \dfrac{\Delta E_s}{\Delta E_B}$ was used as a measure of the discreteness of the energy levels in a device. When plotted against Q, α was shown to follow an identical trend regardless of the device geometry or the steepness of the potential profile. Furthermore, the *same* trend in α was shown to occur not only in the ballistic regime, but also to carry over the quasiballistic and diffusive regimes as well. This implies that material-induced scattering events play a pivotal role in the electron dynamics whether the scatterers are in plane, producing large angle scattering or they are remote, leading to small angle scattering. The experiment described in this chapter will further investigate the origin of the 'universal' conductance fluctuations. Noting that Ketzmeric was able to show that a mixed phase space was a requirement for fractal conductance fluctuations [12], this experiment will address the question "what is providing the chaos ?" To begin, this Chapter returns to the infinite horizon billiards mentioned in Chapter I

Revisiting the Infinite Horizon Billiards

The Sinai billiard can be described equivalently by either schematic of Fig. 4.1. In (a) the billiard is represented in analogy to a semiconductor billiard, whereas the schematic in (b) represents repeated reflections off of the billiard wall as an array of scatterers separated on all sides from each other by an equal distance. Let L represent the distance between each of the scatterers shown in Fig. 4.1 (b). If each scatterer has radius r, and the distance between the edges of two adjacent scatterers is W, then there is a channel of width $W = L - 2r$ in which a particle may move freely. If the square billiard in Fig. 4.1 (a) has side length L and that scatterer has raduis r, then both (a) and (b) would describe the same billiard, and thus exhibit the same dynamics. The schematic of Fig. 4.1 (b) represents an 'infinite horizon' billiards in that there are possible trajectories which would not reflect off a billiard wall [52]. Reflections off of billiard walls of Fig. 4.1 (a) serve to repeat collisions with the scatterer. This replicates the multiple scatterers of the array in (b). Researchers in Ref. [52] found that the Sinai billiard was *superdiffusive*, in that the mean square of the displacement grows faster than linearly [53].

There are, of course, some trajectories for which this superdiffusive transport seems logical, if not expected. Consider for example a trivial trajectory in which a particle's initial velocity is oriented exactly parallel to and in the middle of one of the channels in Fig. 4.1 (b). Such a trajectory would certainly be expected to travel faster than a random walk ($< x^2(t) >$ grows linearly). In fact the other significant
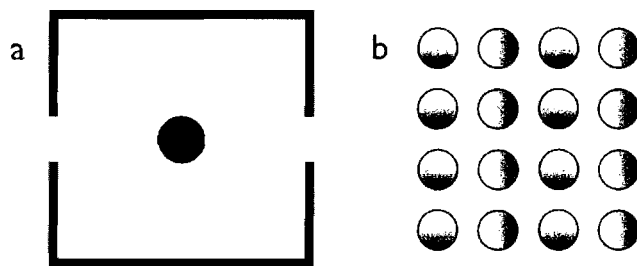
Figure 4.1. Two representations of the Sinai billiard a) Traditional schematic of the Sinai billiard and b) analogous schematic, illustrating the Sinai billiard as an infinite horizon billiard.

contribution of Ref. [52] was that the authors were able to show that this superdiffusive transport held even when such trivial trajectories were forbidden. Furthermore, they were able to show that this behavior held for a modified Sinai billiard such as that illustrated in Fig. 4.3.

Consider the two models of billiards depicted in Fig. 4.2. Panel (a) shows the same infinite horizon Sinai billiard shown in Fig. 4.1, in which superdiffusive (i.e. enhanced diffusion) transport is expected. If the location of the scatterers is randomly oriented the result is regular diffusive transport.
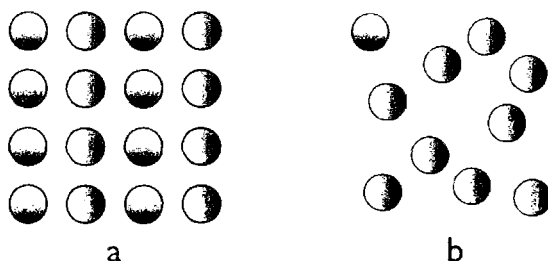
Figure 4.2.. Regular (a) and randomly oriented (b) Sinai scatterers

Panel (a) of Fig. 4.3 shows the infinite horizon version of the Sinai billiard in which each of the scatterers has a radius r, and is situated on a square lattice with a center to center distance of L. The modified version (panel b) has each of the scatterers randomly displaced. The magnitude of the displacement is no greater than $\Delta < (L/2 - r)$ which ensures that there will be channels allowing free motion. The modified Sinai billiard, with the above constraints, was shown to exhibit superdiffusive transport [52].
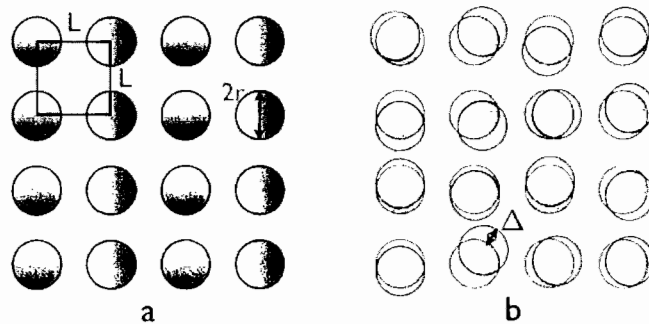
Figure 4.3. (a) Regular and less randomly (b) oriented Sinai scatterers. The red crcles in (b) are constrained such that the magnitude of displacement is limited by $\delta < L/2 - r$, but are randomly oriented in direction.

To illustrate the difference in transport between the random distribution of scatterers in Fig. 4.2 and the constrained random distribution array in Fig. 4.3, consider the feasibility of long range trajectories between scattering events. The completely disordered array will result in a Gaussian distribution of trajectory lengths with dynamics well described by Browinan motion. Long range trajectories will be much more likely in the constrained array. Enhanced diffusion implies that a trajectory will tend towards continuing its current direction. If this enhanced diffusion is sufficiently

strong, it leads to a power law distribution of path lengths, called Lévy Flights [8, 54].
Figure 4.4 distinguishes an example of results for these types of motion. The Gaussian
distribution, leading to Brownian motion, is shown alongside a Lévy flight with the
same number of steps. Both paths were started at the same origin in the upper left
corner of their respective panels, and run through the same number of steps. The
color changes to indicate increasing number of steps, beginning with red and ending
at violet.
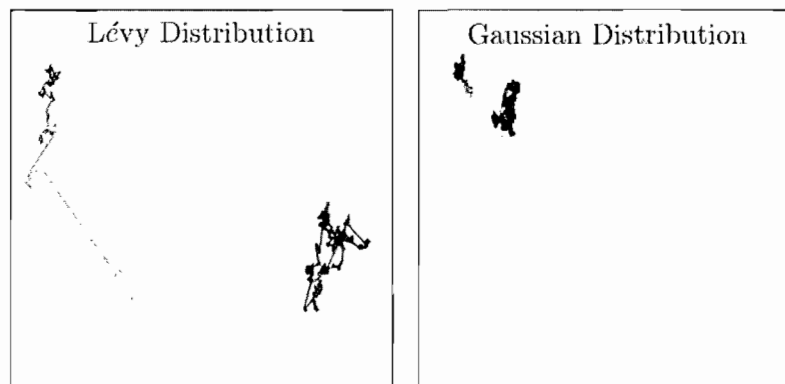
Figure 4.4. Simulation of a (left)Lévy flight and (right) Brownian motion. In each
case, the path starts in the upper left hand corner (indicated by red) and continues
for the same number of steps before terminating (violet). The step length follows a
power law for the Lévy flight and a Gaussian distribution for the Brownian motion.

Thermal Cycling Experiment

The constrained disorder of Fig. 4.3 offers an appealing analogy to our billiard
systems. The modulated doping techniques used to enhance carrier density and
reduce large angle scattering were expected to provide a very clean conducting plane
in the 2DEG. However this chapter proposes that remote ionized donors play a

more vital role in the electron dynamics than previously considered. Modulation doping techniques do reduce scattering from the ionized donors. However they do not eliminate scattering. Since the donors are remote, $\sim$ 20nm above the 2DEG in our etched billiards, the Coulomb interaction due to the ionized donor does not act as a hard scatterer. Rather, it alters the potential landscape in the 2DEG such that rather than a flat plane, electrons traversing the 2DEG are subject to an effective potential that has a rolling terrain. In this view, the hills and valleys are much smaller than E_F, promoting small angle scattering throughout the 2DEG. This effective potential was introduced and imaged in 2001 by researchers at Harvard University and well publicised [37–39]. Furthermore, our collaborators at the University of Cambridge, UK, obtained scanning probe images of the wavefunctions in an AlGaAs/GaAs billiard, and show that they were fractal [55]. The experiment described in this chapter seeks to answer the question "Why are the spatial patterns formed by the wavefunctions fractal?". The proposition is that the role of the billiard walls is to iterate the small angle scattering resulting from the roughened potential terrain. By feeding the traversing electrons back through the hilly terrain, this iterated small angle scattering is what leads to the fractal nature of the MCF.

Background

To remove any doubt that the softness of the potential is not contributing to the fractal character of the MCF, this experiment is conducted on the etched billiards. A schematic of the heterostructure is presented alongside an atomic force micrograph of

a square billiard representing the geometry of the billiard on which this experiment will be focused.
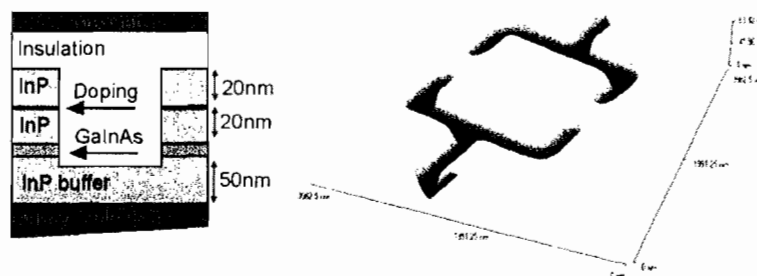
Figure 4.5. Left:GaInAs/InP heterostucture of the etched billiard system and Right: Atomic force micrograph of the billiard geometry investigated in the thermal cycling experiment.

Figure 4.6 shows the electron phase coherence length, ℓ_ϕ, as a function of temperature for the square billiard. The phase coherence length was obtained using the Correlation Field method discussed in Ch. II to determine τ_ϕ and then using the relation $\ell_\phi = v_F \tau_\phi$. This plot illustrates that ℓ_ϕ remains at least as large as the billiard width up to 7K.

<center>Geometry Induced Background of the MCF</center>

In the right hand section of Fig. 4.7, are several MCF for the square billiard shown schematically at the top of that panel. Traces were taken at temperatures of (top to bottom) 12K, 5K, 2K, 1K, 500mK and 12 K as indicated below each trace in that panel. Electronic transport measurements were taken in a four terminal, constant current configuration using standard AC lockin techniques at a frequency of 37 Hz.
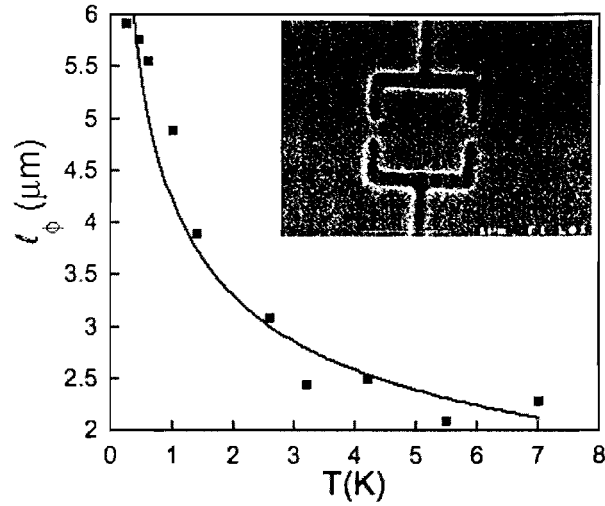
Figure 4.6. Phase breaking length(ℓ_ϕ) plotted against temperature (T) in the etched square billiard shown in the scanning electron micrograph inset.

The top trace, taken at 12K , is relatively smooth because the fine scale quantum interference effects of conductance G with respect to applied magnetic field B have been scattered away by thermal excitation. What remains is a background variation in G which is proposed to be induced by the device geometry. In support of this proposal, a similar cascade of MCF taken at the same temperatures (indicated in the leftmost panel) for billiards with different shapese are shown in the remaining panels of that figure.

The geometry of each device is indicated schematically at the top of the panel. In the center panel is a triangle exhibiting horizontal symmetry about its midline. An electron entering the billiard from the left hand side of this billiard is exposed to the same local geometry whether it travels up or down, and thus this billiard will

be referred to as the UD triangle (Up Down symmetric) or simply UD. Similarly, the billiard schematically shown in the rightmost panel will be referred to as the LR triangle or LR since it is symmetric with respect to a vertical axis running from the center of its base through its apex.
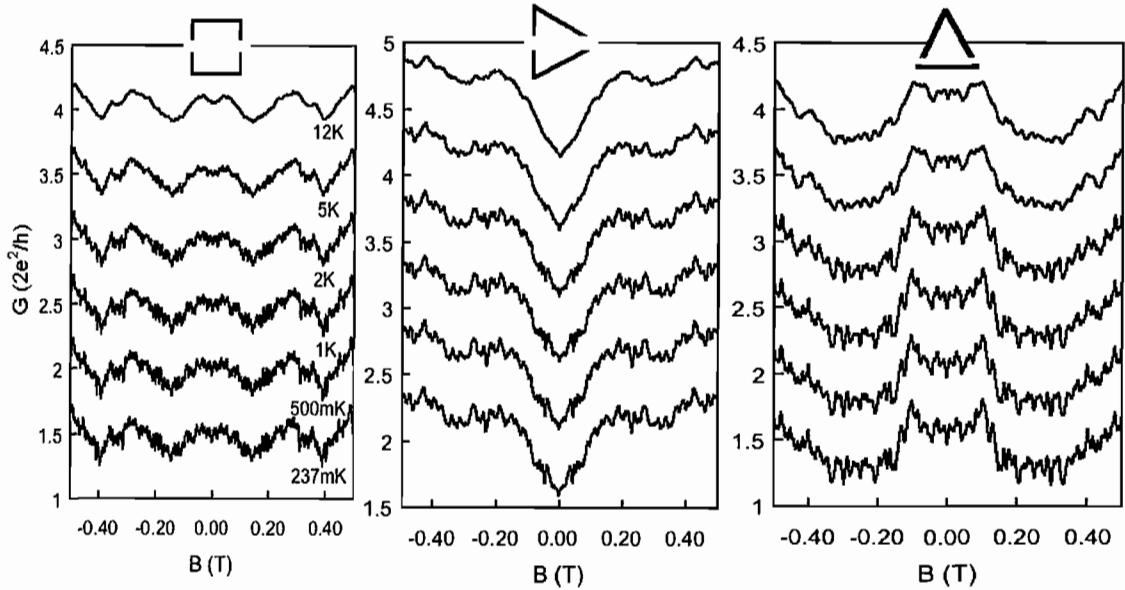
Figure 4.7. Magnetoconductance fluctuation traces taken at various lattice temperaures of a square billiard and two triangular billiards illustrating the geometry induced classical background features of the MCF. Traces have been offeset for clarity In each case lattice temperatures are (top to bottom)12K, 5K, 2K, 1K, 500mK and 237mK.

While the background trend (i.e. long magnetic period oscillations) is the same for traces within each panel of Fig. 4.7 , it is quite different when comparing individual panels representing different billiards. The fact that this background trend remains well after the fine scale features have been suppressed by warming the billiard to 12K indicates that it has a classical origin. This conjecture is further supported by Fig. 4.8 which shows MCF traces taken on different billiards which are on different Hall bars

and at different temperatures. Both MCF displayed in Fig. 4.8 were taken on square

billiards that were fabricated to lithographically have the same dimensions. The top

(red) trace is the same data set shown in the 12 K square billiard trace of Fig. 4.7 (top

left trace). The blue trace in Fig. 4.8 was taken on the Hall bar named H3 which was

used in the thermal cycling experiment to be described below. Despite the fact that

these two billiard lie on different mesas, the background trend is remarkably similar,

in contrast to the marked difference in the long magnetic period smoothly varying

trends of the square billiards and the UD or LR triangles.
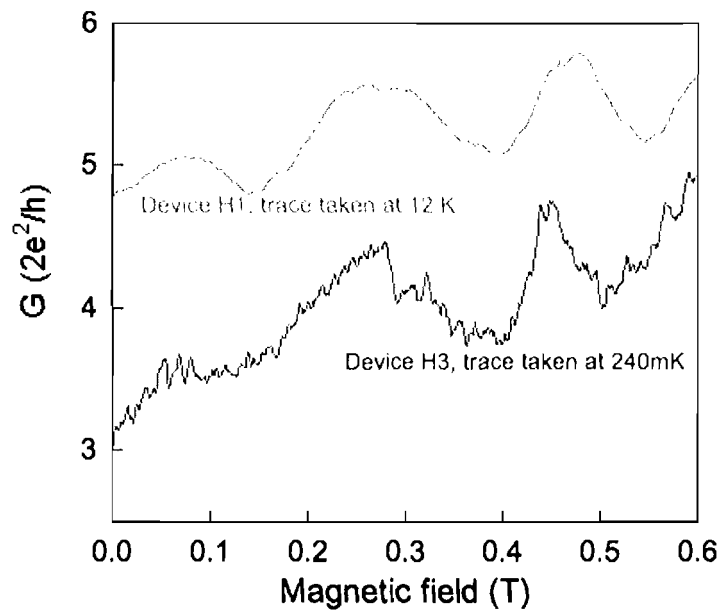
Figure 4.8. MCF of two square billiards on different Hall bars taken at different temperatures but with roughly the same mean conductance. A possible source of the small variations in the backgrounds could be the differing mean conductance values.

The small deviations in the background trends of Fig. 4.8 could be a result of

differences in depletion due to the edge states near the etched barrier. In that case,

the small differences are simply a consequence that the billiards, while lithographically designed to be the same, had very minor variations in later steps of the fabrication such process (i.e. etching, insulation or top gate deposition). Alternatively, it may be a consequence of the fact that the two traces were taken at slightly different gate voltages. In the case of the red trace (H1), the mean conductance was $< G > \sim 2.8(2e^2/h)$, whereas $< G > \sim 3.5(2e^2/h)$ in the blue (H3) data set. The small difference in $< G >$ may be responsible for the slight discrepancies in the two background trends. To illustrate this, consider two traces taken at different conductance plateaus. Conductance through a QPC is known to be quantized in units of $2e^2/h$ [18, 19], and was first shown to exhibit this behavior in an AlGaAs/GaAs systems simultaneously by two groups [56, 57]. In both experiments the application of gate voltage was used to reduce the width constriction of the QPC, allowing conductance through more modes to transport through the device. A similar plot of the conductance through the square billiard H1 as a function of gate voltage is provided in Fig. 4.9. Note that the quantized steps do not occur at integer multiples of $2e^2/h$. This is presumably due to the fact that the construction of a billiard requires an additional QPC, and conductance through the billiard is further suppressed by interference within the confines of the billiard. Nonetheless, the steps themselves are nearly separated by $2e^2/h$, and further discrepancies can be accounted for if one subtracts off the resistance of the bulk material between the QPCs and Ohmic contacts which are assumed not to contribute to the resistance [46].
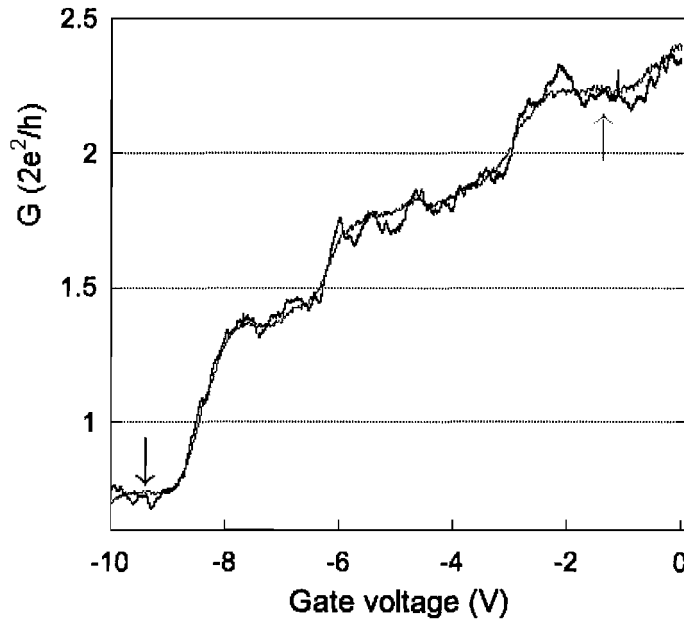
Figure 4.9. Conductance vs. gate voltage for a square billiard. The blue trace is taken at base temperature, while the red trace is taken at T= 5K. The (color matched) arrows indicates plateaus in conductance that magnetic field sweeps of Fig. 4.10 were taken.

The arrows in Fig. 4.9 indicate two plateaus in conductance. The arrows indicate the gate voltages that the MCF of the square billiard on mesa H1 shown in Fig. 4.10 were measured. The bottom (blue) trace was taken on the lowest plateau of Fig. 4.9 indicated by the blue arrow. Similarly the red arrow on Fig. 4.9 indicates the plateau on which the top (red) trace was taken. The typical experimental procedure is to perform a gatesweep, as shown in Fig. 4.9, to find a gate voltage at which stable (i.e. fairly long) plateaus occur, ensuring the magnetic field sweep (i.e. MCF trace) does not coincide with a transition in the number of modes in the QPC. The effect of the number of modes through the billiard can be seen in Fig. 4.10. The background trend

is considerably more pronounced in the high mode (red) trace as compared to the low mode (blue) trace. In particular, the dip in zero field conductance (known as a weak localization peak and due to coherent backscattering of electrons [18, 19, 58]) is much more pronounced in the high mode trace. This can be interpreted as a higher number of modes leading to more pronounced backscattering. In each case (i.e. high or low mode) the backscattering is suppressed by a non-zero magnetic field. The data sets in this figure have not been offset to emphasize the difference in the mean conductance $(< G >)$ of each trace. This is an extreme example of the difference that can occur in the MCF as a result of altering the number of accessible modes in the billiard. In the case of Fig. 4.10 the high mode trace was taken three plateaus higher (i.e. 6 more modes in each QPC) than the low mode trace which corresponds to $< G > \sim 2(2e^2/h)$. It is extremely unlikely that the small difference in $< G >$ in the two traces of Fig. 4.8 would lead to any more than a 1 plateau difference, thus leading to background trends more similar than those shown in Fig. 4.10. Again, aside from the difference in the magnitudes of the weak localization peaks, the overall background trends of the two traces in Fig. 4.10 are quite similar. Considerably more similar than a comparison of the square and the UD or LR triangle (or comparison of the two triangles).

Further support for the background trends being geometry induced is offered in Fig. 4.11. In this figure the 12K and base temperature (236 mK) traces of the square billiard and the UD triangular billiard are reproduced along with insets
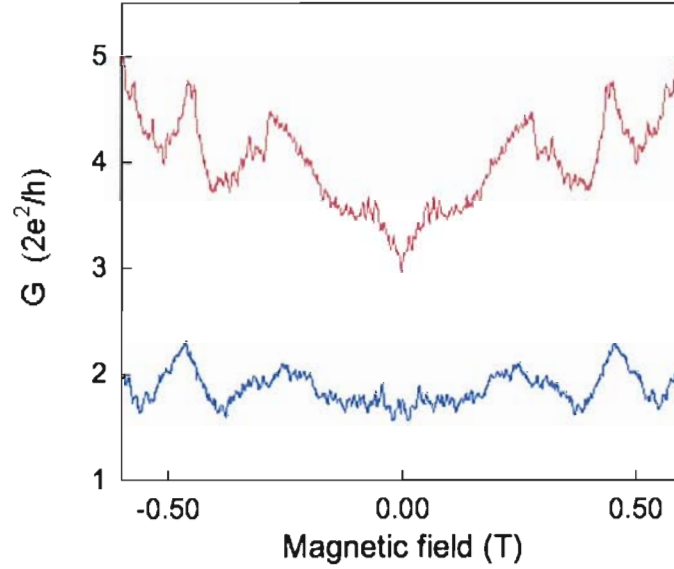
Figure 4.10. MCF in a square billiard taken at different conductance plateaus. Traces taken at base temperature ($\sim$ 240 mK), The color of the trace matches the arrows in Fig. 4.9. The traces Have NOT been vertically offset.

schematically depicting the electron trajectories leading to a few selected features of each background trend. In each case, the electron trajectory has been approximated based on the ratio of the magnetic field B at the indicated arrow to the cyclotron field B_{cyc}. The radius of the circular trajectories that undergo specular reflection is determined by the corresponding ratio to r_{cyc}, defined as the radius of the circle that circumscribes the billiard. The relation between B_{cyc} and r_{cyc} is $B_{cyc} = \sqrt{2\pi\, n_s}\dfrac{\hbar}{e\, r_{cyc}}$. Consider for instance the middle schematic of each billiard. Both show a possible set of trajectories of an electron in a magnetic field applied normal to the plane of the billiard with magnitude $B = B_{cyc}$. In the case of the square billiard, one possible trajectory is that of a single reflection off the top wall resulting in rapid exit from

the billiard, giving rise to an enhanced conductance at that B field. In contrast, the trajectory associated with $B = B_{cyc}$ for the triangular device results in reduced conductance.
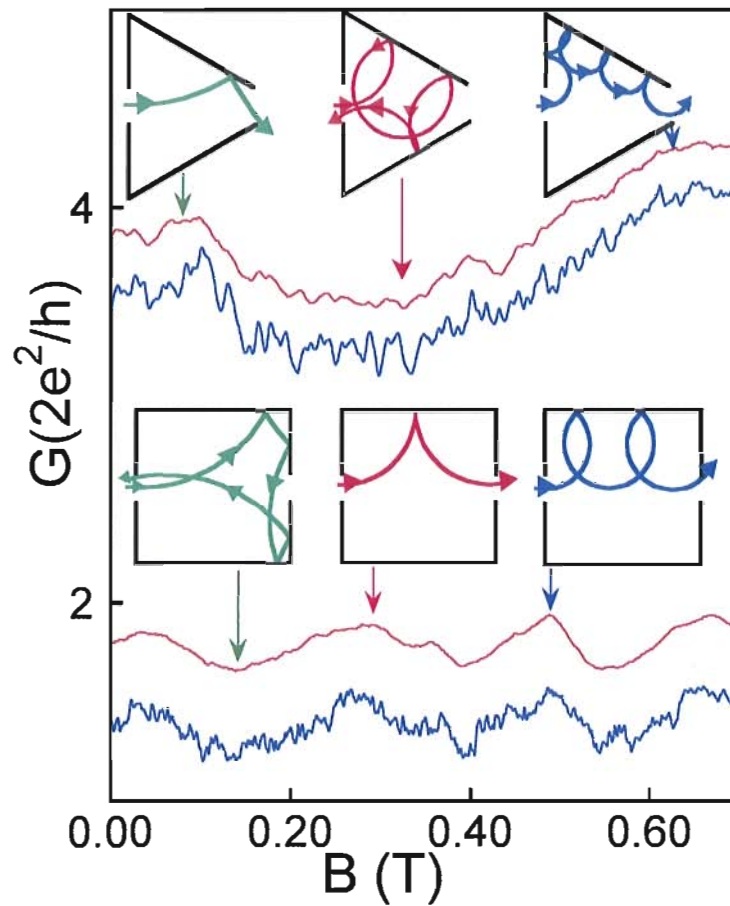
Figure 4.11. MCF traces of the square and triangular billiards taken at 240mK and at 12K are offset for clarity. Insets: schematic representations of possible trajectories geometrically influenced by the billiard walls, corresponding to local maxima and minima in the conductance. Trajectories are based on the ratio the magnetic field to the field that allows a single circular trajectory to circumscribe the billiard (B_{cyc}). For the square billiard the fields shown are (left to right):1/2 B_{cyc}, B_{cyc}, 3/5 B_{cyc}. For the triangular billiard $1/4B_{cyc}$, B_{cyc}, and $2B_{cyc}$.

The differences between the trends of each billiard illustrates that the shape of

the billiard influences the background trend of the device. The fact that the same background trend persists in the MCF taken at 12 K indicates that this background is classical, and not a quantum interference effect, because the phase-breaking length is smaller than the billiard width at that temperature. The similarities between the background trend of the two different square billiards corroborates this, especially in light of the fact that the differences in those traces are far more subtle than the differences in traces from the same billiard taken at different gate voltages. Apart from the notable difference in the weak localization peak, which *is* a quantum interference effect, the overall background of the two traces taken at different gate voltages is quite similar. This serves as further indication of the classical nature of the background trend. Finally, trajectories that either lead to a reduced or enhanced conductance are illustrated to correspond to major peaks and dips in the MCF, consistent with the proposition that the 12 K (top) traces in Fig. 4.7 represent a classical background trend that is induced by the billiard geometry. Together this represents strong evidence to establish that the role of the geometry of the billiard wall configuration is to define the background trend of the MCF.

Effects of Bringing a Billiard to Room Temperature

Having addressed the long range smoothly varying background trend of the MCF, this section will focus on the fine scale fluctuations (i.e. features of period ~ 0.1 T) superimposed onto the geometry-induced background. In addition to dictating the background trend, the billiard walls (regardless of their geometry) repeatedly

reflect electron trajectories back across the electrostatic potential landscape that forms the conducting plane of the billiard. Modulation doping ensures that the potential landscape is rather smoothly varying, producing slight (i.e. small angle) alterations in the trajectories. Thus the walls of the billiard play the additional role of providing iteration, in the sense that they promote the replication of chaotic scattering processes.

It is well documented that the conductance fluctuations are repeatable [32, 51, 59]. MCF traces taken on the same device separated by several months are known to have the same fractal dimension. This has been illustrated previously by two MCF traces taken a month apart on the same billiard. These two traces are presented again in the left hand panel of Fig. 4.12. During the month between these two MCF traces, the billiard was kept at low temperatures. The right hand side of Fig. 4.12 shows the results of bringing a billiard to room temperature between magnetic field sweeps (MCF measurements). Although the overall statics of the MCF, as measured by D_F, remain unchanged, when a device has been brought to room temperature between MCF sweeps, the fine scale features of the MCF are often quite different. This is illustrated by the right hand panel of Fig. 4.12 which shows three MCF data sets taken on a square billiard (H3). These MCF were taken after successive trips to room temperature and back to base temperature. The difference in the fine features of the MCF are quite noticeable when comparing the traces separated by trips to room temperature.
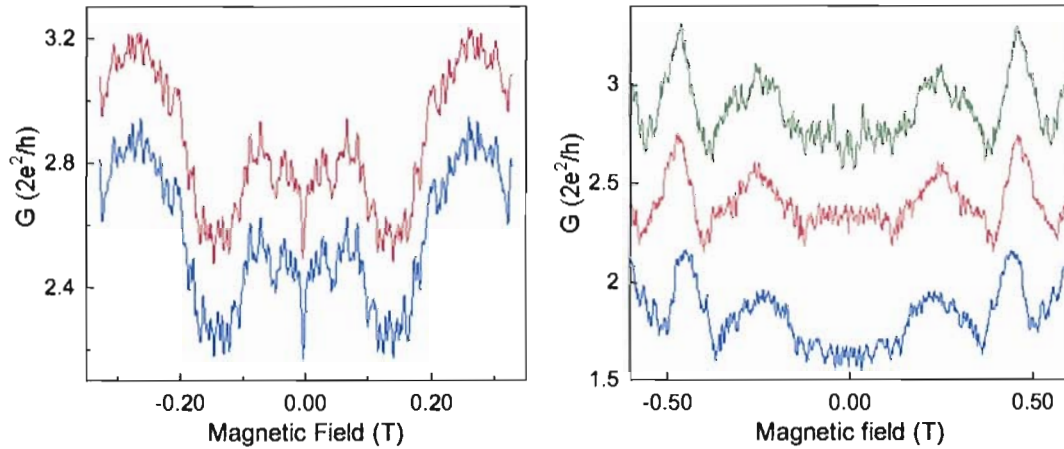
Figure 4.12. The effect of room temperature thermal cycling on MCF. Left: MCF of a square billiard (H1) taken ~ 1 month apart while the sample temperature was kept at $T \leq 12$K. Right: Three MCF of a different square billiard (H3) taken within 2 weeks of one another. The sample was warmed to room temperature and returned to base between measurement.

The traces on the right hand side of Fig. 4.12 were taken during a two week period of this experiment. After the data set represented by the blue trace was measured, the billiard was allowed to warm to room temperature. Upon being brought back to base temperature, the data represented by the red trace was measured. This process was repeated prior to measuring the data represented by the green trace. In contrast the traces on the left had panel of the same figure were taken nearly a month apart during which time the billiard temperature was only raised as high as 12 K. Specifically, on separate magnetic field sweeps during that experiment the device temperature was controlled at 1K, 5K, 8K,(twice) as well as 12K.

Despite the differences in the fine scale features of the data sets in the right panel of Fig. 4.12, all three of those traces have the same fractal dimension. This is evidenced

in Fig. 4.13 which shows the scaling plot resulting from a variational box count on the traces in the right hand panel of Fig. 4.12.
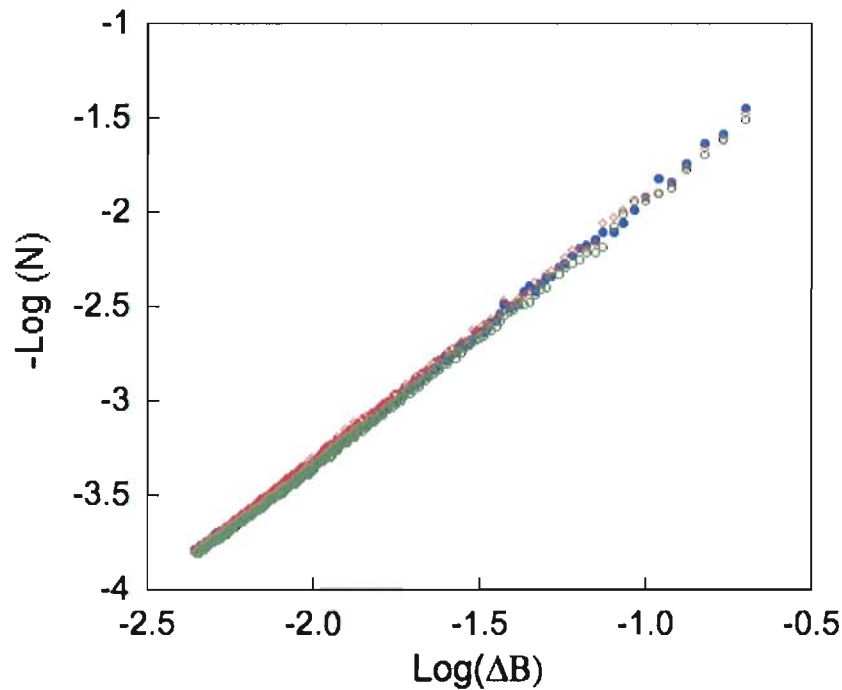
Figure 4.13. Scaling plots of the three (color matched) MCF traces of the right hand panel of Fig. 4.12. The fractal dimension D_F is obtained from the slope of this plot.

The data points in the above scaling plot are color matched to their corresponding data trace in Fig. 4.12. The scaling plot data has not been offset, but has been truncated to display only the fractal region (i.e between B_L and B_U). The scaling plots are identical, within the noise level, and their slope defines the fractal dimension (D_F) of the MCF. Clearly D_F is the same for all 3 magnetic field sweeps and shows that the deviations in the fine scale features that result from bringing the billiard to room temperature between conducting magnetic field sweeps (at 240 mK) do not

alter the statistics of the MCF. These fine scale changes are not noise, as is evidenced by the two month long separated traces shown in the right hand panel of Fig. 4.12.

It is clear that raising the billiard to an intermediate temperature T_i as high as 300 K has a very different effect on the fine scale features of the MCF than raising to say 12K. The fine scale features are *critically* sensitive to the precise configuration of the scattering sites, created by the impurity induced potential landscape [58]. One way to envision this is to imagine an electron traversing the billiard in the presence of soft angle scatterers. The trajectories through the billiard will depend on the exact geography of the scatterers. Since the MCF arise due to interference of wavefunctions, slight alterations in path length will yield alterations in the fine scale features of the MCF. For this reason, the MCF are often referred to as a "fingerprint" of the precise configuration of the scattering sites [51, 58, 59].

The process of warming the billiard has been previous described as an annealing process that redistributes the scattering configuration of impurities [58]. It is possible that the small changes in the fine scale features that occur as a result of warming to room temperature involve a re-distribution of the hills and valleys in the potential landscape. The structure of the potential landscape is a result of the charge state of the individual donors in the doping layer. These small hills and valleys are acting as nanoscopic Sinai diffusers, and altering their location slightly is consistent with the "mildly disordered" modified infinite horizon billiard represented in Fig. 4.3. For instance, if two neighboring donors "swapped" an electron (i.e. each changed their

charge state) then where there was a hill, there would now be a dip in the potential landscape, and vice versa.

The MCF are a result of wavefunction interference due to the phase differences that accrue as as an electron traverses the billiard. Small alterations in the configuration of the terrain will lead to small changes in the path lengths of an electron's journey through the billiard. Consequently, this will result in a slight difference in the accumulation of phase, which is precisely what leads to the interference that produces fluctuations in the conductance (i.e. MCF).

The experiment this chapter describes is designed to address the proposal that bringing a billiard to room temperature introduces enough thermal energy to re-distribute the precise scattering configuration of the impurities (Sinai diffusers). The fact that D_F remains static despite this reconfiguration seems to imply that statistically the system does not change. In other words, bringing a billiard to room temperature does not change the number of dopants that are contributing to the roughening of the potential terrain. However the precise configuration of this terrain does change. More precisely the dopants themselves do not need to relocate, rather some of them will change their charge state.

There are two mechanisms that can accomplish this. Either a neutral donor becomes ionized, and vice versa, thus maintaining the statistics of the potential landscape. Alternatively the presence of an additional trapped state could accommodate the needed alterations in a similar manner.

Si is known to exhibit such a trapped state, which is a deep donor level known as a DX center [60, 61]. The origin of the name DX is that the trap is formed deep within a substitutional donors atom (D) and an unknown lattice defect (X). DX centers are associated with the donors in III-V semiconductors. Evidence of a DX center in InP doped with S has been reported [62]. Similar traps in InAlAs/InP were reported, but these researchers concluded that the trap was not a DX center[61]. Regardless of the exact form of the trap, a trapped state remains a candidate for the reconfiguration of the scattering terrain.

This is an intriguing model. However with the data set provided thus far we cannot answer the question: How much energy is needed to produce the redistribution, and is there a threshold energy, or is the redistribution more of a smooth transition? Furthermore the scaling plots of Fig. 4.13 clearly indicate that D_F (thus α) cannot indicate the presence of such a re-distribution, though the MCFs themselves can, as evidenced by the traces on the right hand side of Fig. 4.12.

The Experiment

To address the question of the energy requirement necessary to bring about the redistribution, the following experiment is performed. The billiard is brought to base temperature, and a base temperature magnetic field sweep is conducted to measure the MCF. The sample is then brought to some intermediate temperature T_i, and held there for a period of time t_H. The billiard is then brought back to base temperature

where another MCF data set is measured. This process is repeated for a variety of T_is, thereby building a catalog of pairs of base temperature traces that have been warmed to some T_i and then cooled back down between data collections.

Prior to each magnetic field sweep a gate voltage sweep was performed to ensure that for each pair of T_i separated data sets has the same number of modes in the QPC. Magnetic field sweeps were conducted at 2 plateaus of the G vs. V_g plots. High mode (n=6) and a low mode ($n = 2$) for each T_i. The value of t_H was fixed at 30 minutes throughout this experiment. A sample of each of the two modes MCF are shown in Fig. 4.14. The High mode trace is indicated in red and the low mode is in blue. The blue (low mode) trace has been vertically offset for clarity.
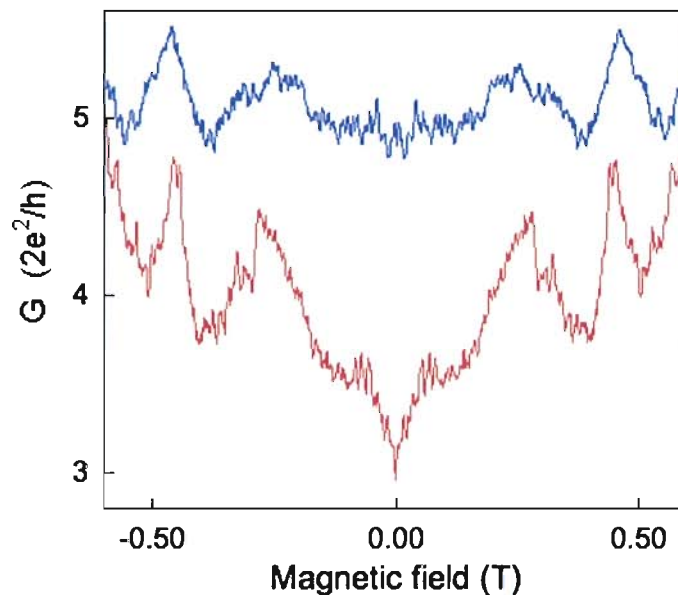
Figure 4.14. An example of the high mode (red) and low mode (blue) MCF taken during this experiment.

Results

Figure 4.15 shows a sample of the data collected. Three pairs of traces are shown, separated by (bottom to top) $T_i = 240$ mK, 115 K and 300 K. The bottom pair of traces in the main figure were held at base temperature between measurements and traces are virtually identical.
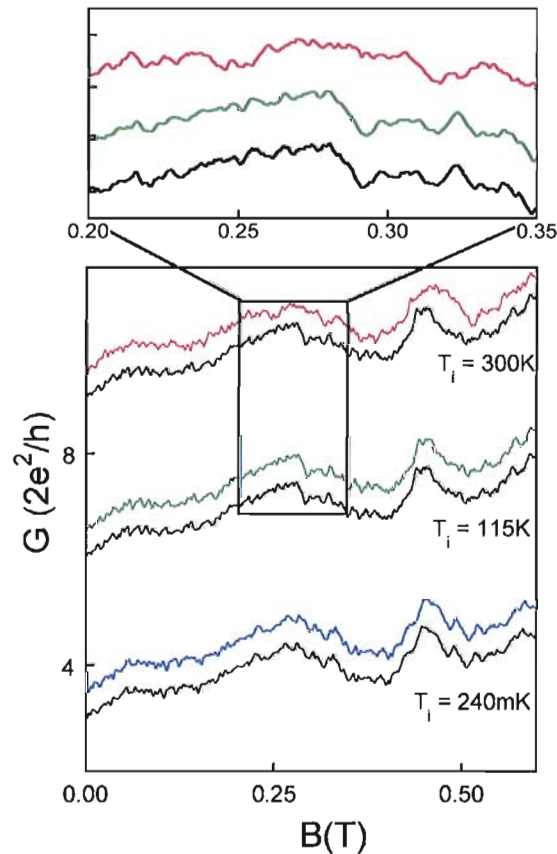
Figure 4.15. Comparison of MCF in the square billiard after being warmed to 3 intermediate temperatures (T_i). Between each trace the billiard was held at the temperature T_i for 30 minutes before being brought back down to base temperature and a magnetic field sweep was obtained. Traces have been off set for clarity. Traces in the bottom pair were taken while the billiard remained at base temperature. Top: Magnified comparison of traces taken with $Ti=115$ K (green and black) and $T_i =300$K (black an red)

The pair of traces separated by $T_i = 115$ K are quite similar in fine scale structure as can be seen by comparison of the middle pair of traces in Fig. 4.15. However, when T_i is above 120K as in the top pair of traces, the fine scale fluctuations are quite different. This distinction is made more clear by examining the small range of magnetic field as shown in the top plot of Fig. 4.15. Once again, a variational box count analysis cannot probe the thermal re-distribution of the Sinai diffusers. This is most likely because the bulk qualities (i.e. μ, ℓ_μ, n_s) are consistent in each magnetic field sweep. Also there is no reason to expect that τ_ϕ nor ℓ_ϕ will change. The sample is returned to base temperature after being held a T_i and gate sweeps ensure that V_g is set so that the number of modes and E_F are consistent within pairs of traces. Indeed, if there were a change in τ_ϕ this would result in a change in Q and D_F would be sensitive to it.

To quantify the difference in the fine scale features of two traces R_1 and R_2, the point by point root mean square of their differences is calculated. It is important to ensure that each trace has the same mean value of resistance $< R >$. Subtracting $< R_i >$ off of each trace will give both traces a mean value of 0. In essence this is the measure of the deviation of R_2 with respect to R_1, hence the name σ:

$$\sigma(R_1, R_2) = \left\langle \left(\tilde{R}_1 - \tilde{R}_2 \right)^2 \right\rangle_B^{\frac{1}{2}} \tag{IV.1}$$

Where $\tilde{R}_i = R_i - \langle R_i, \rangle_B$.

Figure 4.16 illustrates the results of the correlation analysis by plotting the value of σ (labeled Corr) against T_i for both the high(red) and low (blue) mode traces. Note that the correlation analysis is done on the resistance traces (in Ωs), directly obtained from our measurements rather than the conductance G. [1] Thus, the resulting lower magnitude σ, or apparently better correlation of the high field MCF is expected since a higher $<G>$ means a lower $<R>$. For both modes however, there is a marked transition at $\sim$ 120 K .
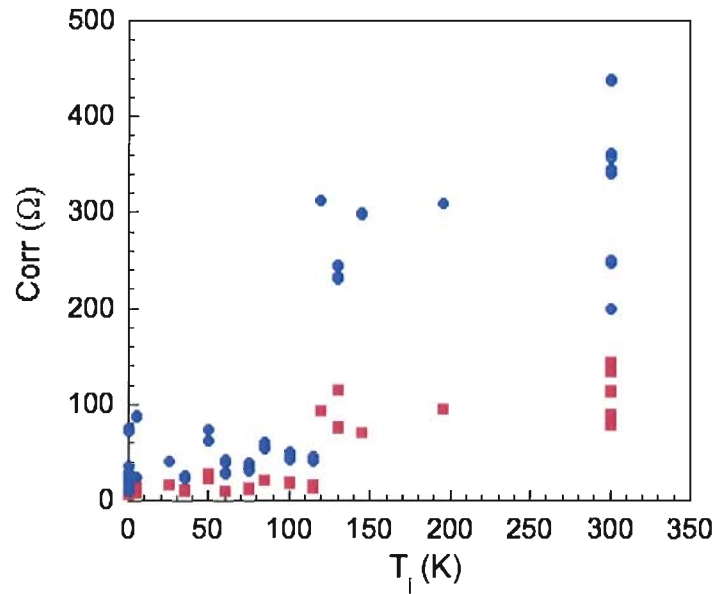
Figure 4.16. σ plotted against T_i for both the high (red) and low (blue) mode traces.

To further quantify this transition we employ a correlation function defined as:

$$F(R_1, R_2) = \left\langle \frac{\left\langle (\Delta R\,(B))^2 \right\rangle - \left(\tilde{R}_1\,(B) - \tilde{R}_2\,(B) \right)^2}{\left\langle (\Delta R\,(B))^2 \right\rangle} \right\rangle_B^{\frac{1}{2}} \qquad \text{(IV.2)}$$

---

[1]G is the parameter most often reported in literature

Where $\tilde{R}_i$ is as defined above. The term $\Delta R(B)$ is a normalization factor inserted so that the value of F ranges between 0 and 1. The value of $\Delta R(B)$ was determined as follows. Traces that have been separated by $T_i = 300$ K (i.e. room temperature) are defined to be completely uncorrelated since this represents the full transition that is to be quantified. Similarly, traces separated without a trip to an intermediate temperature, such as back to back sweeps at base temperature are identical, and thus have complete correlation, so $F = 1$ for $T_i \sim 240$ mK.

$\Delta R(B)$ is calculated by taking the average value of σ for all traces separated by $T_i = 300$K. During the course of this experiment there were 6 different trips to room temperature. This gave 6 pairs of traces which were separated only by $T_i = 300$K. Because by definition a trip to 300 K produces a complete de-correlation, one trip to room temperature is as good as any other, so there were $\binom{6}{2} = 15$ values of σ that contributed to the calculation of $\Delta R(B)$ for each mode number. Calculating $\Delta R(B)$ for each set of traces (high and low mode) allows for normalization of the correlation.

Figure 4.17 shows the results of this correlation analysis. Plotted are the normalized correlation values of both low mode ($n = 2$ blue circles) and high mode ($n = 6$ red squares) traces taken on the square billiard H3 for each T_i. The probability for a charge in the dopant layer to relocate should depend on the available thermal energy by $P \sim e^{-\beta/k_B T_i}$, where β represents an energy barrier for charge relocation. However, this does not tell the whole story. This distribution should also be determined by the length of time the device was at T_i. This behavior is modeled by the expression

$F = \exp[-\eta \exp(-\beta/k_B T_i)]$ where the fitting parameter η is interpreted to represent the number of attempts of the charge to relocate. An alternative interpretation of this expression modeling F is to consider the thermal cycling to be an annealing process, in which case the parameter β could be interpreted as the activation energy, and η would represent the number of attempts (i.e. attempt frequency$\times$ time elapsed).
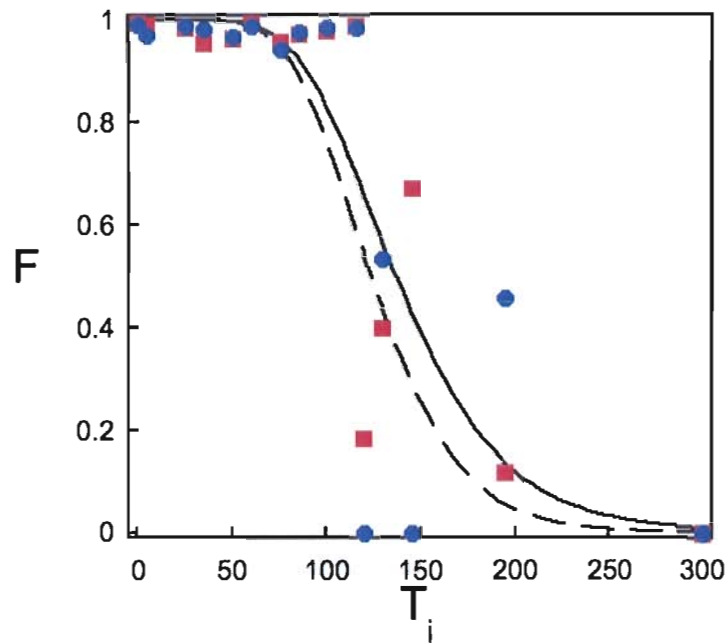
Figure 4.17.. Correlation Function F as a function of T_i

Two fits of this form are also shown in Fig. 4.17. The process to obtain the fits came in two steps. First a value for β was obtained by using a two parameter fit to the high mode data in Fig. 4.17. This two parameter fit generates the solid line in that figure, and fixes the value of β. The high mode traces were chosen for this because they tend to have a tighter spread (see Fig. 4.16). With the value of β fixed

at 42meV, the next step was to obtain a single parameter fit to the low mode data. This produced the dashed line fit, generating an η value of 25 attempts.

Figure 4.18 gives a feel for what happens as either η (a) or β (b) are allowed to vary while keeping the other parameter fixed. For convenience the value of the fixed parameter is set at $\beta = 42$ meV in (a) and $\eta = 25$ attempts in (b) the values obtained in the modeled fits to the data. In both panels the black curve represents $\beta = 42$ meV and $\eta = 25$. This is a reproduction of the dashed curve in Fig 4.17. In panel (a) of Fig. 4.18 η is increased from 10 attempts (red curve) to 100 attempts (blue curve), while β is held at 42 meV. The result is a sharper transition from $F = 1$ to $F = 0$. However, it is a decrease in the activation energy that produces a steeper falloff. In panel (b)β decreases from 56 meV (red curve) to 17 meV (blue curve) while the number of attempts is fixed at 25.

Figure 4.18. A plot of the model fit function $F = \exp[-\eta \exp(-\beta/k_B T_i)]$ as fit parameters η (a) and β(b) are varied. In (a) β is fixed at 42 meV, the values of η are: red 10, black 25, green 50 and blue 100. In (b) η is fixed at 25 attempts, the values of β are: red 56 meV, black 42meV, green 30 meV and blue 17 meV.
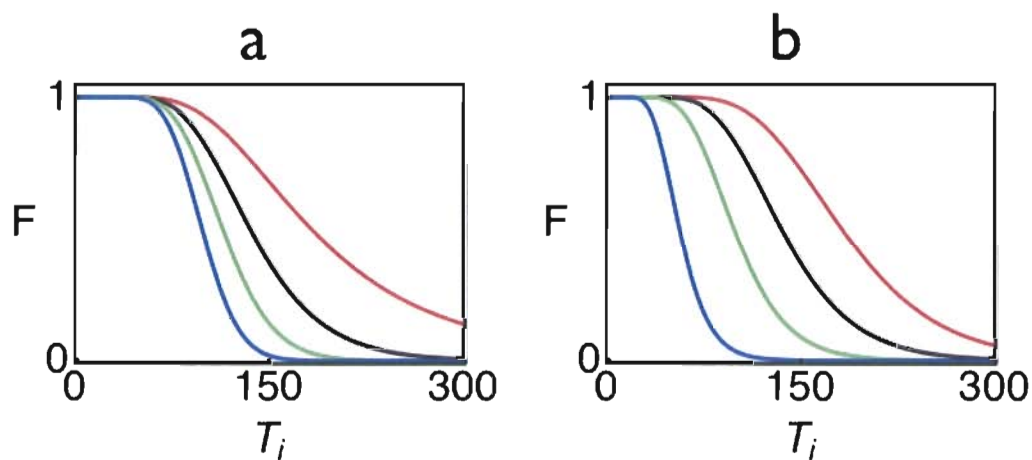
<u>Discussion</u>

This experiment shows that the de-correlation similar to that observed by bringing a billiard to room temperature can be achieved by bringing a billiard to $T_i \approx 120$ K. Normalization of correlation analysis indicates that there is a threshold energy necessary to bring on this de-correlation at about $\beta = 42$ meV. The ionization energy of Si occurs at 5.6 meV considerably lower than the 42 meV found for β. 5 meV translates to ~ 60 K and yet traces separated by as much as $T_i = 115$ K remain fairly correlated.

This indicates that simple ionization and recapture of that electron by another donor is not a strong candidate for the redistribution mechanism. However, a trapped state such as a deep DX center in the donor remains a likely candidate. Support for this claim is shown in Fig. 4.19. During a different experiment, conducted on a set of billiards etched into the same heterostructure but on a different Hall bar (sample B3b), illuminating the sample led to an enhanced electron concentration, similar to the procedure used on Wire E of Ch. III. DX centers are known to exist in AlGaAs/GaAs systems doped with Si, and persistent photoconductivity (PPC) is attributed to the DX center [60]. When the sample is exposed to light, the DX centers become ionized, and the carrier concentration increases. It is persistent in that the electrons remain in the conduction band even after the light is turned off, until eventually they are recaptured by the DX center which can take as long as days depending on material properties [60]. The increased electron concentration shown

in Fig. 4.19 had a much shorter lifespan, but did last for about 12 hours. Our etched structure has not been studied to exhibit DX centers. A literature on the subject revealed no results. However there were no results discounting the possibility either.
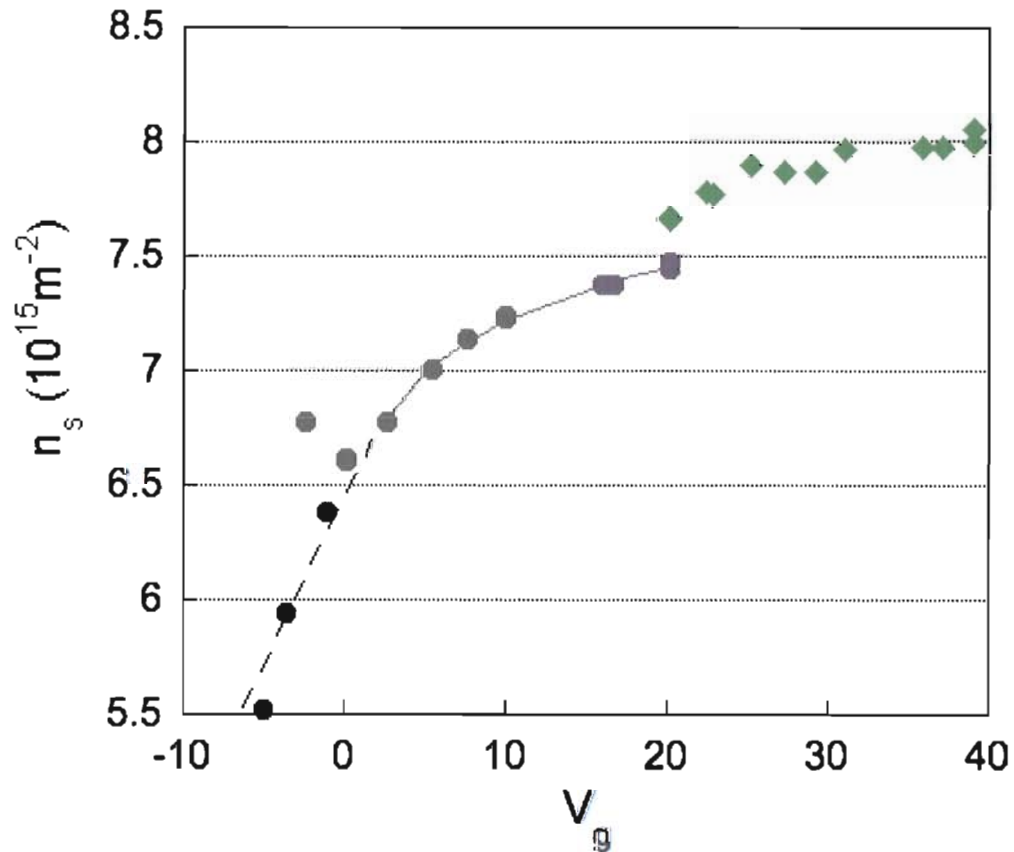
Figure 4.19. Electron density (n_s) *vs* gate voltage (V_g) before (grey) and after (green) illumination of sample B3b. The dashed line is a guide to the eye. The solid line is a power law fit to the pre-illumination data in the saturated regime of n_s. Green data points indicate the rise in n_s after illumination.

The plot of electron density vs. gate voltage in Fig 4.19 shows a marked increase in electron density before (grey) and after illumination (green). The dashed line is a

guide to the eye, illustrating the linear nature of n_s for negative gate voltages. The solid line is a powerlaw fit to the saturated portion of n_s which is not uncommon for positive gate voltages [63]. This saturation is most likely due to an inter-surface state [19, 21].

Figure 4.20 is a plot of the gate sweeps ($G\,vs.\,V_g$) conducted before and after the illumination of sample B3b. There are a total of four data sets in this figure, G is plotted against V_g for two billiards before (grey) and after (green) illumination. The upper trace, with data beginning to be displayed at $V_g = 0V$, is measured for billiard 2L, while the other data set (beginning at $V_g = 5$ V) was measured on billiard 3L. Both devices show a rise in $< G >$ after illumination, which is as expected since the measurement for n_s is conducted on the Hall bar itself, not a specific billiard. However, at $V_g = 20V$, the upper trace (larger $< G >$ for all V_g) shows that both the green and grey traces lie on the same plateau of $< G > \sim 2.5$ ($2e^2/h$). Thus another way to interpret the effect of the increase in n_s is that the QPCs in the billiard are able to accommodate additional modes (i.e. reach a new plateau) at a smaller V_g.

MCF traces taken before and after illumination still may show differences in their fine scale features, because the increase in n_s is directly proportional to an increase in E_F. Such a small shift in E_F is not expected to alter the location of the diffusers. However it may alter the electrons path with respect to the diffusers [58]. Consider, for example, an electron traveling straight towards a diffuser, perhaps a 'hill' in the potential. Suppose that while the billiard is at some Fermi energy E_F^A the path
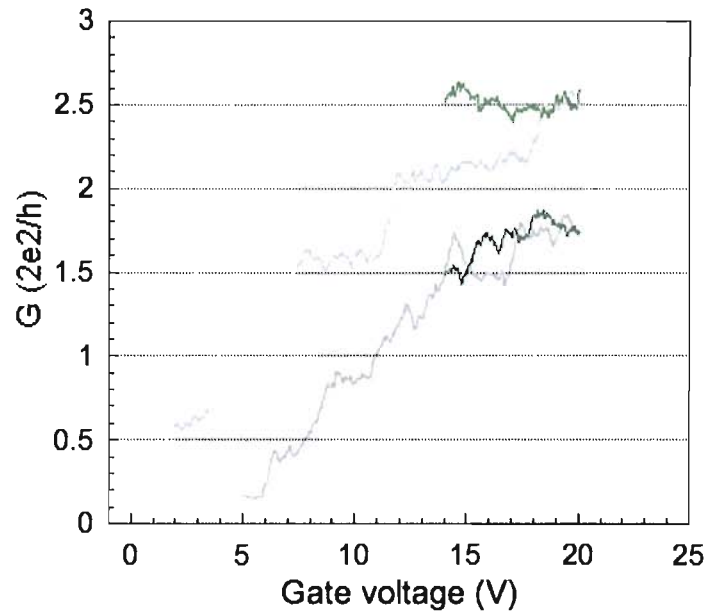
Figure 4.20. G vs. V_g for before(grey) and after (green) illumination for two billiards on the Hall bar called B3b. billiards 2L (upper trace) and 3L (lower trace)

tends to veer through a small angle that takes the electron to the left of the 'hill'. Altering the Fermi energy to say E_F^B could result in the trend of the path to produce a small angle veer to the right [58]. Such a difference in paths will slightly alter the accumulation of phase in the same manner as the redistribution of the diffusers, particularly after repeated reflection off of billiard walls. Field sweeps (MCF traces) were taken after each of the gate sweeps in Fig. 4.20 and are plotted together in Fig. 4.21. The blue trace is the field sweep taken prior to illumination. The green trace, which has been vertically offset for clarity, was taken after illumination.

Indeed, there are differences in the fine scale features of the MCF of Fig 4.21. In fact, by visual comparison, those differences seem to be on par with the differences in
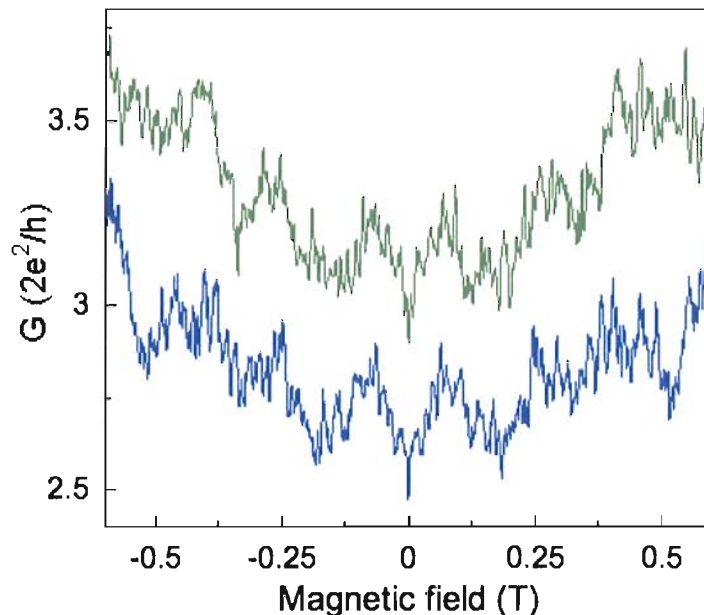
Figure 4.21. Magnetic field sweeps of billiard B3b2L taken before and after illumination

the traces that have been temperature cycled to $T_i = 300K$. Correlation analysis was performed resulting in $\sigma = 150\ \Omega$. Normalization of this was not possible since we have only one data point, in which the billiard sat at the same conductance plateau at the same gate voltage before and after illumination. However, comparison with the values of σ for the $T_i = 300K$ traces, places this value just above the least correlated high mode ($\sigma = 144\ \Omega$) and well below the most correlated low mode trace ($\sigma = 357\ \Omega$). Since this is a high mode trace, this seems to imply that the effect of illumination produced trajectory changes that were on par with those arising from warming the sample to room temperature and re-distributing the scattering configuration in the billiard. Unfortunately, this is the only data point for this measurement, so making

any stronger claims is unjustified. However, coupling this strong de-correlation with the existence of PPC does seem to indicate that a trapped state is a likely candidate for the mechanism leading to relocation of the ionized donors. A schematic rendition of a band diagram including this trapped state is shown in Fig. 4.22. Energy is plotted against the heterostructure depth, and the trapped state is shown schematically as a square well in the Si doping layer as this trapped state seems to have some of the characteristics of a DX center, which are known to reside in the Si atoms in Si doped III-V semiconductors [60]. A more realistic, yet still primitive model of the potential near a donor containing trap is also illustrated to the right of the true quantum well that forms the 2DEG (indicated by the green arrow), which is modeled after a DX center [19, 60, 62].

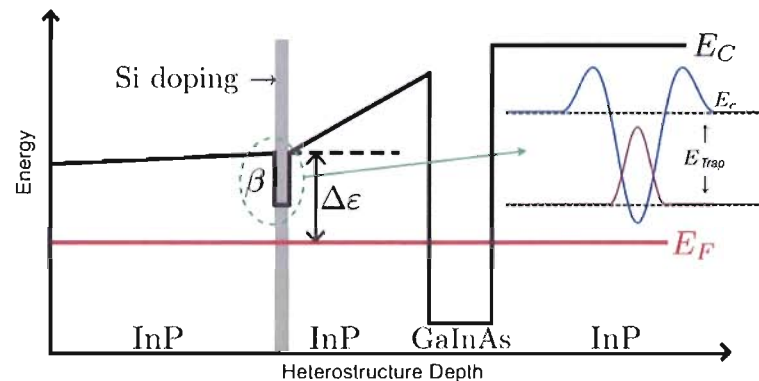**Figure 4.22.** Schematic band diagram for the possible trapped state. The circled region represents the location of the trapped state while the arrow points to a crude representation of the potential surrounding the donor with the trapped state.

This trap requires more than one energy to be characterized, consistent with persistent photoconductivity (PPC). The blue barriers that rise above the conduction

band indicate that there is some energy requirement to occupy the trap. There is also some energy requirement to escape, indicated by the separation of the peak of the purple curve and the conduction band E_c. Illumination can accomplish the release of an electron into the conduction band. Finally, there is some energy E_{trap}, that in the case of the DX center, determines the occupation when the DX centers are in thermal equilibrium with the rest of the lattice. The presence of PPC at low temperature indicates that the DX center is not in thermal equilibrium at low temperatures, thus the occupation levels are 'frozen' in [19, 60].

Conclusion

This chapter began by revisiting the infinite horizon billiards introduced in Ch. I. The discussion of the infinite horizon billiards reported on findings that a small shift in the location of the Sinai diffusers led to the same enhanced diffusion present in the well ordered array. The role of the walls in semiconductor billiards is to perpetuate the array of the material impurities (i.e. the ionized donors). These play the role of the Sinai diffusers by producing a roughened potential terrain. Reflection off of the billiard walls serves to amplify this classically chaotic effect through the process of iteration. The role of the billiard walls was further extended by demonstration that the walls dictate the form of the overall background trend of the magneto conductance fluctuations.

The experiment described in this chapter demonstrates such a mildly disordered Sinai billiard can be produced by alteration of the charged state of the dopant layer in the heterostructure. To achieve this alteration, the dopants themselves need not change their location, just their charge. The activation energy necessary to produce this alteration was found to be on the order of 40 meV by thermally cycling the billiard to various intermediate temperatures and quantifying the amount of de-correlation in the magnetic field sweeps conducted after each T_i. This activation energy of the annealing process is much lower than the energy necessary for the dopants to diffuse throughout their layer. Diffusion of Si dopants has ben reported to occur at temperatures of $\sim 500\,^\circ$ C in GaAs δ doped with Si [64], and much higher temperatures in modulation doped AlGaAs/GaAs [65]. This indicates that the relocation of the dopants themselves should be ruled out entirely.

However, strong candidates for the re-distribution process remain, 42 meV is more than sufficient energy to ionize the Si. So ionization and recapture is a possibility. Recapture seems an important feature of this particular mechanism because the statistical properties of the MCF, as measured by D_F, were shown to remain unchanged after several cycles to room temperature.

The other candidate for this mechanism of the Sinai diffuser re-distribution is a trapped state, with a binding energy on the order of $\sim$ 40 to 50 mK. Support of this trapped state was provided in the form of persistent photoconductance, a hallmark of the DX center known to be a resonant state of Si donors [60]. After photo

illumination, the one pair of MCF traces was shown to be as fully de-correlated as the high mode pairs (T_i= 300K). Ultimately this chapter has provided strong evidence that the previously considered "clean" billiard defined by etching a modulation doped heterostructure is not so clean, as material induced impurities still play a vital role in the electron dynamics.

CHAPTER V

THE SENSITIVITY OF D_F TO EXTERNAL FIELDS

Introduction

The previous chapters have shown that the underlying cause of fractal conductance

fluctuations (FCF) was material impurities playing the role of Sinai diffusers. This

was shown to be 'universal' in the sense that the same process dictated the dynamics

across the diffusive, quasi ballistic and ballistic regimes. Whether the Sinai diffusers

were in the plane of conduction as in the diffusive wires, or were remote and acted as

small angle scatterers, the process was the same. Furthermore, the fractal dimension

could be charted in the same manner across all three regimes. The form of $Q = \dfrac{\Delta E_S}{\Delta E_B}$

leads to the prediction that if the billiard size were reduced to ~ 50 nm than values of

$Q = 1$ could be observed at room temperature.[1] Together with the FCF's remarkable

insensitivity to device boundaries, shape, or level of material induced disorder seems

to indicate that they will be prevalent whenever resolution of the energy states is

possible. It is not the presence of FCF that is sensitive to these parameters, but

rather their fractal dimension. This leads to two obvious roles for the FCF. Either

the FCF will be unwanted, and be viewed as noise, or on the other hand, they could

---

[1]This calculation is based on parameters of bismuth nanoclusters that are the subject of current research with collaborators in Australia and New Zealand

be harnessed as some sort of novel sensor. Either way, the characterization of the sensitivity to external electric and magnetic fields will be important.

With the aim of characterization of this sensitivity, this chapter will also explore using a different means to alter the accumulation of phase leading to FCF. Application of an electrostatic field will change the energy at which the electrons traverse the billiard and this will give rise to alterations in phase [66]. This chapter begins with the investigation of this process.

Producing FCF with an Electric Field

Figure 5.1 shows the conductance G as a function of voltage applied to the Ti/Ag top gate, which has been electronically isolated from the device via a 1μm layer of hard baked Shipley 1813 insulating polymer. The measurement was taken on the square billiard of the sample called H1. Traces were taken at base temperature of our ^{3}He cryostat ($\sim$ 240 mK, blue line). An additional trace is shown taken at 5K (red line) to establish the plateau background, indicating the number of modes in the QPC. Arrows indicate the plateaus at which the gate was held during magnetic field sweeps for $B_1, V_g = $ -9.2V, $V_g = $ -5 V for B_2 and -1.2 V for B_3. This experiment involved taking a high resolution gate sweep at base temperature and using this data to investigate the production of fractal conduction fluctuations induced by an electric field.

Typical gatesweeps are conducted at a resolution of $\sim$ 10mV. To enable fractal

analysis, the resolution of the base temperature gate sweep was increased ten fold to 1 mV. The black trace (offset) at the top off the figure is the result of subtracting the 5K (red) trace from the base (blue) trace, removing the plateau background. The arrows indicate the plateaus at which magnetic field sweeps were conducted.
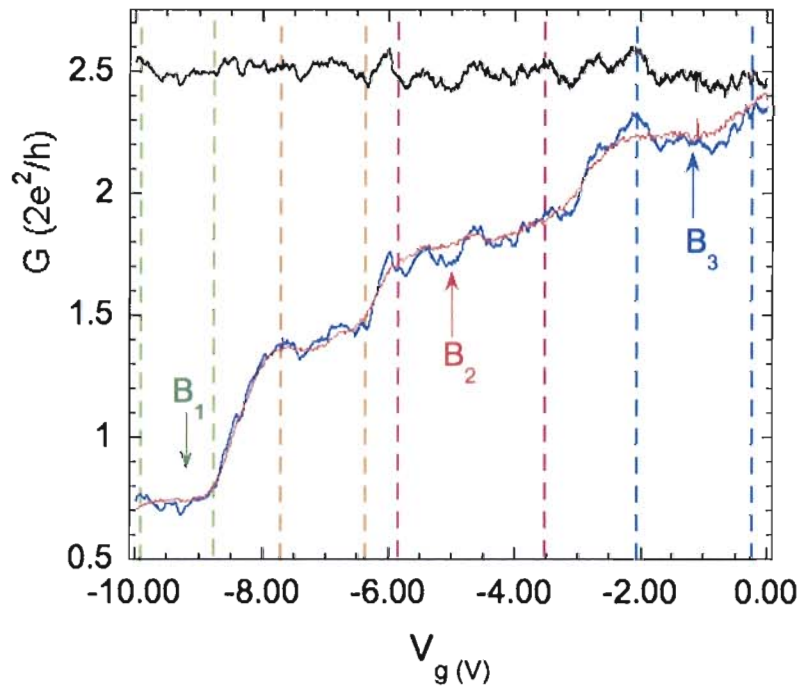
Figure 5.1. Conductance *vs.* applied gate voltage for the device called H1 taken at base temperature (blue), 5K (red). The difference between the two traces is vertically offset and shown in black. Arrows indicate gate volyages at which magnetic field sweeps were conducted. Dashed lines represent subregions of the plateaus.

When offset as in Fig. 5.1, the fluctuations in the background-subtracted gate sweep (black trace) appear small enough that one may interpret them as noise. However, this is not the case, as is evidenced in Fig. 5.2 where the background-subtracted gate sweep is plotted in blue along with a noise reference plot in red.

The noise plot was obtained by running a magnetic field sweep with the magnet turned off, (hence the label of the top axis). Data was recorded without sweeping the magnet but with current running through a billiard. The mean value of the conductance in the noise sweep was then subtracted off to allow a measurement of the noise scattered about $G = 0$ $(2e^2/h)$. The background-subtracted gate sweep has fluctuations considerably larger than those of the background-subtracted noise sweep, indicating that the gate sweep fluctuations are not noise.

Figure 5.2. Background-subtracted conductance fluctuations (blue) are much larger than the noise level of the measurement (red)
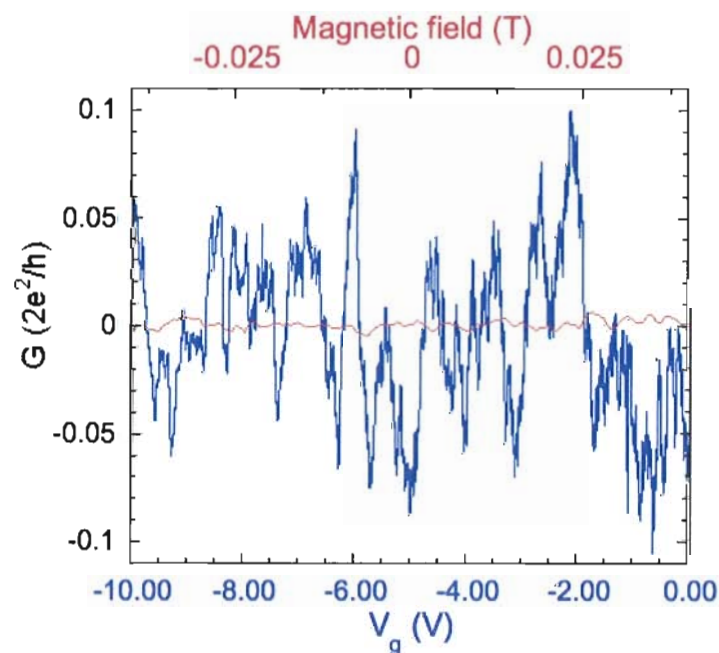
Figure 5.3 left shows the magnetoconductance fluctuations (MCF) resulting from sweeping the magnetic field while the gate voltage was held at (bottom to top) B_1 = -9.2V (green), B_2 = -5V (red) and B_3 = -1.2V (blue). In the right panel is the

scaling plots for the associated traces. The slope of these lines designates the fractal dimension (D_F) of each trace. As more modes are introduced by increasing the gate voltage, the D_F value gradually decreases from a value of $D_F=1.45$ for the low mode B_1 to 1.42 for B_2 and finally 1.38 for B_3.
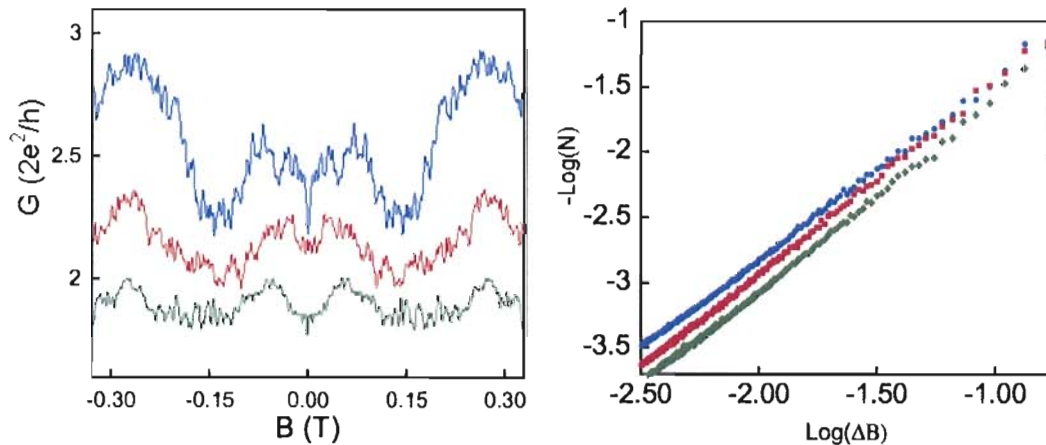
Figure 5.3. MCF and (color matched) scaling plots of the magnetic field sweeps indicated by the (color matched) arrows in Fig. 5.1

The reason for the vertical dashed lines delineating each plateau in Fig. 5.1 is illustrated by Fig. 5.4. Presumably, one could imagine that the fractal dimension of the background-subtracted gate sweep shown in blue in Fig. 5.2 should be bounded by the values obtained from the MCF taken at plateaus at both ends of the gate sweep. While this is the case, it turns out not to tell the whole story. This is evidenced by the red line in Fig. 5.4. The data points in that figure are the results of the variational method box count, the red line illustrates a line with a slope 1.4, which is bounded by the MCF D_F values. However, the main reason for this line is not to illustrate the bounding but to emphasize the curvature of the scaling plot data. While a very short

region of that data could be fit to a straight line, the true nature of the fit would be convex. This illustrates the need to individually consider the subregions defined by the plateaus.
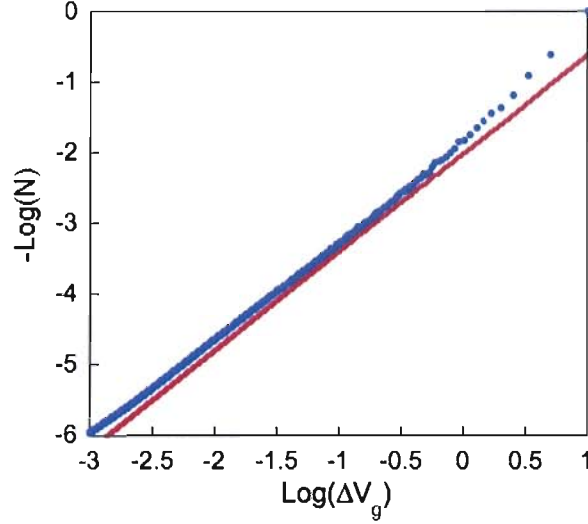
Figure 5.4. Scaling plot of the background subtracted gate sweep. The red line is a straight line with a slope of 1.4 for comparison.

This raises the interesting question of why should it be necessary to divide the background-subtracted gate sweep into sub-regions? Whenever an MCF sweep is conducted, general practice is to run a few gate sweeps to ensure that the magnetic field sweep will be conducted on a plateau. This ensures a consistent Fermi energy during the sweep, i.e. not on a transition to a new plateau. Equation II.11 gives:

$$r_{cyc} = \frac{m^* v_F}{e\, B_{cyc}} = \frac{v_F}{\omega_{cyc}} \tag{V.1}$$

Where $\omega_{cyc} = \dfrac{e\, B_{cyc}}{m^*}$ defines the cyclotron frequency at which the electrons travel

in a circular orbit under the influence of a perpendicular magnetic field B_{cyc}. Quantization of energy of the electrons in the 2DEG yields the Landau levels [18, 46] with energy given by:

$$E_n + \left(n + \frac{1}{2}\right) \hbar \omega_{cyc} \qquad (\text{V}.2)$$

For small magnetic fields, in which the cyclotron radius is much larger than the billiard dimensions (i.e. $2r_{cyc} \gg W$ for a square billiard of side lengths W) the effects of confinement by B are negligible [46]. It is the electrostatic confinement that contributes to quantization of the energy levels. $B \sim B_{cyc}$ sets the threshold of the magnetic field's onset to contribution to the confinement.[46] However, MCF are only analyzed for their fractal content up to B_{cyc}. Thus the magnetic field's contribution to the MCF is providing a curvature of the trajectories, not a confinement. Staying at a fixed gate voltage, on conductance plateau ensures that the MCF are a measurement of the magnetic fields influence of the electron trajectories at a particular E_F.

This is not the case when the gate voltage is used to induce the conductance fluctuations. Application of voltage to the top gate allows tuning of the Fermi energy (E_F) and therby the Fermi wavelength(λ_F) in the billiard as well as the number of conducting modes(n) in the quantum point contacts, as illustrated by the conductance plateaus in Fig. 5.1. It is the changing of λ_F that offers the most intuitive explanation to the observed conductance fluctuations. Changing λ_F necessarily changes the ratio

of wavelengths to path length, which can also be considered as phase difference. These phase differences will of course lead to a change in interference.

This is a plausible explanation for the presence of the conductance fluctuations with applied gate voltage. It also indicates the need to isolate the individual conductance plateaus and treat them independently. Over a particular plateau, a slight change in E_F will still occur, but this will not be accompanied by an increase in conducting modes. The sub-regioning of the high resolution gate sweep was carried out, and the resulting D_F values are listed in Table 5.1 along side the D_F values obtained from the MCF.

V_g (V)	D_F MCF	D_F subregion
-9.2	1.45	1.23
-7	–	1.33
-5	1.42	1.34
-1.2	1.38	1.40

Table 5.1. D_F for the magnetic field sweeps indicated by the arrows in Fig. 5.1 and the background-subtracted subregions indicated by the dashed lines of the same figure.

The high resolution gate sweep represents the conductance fluctuations in a particular billiard as a function of voltage applied to the top gate of that billiard. To obtain a larger range of FCF produced in this manner, conductance fluctuations were simulated by a process known as fractional Brownian Motion (fBM) which is known to produce fractals [4, 26], and has previously been used to model conductance fluctuations [12]. With D_F is an input parameter in the simulation, using the fBm simulations adds the

advantage of being able to investigate the properties of a trace with a specific D_F. Because simulated fBm traces are going to be used in comparison, it would be useful to have the fluctuations in G as a function of the electrostatic potential changes in the device. Having G as a function of the potential will offer a wider scope of the analysis. To obtain the potential changes, it is assumed that alterations in E_F from the $V_g = 0$ value are due to changes in the potential according to $\Delta E_F = e\Delta V$. This then requires obtaining E_F, or more precisely $\dfrac{\partial E_F}{\partial V}$, which can be obtained from the electron density n_s.

The electron density in the billiard is plotted against gate voltage in Fig. 5.5. Because this measurement was obtained for values of $V_g < 0$, n_s is far from the saturated regime, and scales linearly with V_g. Thus $\dfrac{\partial E_F}{\partial V}$ is approximated by the slope of the linear fit to the n_s $vs.$ V_g data shown as the dashed line in Fig. 5.5.
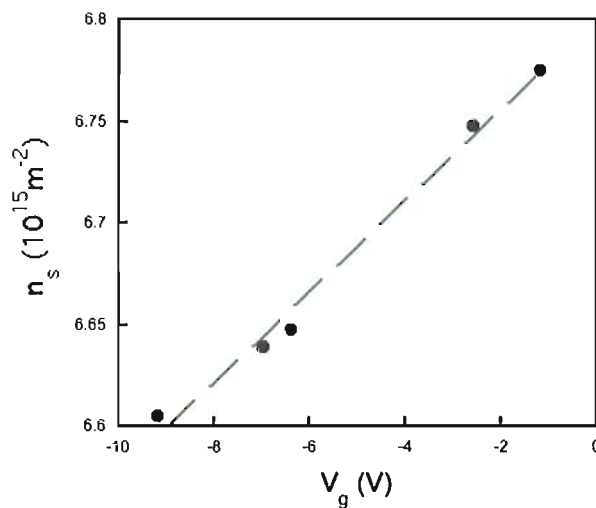
Figure 5.5. Electron density (n_s) plotted against applied gate voltage (V_g) in the square billiard of H1.

When electrons are confined to two dimensions, E_F scales linearly with n_s. Because E_F scales linearly with n_s and n_s scales linearly with V_g, E_F must also scale linearly with V_g. Fig. 5.6 illustrates that this is the case and E_F is plotted in blue (according to the left hand axis) against V_g. In this figure, λ_F is also plotted against V_g to emphasize that λ_F remains considerably smaller than the billiard dimensions.

Figure 5.6. Fermi Energy (blue, left axis) and Fermi wavelength (red, right axis) plotted against applied gate voltage

It is a safe assumption that the change in V_g results in a change in the potential that also scales linearly. However, to verify this, values of the potential responsible for changing E_F from the $V_g = 0$ according to $\Delta E_F = eV$ value have been plotted in Fig. 5.7.
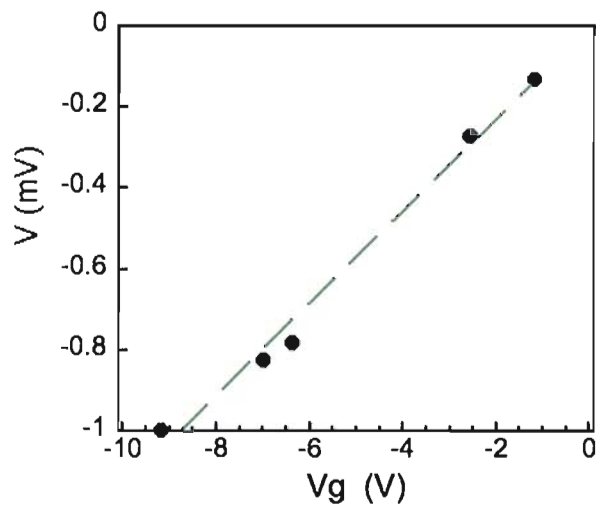
Figure 5.7. Estimation of the electrostatic potential energy as a function of applied gate voltage.
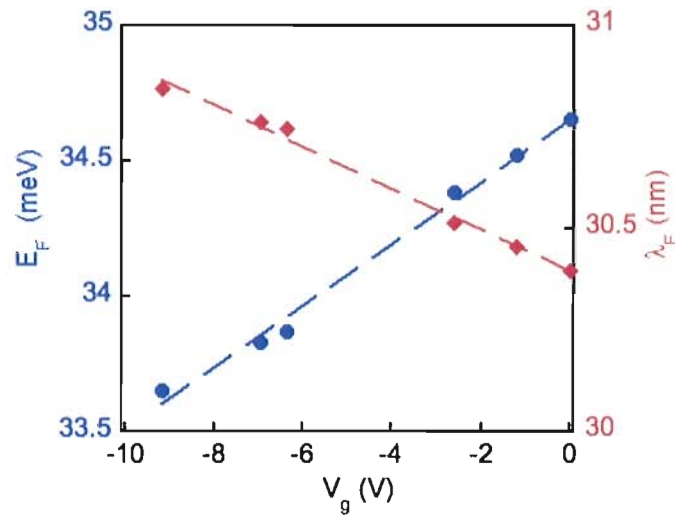
Figure 5.8 shows the gate sweep scaled in this manner emphasizing that the change of scale does not alter the structure of the data set. The blue trace corresponds to the bottom axis and is the original background subtracted gate sweep. The red trace is the same data set scaled to be plotted as a function of electrostatic potential rather than gate voltage. This allows the freedom to compare the gate sweep with spectrally simulated fBm traces on equal footing, that is to say the comparison is not limited to units that are device dependent.

Noting that the full gate sweep was a trace in which the D_F value changed throughout the sweep, this was imitated with the fBm generated traces. Figure 5.9 shows the results of this simulation. The top (blue) trace is the high resolution gate sweep. The traces below that each consist of three fBm traces that have
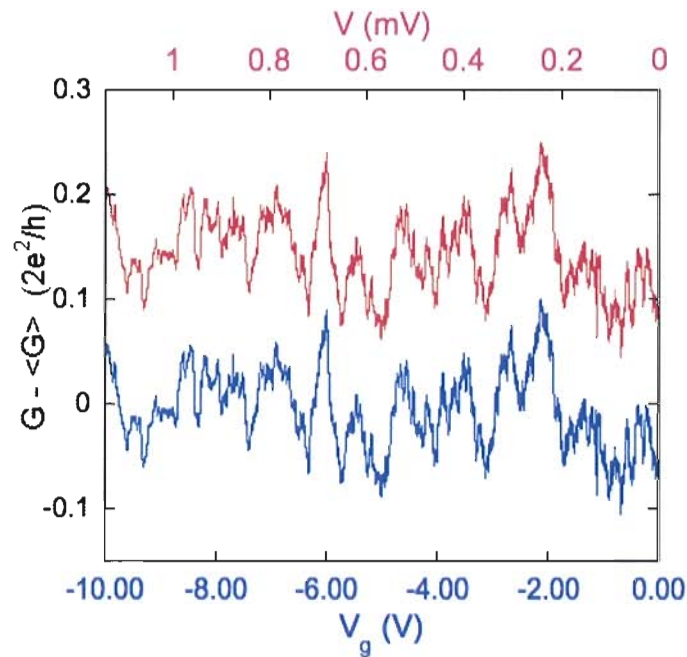
Figure 5.8. Conductance in the square billiard as a function of gate voltage(blue, bottom axis) and electrostatic potential (red, top axis).

been appended to one another in an attempt to mimic the increasing density of the fluctuations as the applied voltage increases from negative voltages toward $V_g = 0$. The middle (green) trace represents fBm simulations with input D_F values of (left to right)1.3, 1.4, and 1.5. The vertical dashed lines in that figure mark the transitions between the three fBm simulations that constitute the full trace. The bottom (red) trace is an extreme example of this combination procedure. In that trace, D_F values increase quickly from 1.1 in on the left to 1.5 to 1.9 for the last third of the trace.

A fractal analysis was conducted using the variational method box counting technique. In Fig. 5.10 color matched scaling plots have been shifted for clarity and ordered to match the inset. Note that each of these scaling plots has a slight upward bend. Thus
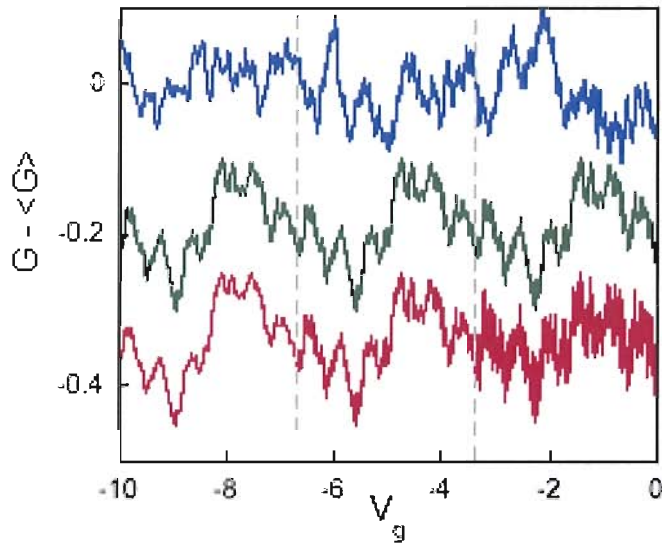
Figure 5.9. Background subtracted gatesweep and simulated fBm. Top (blue) trace is the high resolution gate sweep with the plateau background and $< G >$ subtracted. Also shown are simulated FBM traces. These traces are combinations of $D_F = 1.3, 1.4$, and 1.5 (green) and $D_F = 1.1, 1.5, 1.9$ (red).

an effective fractal dimension (D_e) is estimated based on the best fit to a reasonably long (i.e. >1 order of magnitude) portion of the associated scaling plot. Effective dimensions were estimated to be $D_e = 1.41$ for the (blue) high resolution gate sweep, 1.39 for the simulated fBm trace composed of slowly increasing values of D_F (green trace) and 1.49 for the red trace in which the D_F value rise sharply.
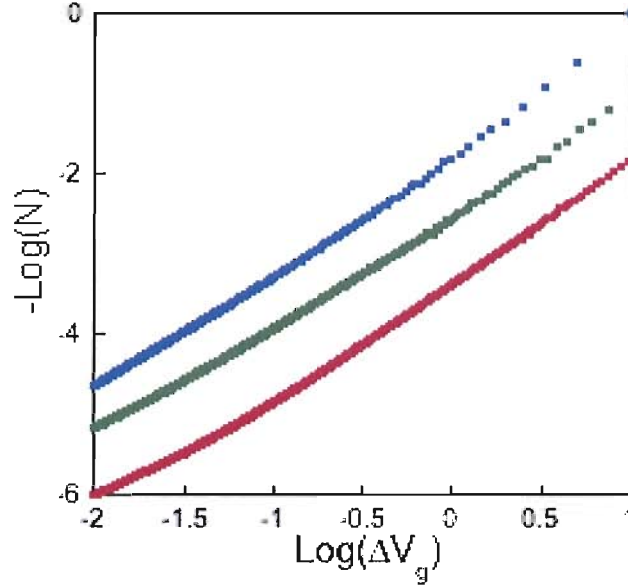
Figure 5.10. Scaling plots of the gatesweep to simulated fBm. Scaling plots are shown for the traces shown in Fig. 5.9(same colors). Note that the slope of the data trace closely matches that of the FBM trace consisting of slowly varying D_F values.

Autocorrelation Analysis

The curvature of the scaling plot suggests that using a probe other than D_F is in order. Noting that the correlation function used in the thermal cycling experiment (Eq. IV.1) was more sensitive to fine scale differences traces than D_F, a similar process was used to obtain a measure of how well an individual trace remains correlated with itself. As such, an autocorrelation function analysis was used to monitor the effects of an applied field to the conductance fluctuations.

$$\mathcal{F} = \frac{\langle G(\Phi)G(\Phi + \Delta\Phi)\rangle}{\langle (G(\Phi))^2 \rangle} \tag{V.3}$$

Here Φ represents either the applied magnetic or electric field. This is not a drastic departure from the fractal analysis that has been used thus far in this dissertation. In fact, Eq. V.3 is the Fourier transform of the power spectrum [26]. However, because Matlab is well equipped to handle matrix manipulation, it proved more practical to develop a program that would carry out the process of Eq. V.3. Figure 5.11 shows the results of this analysis on the three magnetic field runs depicted in Fig. 5.3 (left panel), as well as the three dashed regions of the gate sweep (right panel) of Fig. 5.9. The choice of using the three dashed regions represents a compromise between allowing the applied potential to vary slowly and at the same time allowing for sufficient data resolution for statistical analysis. Prior to autocorrelation analysis the gate sweep was scaled by $\partial V / \partial V_g$. This allows the autocorrelation analysis to be interpreted as the de-correlation of the trace as a function of applied field. The magnitude of the applied potential at each subregion is ranked low to high on the plots for distinction. To characterize the how quickly a trace de-correlates, the range of Φ is chosen to illustrate when $\mathcal{F}(\Phi)$ falls to half of its value of 1 at $\mathcal{F}(0)$.

The plots in Fig. 5.11 indicate the fractal conductance fluctuations sensitivity to the applied fields. When the applied field is strictly an electric field, $\mathcal{F}$ falls of more quickly as the magnitude of the field is increased. When exposed to both a magnetic and electric field, the rate at which $\mathcal{F}$ falls off is governed by the D_F value. The same cannot be said for the electric field induced conductance fluctuations because as yet the D_F values obtained are in question. To solve this problem, the individual
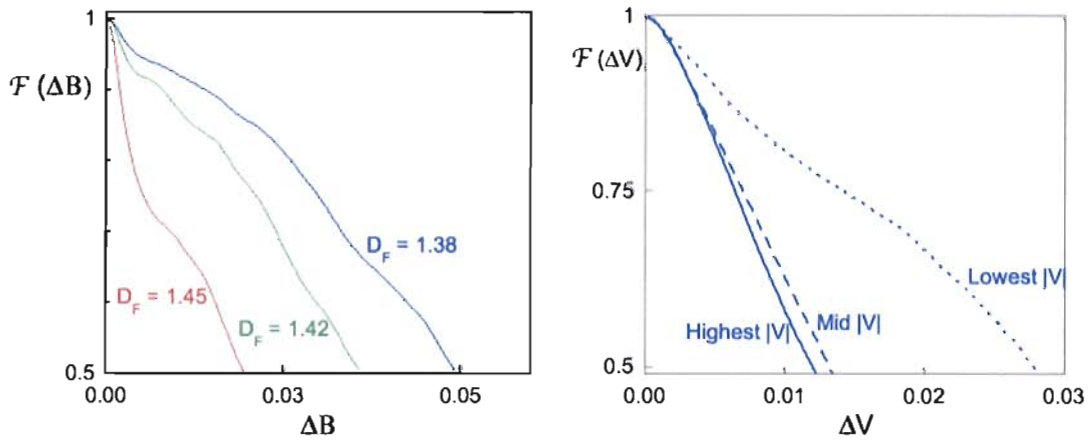
Figure 5.11. Autorrelation Function $\mathcal{F}$ falloff as a function of ΔB for the three MCF traces in Fig. 5.3 and $|\Delta V|$ for the three dashed regions of Fig. 5.9.

fBm traces will be used. But before that can be done, a relationship between the autocorrelation falloff and D_F should be understood.

The relation between the autocorrelation falloff and D_F, first consider a continuous bounded temporal function $f(t)$ which has a box counting dimension s. Reference [26] relates the autocorrelation function $(C(h))$ to the box counting dimension s as:

$$C(0) - C(h) \simeq ch^{4-2s} \tag{V.4}$$

Where c is a constant, and h is used to represent separations in time. Translating Eq. V.4 to the autocorrelation function $\mathcal{F}$ as a function of applied field (as opposed to time) and replacing s with D_F for consistency with the previous nomenclature gives:

$$\mathcal{F}(0) - \mathcal{F}(\Delta\Phi) \simeq k\Delta\Phi^{4-2D_F} \tag{V.5}$$

Where the constant c has now been replaced by k for clarity. Defining the value of Φ_c to be the $\Delta\Phi$ value at which the autocorrelation function falls to half of its value of $\Delta\Phi = 0$ gives:

$$\mathcal{F}(0) - \mathcal{F}(\Phi_c) = \frac{1}{2} \simeq k\Phi_c^{4-2D_F} = k\Phi_{1/2}^{\tilde{D}} \qquad (V.6)$$

Where, for convenience, $\tilde{D}$ has been defined as

$$\tilde{D} \equiv 4 - 2D_F \qquad (V.7)$$

This gives:

$$\frac{1}{2} \simeq k\Phi_c^{\tilde{D}} \Rightarrow \Phi_c^{\tilde{D}} \simeq \frac{1}{2k} = (2k)^{-1} \qquad (V.8)$$

Taking the logarithm of both sides of the above equation, and noting that if k is a constant then $\ln(2k)$ must be as well allows:

$$\ln\left(\Phi_c^{\tilde{D}}\right) \simeq \ln\left((2k)^{-1}\right) \qquad (V.9)$$

$$\tilde{D}\ln\left(\Phi_c\right) \simeq -\ln\left(2k\right) \qquad (V.10)$$

$$\tilde{D}\ln\left(\Phi_c\right) \simeq -\tilde{k} \qquad (V.11)$$

Where in the last step the constant $\tilde{k}$ was substituted for the constant $\ln(2k)$. Φ_c is the width of the increment in applied field corresponding to the half-max falloff of the autocorrelation function $\mathcal{F}$. Exponentiating both sides of Eq. V.9 allows the relation

of Φ_c to D_F of the associated conductance trace according to:

$$\Phi_c \simeq e^{-\tilde{k}/\tilde{D}} = exp\left[\frac{-\tilde{k}}{4-2D_F}\right] \equiv \mathcal{F}_{1/2} \qquad (V.12)$$

Where in the last step the half width falloff of $\mathcal{F}$ has been renamed to the more intuitive $\mathcal{F}_{1/2}$. This gives the expected form of the falloff to half max value of the autocorrelation function $\mathcal{F}_{1/2}$ as a function of D_F. The simulation of the fBm traces allows for assigning D_F as an input. However, this value is not always the true fractal dimension of the associated simulation. For this reason a variational box count was conducted on each of the simulated fBm traces used for this analysis. An autocorrelation analysis was performed on each of the fBm traces and their $\mathcal{F}_{1/2}$ values are plotted against D_F in Fig. 5.12. The intended D_F values (i.e. those fed into the fBm simulations) are represented by hollow circles and the dashed line is a fit to that data using Eq. V.12. The D_F values obtained by box count of the fBm traces are indicated by solid circles.

The intended D_F values fit the form of Eq. V.12 well, while the verified (by box count) values show significant deviation from the fit. However, the overall trend is in agreement, which is promising. To obtain a better fit to the verified D_F values, the fact that Eq. V.12 is not a strict equality is exploited. The relaxation of equality implies that the use of a pre-exponetial constant other than unity and an additive constant are acceptable. The addition these fitting parameters results in the dashed fit line to the verified D_F values plotted in Fig. 5.13. Also shown in that plot are the $\mathcal{F}_{1/2}$ values obtained for the magnetic field sweeps (in blue) which correspond to the
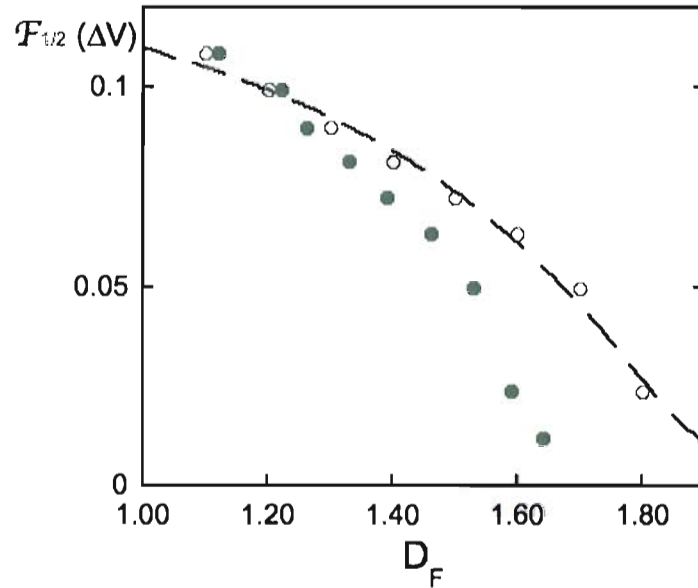
Figure 5.12. Autorrelation Function $\mathcal{F}$ as a function of intended (hollow circles) and verified (solid circles) D_F for the simulated fBm traces.

left hand axis. For comparison, the D_e (red) values obtained are used to plot $\mathcal{F}_{1/2}$ for as a function of dimension. Both the D_e values and the verified D_F values for the simulated fBm traces are associated with the right hand axis.

Figure 5.13 indicates that the fractal conductance fluctuations are quite sensitive to external fields, both magnetic and electric. Sensitivity increases with the fractal dimension of the FCF in the sense that the field will induce a more dramatic de-correlation.
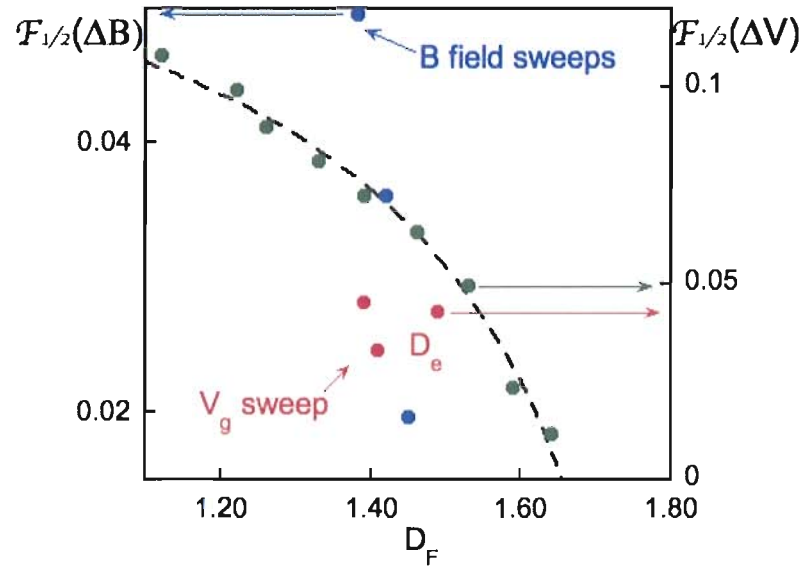
Figure 5.13. Autorrelation Function $\mathcal{F}$ falloff as a function of D_F in magnetic and electric field traces. The MCF (blue circles) and the simulated fBm traces (green circles) with D_F determined by a box count. Also shown (in red) is $\mathcal{F}$ as a function of the effective dimension D_e of the three traces in Fig. 5.9

<u>Application of a Bias Voltage</u>

Any reasonable application of a device will most likely include exposure to higher fields than have been investigated thus far. Whether the application is to be used for a process in which the FCF are viewed as unwanted, contributing to the noise, or the FCF are to be employed as a novel sensor, the device will most likely have a bias voltage defining the current direction applied to it. The effect of an applied bias will surely alter the potential in the billiard. However this is not expected to alter the existence of FCF. Indeed it has been shown previously in this dissertation that the presence of FCF is not suppressed by alterations in the potential. However, the application of a bias voltage could also induce an increase in phase breaking

interactions. Such interactions will reduce the phase breaking time, τ_ϕ. Reduction of τ_ϕ will alter the statistical properties of the FCF (i.e. α). In addition, an applied bias voltage could also lead to heating, which can also reduce τ_ϕ . Indeed both τ_ϕ and T appear in Q and thus may alter the performance of such a sensor, or influence the FCF's contribution to any noise. This section will investigate the results of exposing the billiard to higher voltages. Since Q will be used throughout this discussion, the FCF will again be characterized by α rather than D_F. However the two are related through Eq. II.8, $\alpha = 5 - 2D_F$.

All previous electronic measurements have been made in the constant current configuration as illustrated schematically in Fig. 2.12. The measurements discussed below are conducted with a voltage adder/divider configuration in which the voltage drop across the sample consists of an AC voltage with a DC bias. This measurement set-up is illustrated in Fig. 5.14. The main deviation from Fig. 2.12, is the adder/divider box used to couple the DC bias voltage to the AC signal. One port of the IOTECH DAC was used to piggy-back a small DC bias voltage (V_{DC}) to the 37 Hz AC signal (V_{AC}) used for Lock In measurements. The mixture of bias and signal was obtained using a voltage adder/divider circuit built in our lab for similar measurements. The adder/dividers was designed so that the output was given as $V_{out} = \dfrac{V_{AC}}{33,333} + \dfrac{V_{DC}}{1000}$. Using a 0.1V AC signal from the 'sine out' port of a lock-in amplifier then results in a reduced AC signal of 30 μV. Similarly, the applied DC voltage from 0 to 10 V was also reduced to range from 0 to 10mV. Four terminal measurements were conducted

across each of the billiards, and current was monitored by measuring the voltage drop across a known $(1K\Omega)$ resistor.
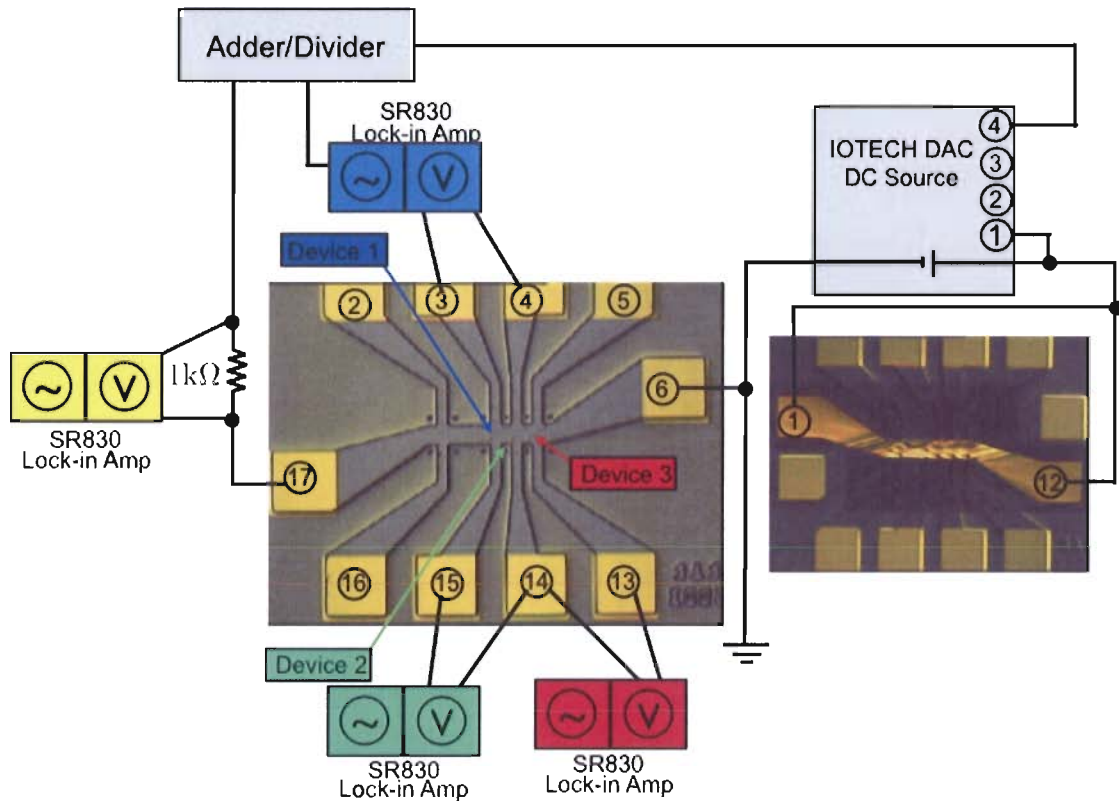
Figure 5.14.. Measurement schematic for the applied bias measurements

Prior investigations of an applied bias to a billiard have established that if the condition $eV_{bias} \ll k_B T$ holds then the properties of the conductance remain in the linear response or low bias regime [18]. In this regime, Ohms law holds and current is linear with conductance $I = GV$. However relaxing this constraint can result in the introduction of nonlinear terms in conductance also known as non equilibrium effects [67, 68]. While in the linear response, the effect of small bias voltages is mainly that

of electron heating which can be modeled by balancing the Joule heating due to the current with the cooling power of the low temperature ohmic contacts [67]. This effective temperature can then be written as [67, 68]:

$$T_e = \frac{1}{2}T_L + \frac{1}{2}\sqrt{T_L^2 + \frac{3}{2\pi^2}e^{-\gamma\tau_\phi}(\frac{eV_b}{k_B})^2} \qquad (V.13)$$

Here T_L is the lattice temperature of the sample. The exponential term represents the portion of electrons that have time to thermalize with their surroundings before leaving the billiard. In this exponential term, τ_ϕ is the phase breaking time that is obtainable through the correlations field analysis discussed in Chapter II. The escape rate is given by γ such that electrons that are able escape quickly (large γ) do not contribute to heating. If γ is sufficiently large, then the expression reduces to T_L and the applied bias (V_B) has no heating effect on the billiard.

The effects of an applied bias to the MCF in the square billiard on sample H1 can be seen in Fig. 5.15. The bottom (blue) trace is a base temperature trace with $V_{bias} = 0$ mV. The trace above that was taken with the lattice temperature raised to 2K and no bias applied. The middle (dark purple) trace was taken with the sample at base temperature and V_{bias} set to 3mV. This results in an effective temperature of $T_e = 3$K and the traces exhibit similar smearing of the small feature conductance fluctuations. The next red trace (second from the top) was taken with $T_L = 8$K and no applied bias. In contrast, the top trace was taken at base temperature and the bias voltage was set to -7mV. This corresponds to $T_e = 8.2$K and yet the traces are

markedly different. There appears to be much more high frequency fluctuations in the top (orange) trace. This seems to indicate that a departure from the linear response.
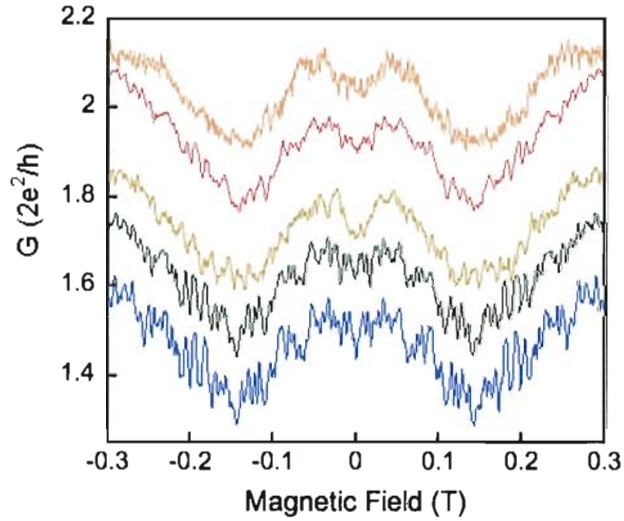

Figure 5.15. Increased bias voltage has a similar effect on the MCF as increased temperature.

To investigate this further, the left panel of Fig. 5.16 plots both the effective temperature as well as the phase breaking time against the magnitude of the applied bias voltage. The left axis corresponds to the blue T_e data points, as expected by the form of Eq. V.13 , T_e follows a linear trend with V_{Bias}. The right axis corresponds to the red data point that represent the values of τ_ϕ obtained through the correlations field analysis. The error bars in τ_ϕ are a result of the inherent scatter of the $B_c vs. B$ plot on which that analysis depends. Despite the scatter, τ_ϕ seems to have a decreasing trend with increasing V_{bias} which is also expected if the electrons are able to thermalize within the billiard. It appears that neither of these parameters are independently sensitive to non-equilibrium effects apparent in the MCF when plotted against V_{bias}.
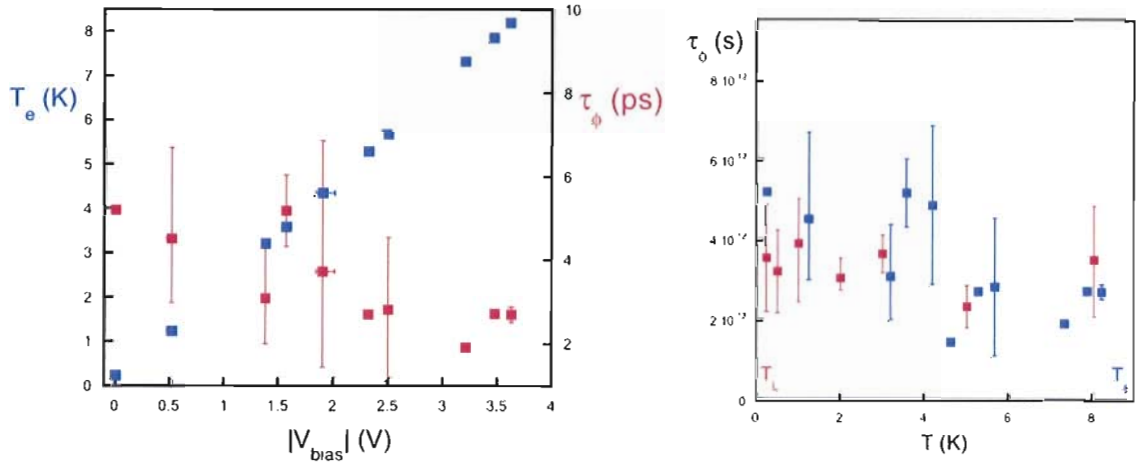
Figure 5.16. Left:Effective temperature (blue squares, left axis) and phase breaking time(red squares, right axis) plotted against the magnitude of the applied bias voltage. Right: Phase breaking time plotted against Lattice (red) and effective (blue) temperatures.

The right hand panel of Fig. 5.16 plots τ_ϕ against both effective and lattice temperatures. This plot does not seem to indicate a transition to non linear behavior. However, it does indicate that an increase in both T_L plotted in red and T_e plotted in blue lead to a decrease in τ_ϕ which matches intuition. It could be argued that the overall decreasing trend in the T_e phasebreaking times is slightly steeper than those corresponding to T_L, thus indicating that V_{bias} is doing more than just increasing electron temperature. However, this argument does not carry substantial weight due to the large error associated with the measurement of τ_ϕ.

If the only function that an applied bias voltage plays is to increase the temperature, then it should not influence the MCF as seen in Fig. 5.15. This indicates that the 'universal' parameter Q should be enlisted to chart the α values of the V_{bias} MCF traces. Equation III.1 introduced Q as:

$$Q = \frac{\Delta E_S}{\Delta E_B} = \frac{2\pi \hbar^2/m^* A}{\sqrt{(\hbar/\tau_\phi)^2 + (k_B T)^2}} \qquad \text{(V.14)}$$

To evaluate Q for the V_{Bias} measurements T_e must be used in place of T. The data previously taken to construct the Q curve (i.e. in the linear response) is plotted in the right hand panel of Fig. 5.17, This is the same data set plotted in Fig. 3.7. The region indicated by the ellipse indicates the region that has been magnified in the left panel.
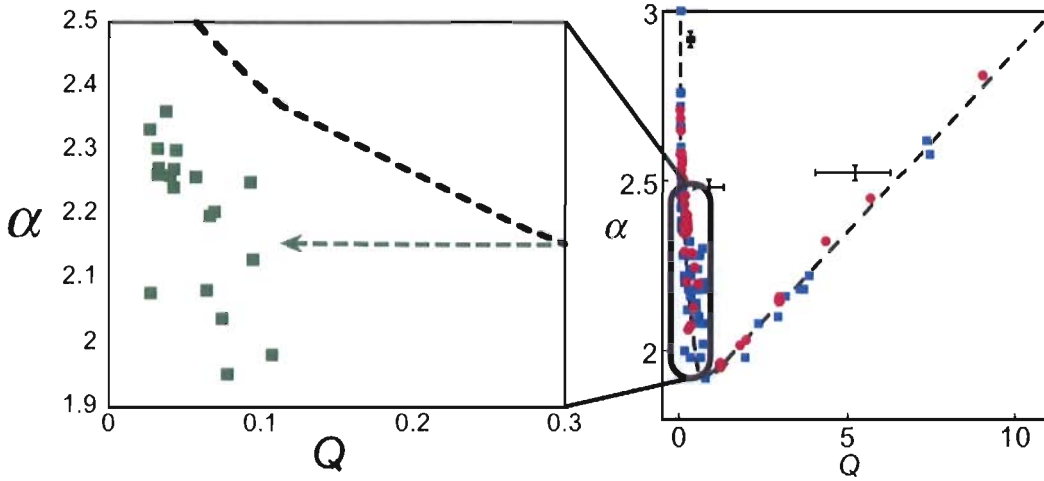
Figure 5.17. α shows a departure from Q in the high bias regime, indicating a high bias effects alpha in a non trivial way.

The left panel of Fig. 5.17 indicates that α, when plotted against Q, is sensitive to the transition to non-linear response. While only the MCF from the square billiard were shown in Fig. 5.15, the α values plotted on the left panel represent all three of the billiards that were on the Hall bar labeled H1. Not only the square billiard, but both the LR and UD triangles α values depart from Q when those billiards

are exposed to a high bias voltage. These are the same billiards that were used to construct the Q curve in Fig. 3.3 that was shown in Chapter III. This departure from Q indicates that application of a high bias effects the MCF in a non-trivial manner. It is recommended that a future student carries on with this investigation, including if possible a replication of this experiment to ensure that these results are reproducible.

Conclusions

This chapter investigated a billiards sensitivity to external fields, as charted by D_F. FCF were produced by both electric as well as magnetic fields. Using an autocorrelation analysis, it was shown that FCF associated with high D_F values tend to be more sensitive to external fields. That is to say that the FCF associated with high D_F values de-correlated at smaller increments of the applied field than the FCF associated with low D_F values. The results of Ch. IV indicate that the FCF will arise in any device with impurities. Coupling that with the results of this chapter seem to imply the possibility of using these devices or at least the FCF as a novel sensor of external fields. The sensitivity could be tuned via D_F by perhaps engineering devices that yield the desired range of D_F. For instance, if the FCF are to be used as a sensor, a high D_F would be desired. On the other hand, if the goal is the suppression of the FCF due to external fields, low D_F devices would be indicated.

The application of a high bias voltage led to a departure from the Q curve that is not understood. It is recommended that a future student carries on with this

investigation, including if possible a replication of this experiment to ensure that these results are reproducible. It would be worthwhile to further probe the consequences of this non-trivial effects on the FCF in the presence of an applied bias.

CHAPTER VI

CONCLUDING REMARKS

The central question of this dissertation is: what is the underlying cause of *Fractal Conductance Fluctuations* (FCF) observed in semiconductor devices ? As an answer, it was proposed that scattering from impurities in the material produced a mix of stable and chaotic electron trajectories within the confines of the device. Multiple reflections off the device walls are induced, leading to repeated traversals through the confined region of the device. Repetition of the trajectories continues until the electron can finally escape the device through the exit QPC. The production of a mixture of stable and chaotic trajectories is crucial to the development of fractal conductance fluctuations, and is based on the theoretical predictions of Ketzmerick[12]. Chapter I provided background information on fractal geometry, including a demonstration of the link between chaos and perhaps the most famous of mathematically generated fractals, the Mandelbrot set. This link was then shown to be physically realisable with an experiment involving a three dimensional Sinai billiard. In this 'Sinai cube', rays of light were spectrally reflected off of mirrored surfaces. It was shown that the fractal dimension, D_F, of the resulting pattern of light rays was dependent only on the light's ability to escape the billiard, which was charted as the 'openness' of the billiard.

Following a brief overview of the relevant physics pertaining to the fabrication and measurement of the analogous electronic billiards in Chapter II, magnetoconductance fluctuations (MCF) were shown to arise from a quantum interference effect that results from exposing the billiard to a varying external magnetic field. The Fourier deconstruction of the frequencies contributing to the MCF were shown to be well characterized by the spectral exponent α. The overview included relating α to D_F through the expression $\alpha = 5 - 2D_F$. Chapter III investigated the quantum chaos of the Sinai billiard, and showed that the chaos necessary to produce the FCF was not limited to device geometries that were classically chaotic. Charting α with the empirical parameter $Q = \dfrac{\Delta E_S}{\Delta E_B}$ illuminated flaws in predictions that the FCF would rely on billiard geometry, potential profile, and the severity of material induced scattering.

This led to our proposal that remote, or modulation, doping produces the necessary chaos via ionized impurities. The ionized impurities alter the potential landscape, and produce small angle scattering that is iterated by reflections off the billiard walls. Chapter IV focused on an experiment designed to test this proposal. It was shown that warming the billiard to ~120 K provided sufficient thermal energy to redistribute the charge configuration within the doping layer of the heterostructure. The redistribution of the precise charge configuration led to alterations in fine scale features of the MCF while leaving the overall statistics, as measured by D_F, unchanged. This provided strong support for the altered potential landscape model, in which

the remote ionized donors act as nanoscopic Sinai diffusers, promoting small angle scattering that is then amplified through iteration by reflections off of the billiard walls. Finally, Chapter V investigated the sensitivity of FCF to external fields as monitored by D_F.

The underlying theme of this dissertation is the following model. Remote ionized donors alter the potential landscape encountered by the electrons as they traverse the billiard. The ionized donors act as Sinai diffusers, producing small angle scattering of the electron trajectories. This scattering generates iterated chaos due to repeated reflections off of the billiard walls. Each reflection off a billiard wall redirects the electron through the roughened terrain, where small angle scattering is repeated. In this picture, if the scatterers are 'hard' (i.e. in plane) stable trajectories do not interact with the scatterers and are thus able to escape the billiard after a small number of reflections. However, if the scatterers are 'soft' (i.e. remote) then both stable and chaotic trajectories are generated [12, 33]. It is the trajectories that encounter a large number of small angle scattering events that are chaotic and tend to undergo more reflections and thus the chaos is iterated. Quantum interference between electron wavefunctions flowing along the mixture of the stable and chaotic trajectories then results in fluctuation in the conductance that are fractal. The results presented in chapters III, IV and V is strongly supportive of this model.

This model predicts that if one were able to fabricate a billiard that is truly 'clean', in the sense that the 2DEG potential landscape was smooth, any conductance

fluctuations that arose would NOT be fractal. This implies that a real test of this model lies in the fabrication and measurement of an 'ultra clean' billiard. Our collaborators at the University of New South Wales in Sydney, Australia have done just that [69, 70]. MCF were measured and a preliminary data set was supplied to us for fractal analysis which was completed literally days ago at the time of this writing. Figure 6.1 schematically shows the heterostructure used by our collaborators. Above the undoped GaAs substrate (yellow) sits a 160 nm undoped layer of AlGaAs(green). A 2DEG forms at the interface. Above the AlGaAs layer is a highly doped GaAs cap layer (35 nm) used as a gate. This layer is degenerately doped, producing a high enough electron density to screen the 2DEG from ionized cap layer impurities, providing metallic conductivity at low temperatures[69], leaving the 2DEG with a smooth potential landscape. The dashed line in the GaAs cap layer indicates a 25 nm spacer of undoped GaAs which provides further screening.
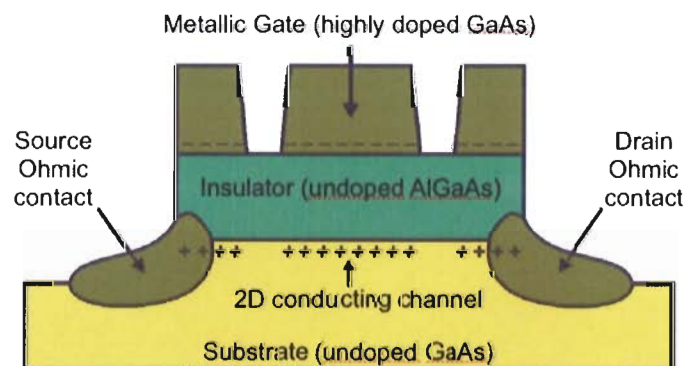

Figure 6.1. Schematic of the heterstructure used for a billiard fabricated without modulation doping by collaborators in Sydney, Australia.

Billiard definition was obtained using electron beam lithography and wet etching which formed $\sim$ 45 nm deep trenches in the GaAs cap layer. This separated the cap into seven regions, each of which was used as a separate gate[69]. An atomic force micrograph of the billiard is provided in Fig. 6.2. The billiard dimensions are $0.74 \times 0.66\,\mu m^2$. The source and drain QPC's are roughly $0.5\,\mu m$ wide, providing an entrance and exit for current to flow through the billiard. In this billiard, electrons are electrostatically induced into the channel by the application of a positive voltage to the 'metalic' gate. The induction process is similar to the action of a parallel plate capacitor. Electrons form a 2D sheet whose density can be tuned by the applied gate voltage. Note that this is a rectangular, hard walled billiard, free from material induced impurities, and thus should support only stable electron dynamics.
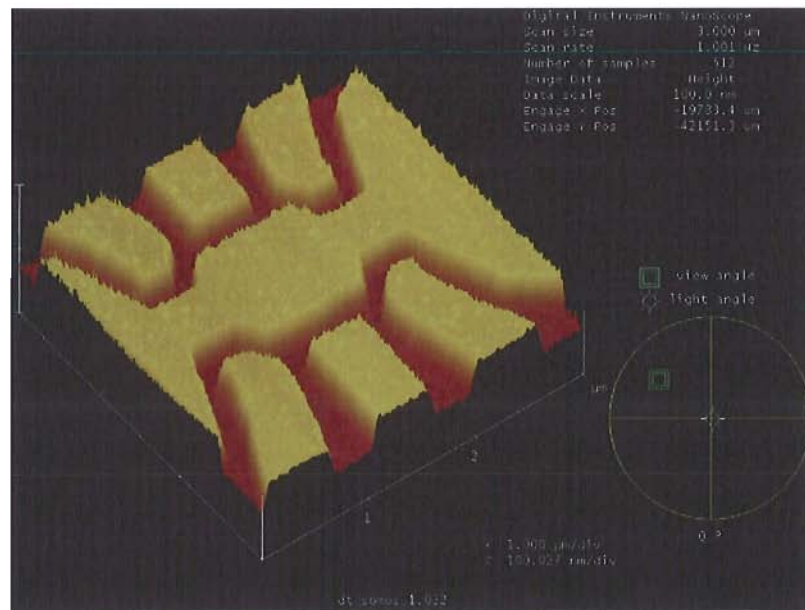

Figure 6.2. AFM image of the high mobility billiard fabricated without modulation doping by collaborators in Sydney Australia.

Figure 6.3 shows an example of the preliminary data trace provided to us by our collaborators. This data set was obtained by measuring the current through the billiard using lock-in techniques with a 20μV AC signal. The magnetic field was swept at a rate of 0.01T/minute and the temperature, using a dilution refrigerator, was 40 mK.
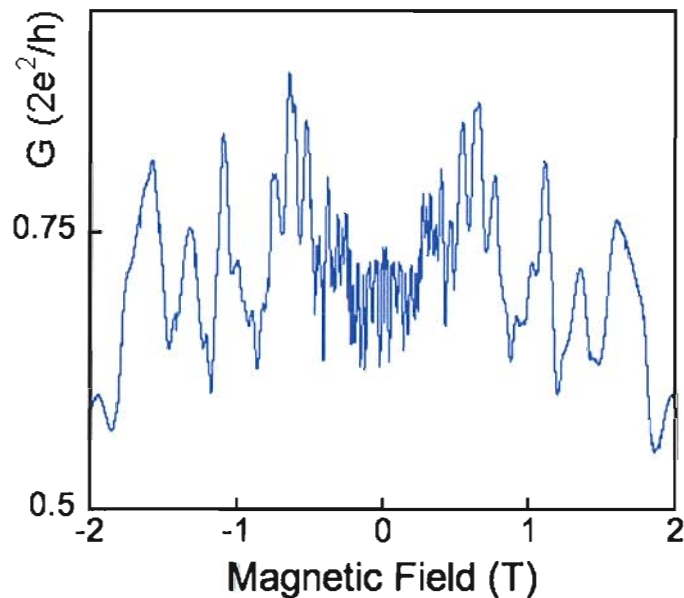
Figure 6.3.. Magneto conductance fluctuations in the undoped billiard

The observed fluctuations in conductance are not fractal, as illustrated by Fig. 6.4. The left hand side of Fig. 6.4 shows the results of the variational method box count analysis performed on the data set in Fig. 6.3. The vertical dashed lines indicate the cutoffs for this scaling plot. The orange line indicates the cutoff associated with the smallest observeable feature of the MCF, and corresponds to the lower cutoff

(previously refered to as B_L). The purple dashed line corresponds to the upper cutoff (B_U) and is determined by the statistical constraint of having no less than 49 boxes covering the trace during a box-count.[1] The brown dashed line represents the limit of five times the data resolution, based on the assumption that at least 5 data points are needed to distinguish a complete period of an oscillation. The data resolution cutoff is displayed for two reasons. First, B_L occurs well before the data resolution limit. Additionally any data that is analyzed with box sizes smaller than the data resolution will result in scaling that produces a D value of 1. The blue line in the left hand panel of Fig. 6.4 is a fit to $D = 1$ and the green line is a fit to $D = 2$. The region of this plot between B_L and B_U spans nearly two orders of magnitude. However, the data within this region does not follow a linear trend for even one order of magnitude, which is the minimal range of scaling required for an object to be considered fractal [5].

For contrast, the right hand panel of Fig. 6.4 shows a scaling plot of the square billiard of sample H3's MCF. In this scaling plot, the data follows a linear trend for $\sim$ 1.5 orders of magnitude, nearly the entire range between B_L and B_U. The blue line in that plot is a fit to $D_F = 1.4$. To emphasize this difference, Fig. 6.5 shows the same scaling plot of the undoped square billiard's MCF, truncated to the region between B_L and B_U. The blue and green lines are the same as those used in Fig. 6.4. The black line is a ploynomial fit to the data, emphasizing the curvature of the data set within

---

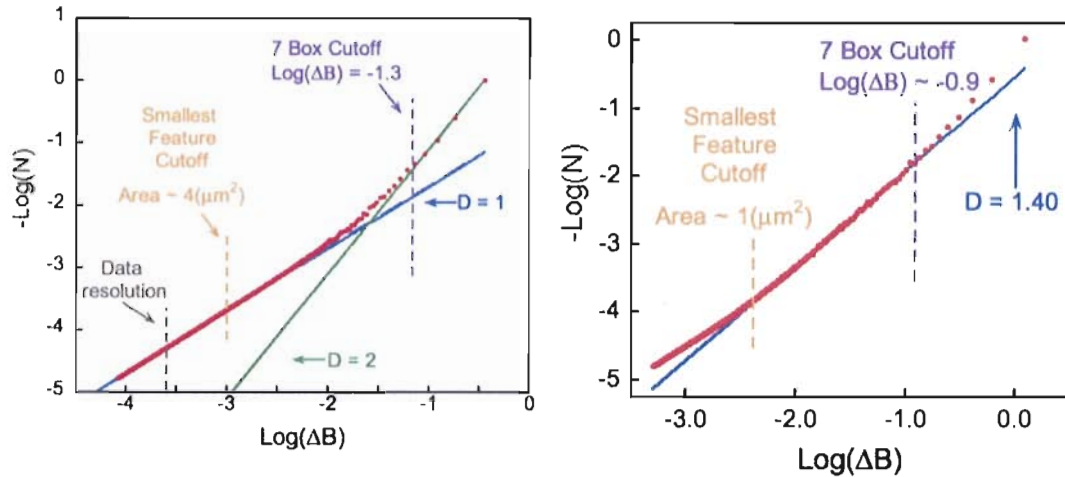[1] A square 7x7 grid will contain 49 boxes, thus the label 7 box cutoff

Figure 6.4. Left: Scaling plot of the udoped square billiard's MCF. Dashed lines indicate the associated cutt-offs. The blue line is a linear fit in which $D = 1$, the green line is a fit to $D = 2$. Right: Scaling plot of the square billiard H3's MCF. This billiard was defined by etching the GaInAs/InP heterostructure, the blue line is a fit to $D_F = 1.4$.

the cutoffs. Figure 6.5 illustrates that the scaling plot is gradually transitioning from the $D = 1$ value arising from box sizes that are smaller than the data resolution, to $D = 2$ arising from box sizes that are too large, and thus are all filled. This data does not follow a linear trend anywhere within the measurement range and thus, the MCF corresponding to this scaling plot are not fractal.

It should be re-emphasized that the above was based on a preliminary data set. Our collaborators provided us with two data sets, both of which reveal the same non-fractal scaling plots. However, this is only two data sets taken on one billiard. Thus any conclusions must be drawn cautiously. Nonetheless, it certainly appears that these 'ultra-clean' billiards do not have the roughened potential terrain
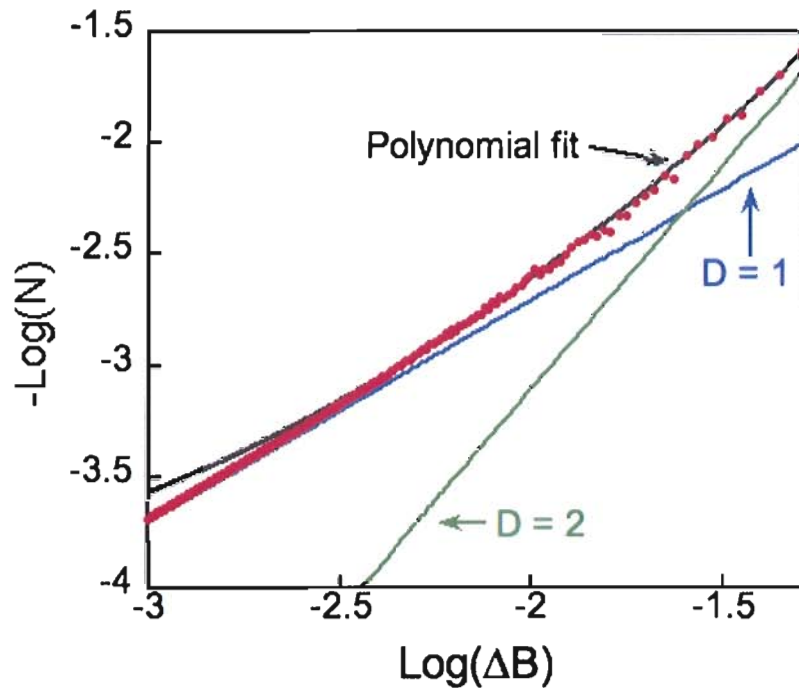
Figure 6.5. Close-up of the undoped billiard scaling plot. Scaling plot of the undoped square billiard's MCF over the region within B_U and B_L. The blue (green) line is the same fit to $D = 1(2)$ used in Fig. 6.4. The black line is a polynomial fit to the data emphasizing the curvature in the transition between $D = 1$ to $D = 2$.

that accompanies modulation doping. If there are any impurities present, they do not produce the same effect as the ionized impurities that are an artifact of modulation doping. Without the small angle scattering produced by the remote ionized impurities, the conductance fluctuations that arise are not fractal. This lends considerable support to the proposal that these ionized impurities act as Sinai scatterers, leading to chaotic trajectories. Further experimentation on these systems is warranted, and the undoped billiards should be subjected to the temperature cycling experiment described in Ch. IV. The temperature cycling experiment will further

aid in determining if impurities are present. Such an experiment is planned within the next couple of months, when our collaborators supply us with the billiards. As discussed in Ch.V, further investigation into high bias voltages leading to α values that depart from Q is also warranted and slated for experimentation during the same cool down. That being said, when coupled with the preliminary data recently provided by our collaborators, the results presented in this dissertation offers a comprehensive description of how chaotic electron transport in diffusive, quasiballistic and ballistic semiconductors lead to conductance fluctuation that are fractal.

REFERENCES

[1] Y. G. Sinai, Russian Mathematical Surveys **25** (1970).

[2] S. Bleher, C. Grebogi, E. Ott, and R. Brown, Phys. Rev. A **38**, 930 (1988).

[3] B. B. Mandelbrot, *The Fractal Geometry of Nature* (W. H. Freeman and Company, New York, 1983).

[4] H.-O. Peitgen, H. Jürgens, and D. Dietmar Saupe, *Chaos and Fractals* (Springer-Verlag, New York, 1992).

[5] D. Avnir, O. Biham, D. Lidar, and O. Malcai, Science **279**, 39 (1998).

[6] R. L. Zimmerman and F. I. Olness, *Mathematica for Physics* (Addison-Wesley, New York, 2002).

[7] T. Lei, Commun Math Phys. **134**, 587 (1990).

[8] J. C. Sprott, *Chaos and Time Series Analysis* (Oxford University Press Inc, New York, 2003).

[9] R. M. May, Nature **261**, 459 (1976).

[10] E. N. Lorenz, J. Atmos Sci. **20**, 130 (1963).

[11] J. Gleick, *Chaos Making a New Science* (Penguin Books, New York, 1987).

[12] R. Ketzmerick, Phys Rev B **54**, 10841 (1996).

[13] E. Ott, *Chaos In dynamical Systems* (Cambridge University Press, New York, 2002).

[14] H. van Beijeren, Rev. Mod. Phys. **54**, 195 (1982).

[15] J. Y. D. Sweet, E. Ott, Nature **399**, 315 (1999).

[16] K. Amano, D. Narimatsu, S. Sotome, S. Tashiro, A. Uchida, and S. Yoshimori, Phys. Rev. E **76**, 046213 (2007).

[17] C. Bercovich, U. Smilansky, and G. Farmelo, European Journal of Physics **12**, 122 (1991).

[18] S. Datta, *Electronic Transport in Mesoscopic Systems* (Cambridge University Press, New York, 1995).

[19] J. H. Davies, *The Physics of Low Dimensional Semiconductors* (Cambridge University Press, New York, 1998).

[20] N. W. Ashcroft and N. D. Mermin, *Solid State Physics* (Brooks/Cole Thomson Learning Inc., New York, 1976).

[21] T. P. Martin, Ph.D. thesis, University of Oregon (2006).

[22] T. P. Martin, C. A. Marlow, L. Samuelson, A. Hamilton, H. Linke, and R. Taylor, Physical Review B **77**, 155309 (2008).

[23] Y. Aharonov and D. Bohm, Phys. Rev. **115**, 485 (1959).

[24] R. Landauer, *Nonlinearety in Condensed Matter* (Springer-Verlag, Berlin, 1987), ed. Trullinger, S. E.

[25] B. L. Al'tshuler and D. E. Khmelnitskii, JETP Letters **42**, 360 (1986).

[26] K. Falconer, *Fractal Geometry* (John Wiley and Sons Ltd, West Sussex, 2003).

[27] D. C. Agnew, Geophys Res Lett **10**, 333 (1992).

[28] A. P. Micolich, R. P. Taylor, A. G. Davies, J. P. Bird, R. Newbury, T. M. Fromhold, A. Ehlert, H. Linke, L. D. Macks, W. R. Tribe, et al., Phys. Rev. Lett. **87**, 036802 (2001).

[29] C. A. Marlow, R. P. Taylor, T. P. Martin, B. C. Scannell, H. Linke, M. S. Fairbanks, G. D. R. Hall, I. Shorubalko, L. Samuelson, T. M. Fromhold, et al., Phys. Rev. B **73**, 195318 (2006).

[30] C. M. Marcus, R. M. Westervelt, H. P.F., and A. Gossard, Physical Review B **48**, 2460 (1993).

[31] B. Hackens, F. Delfosse, S. Faniel, C. Gustin, H. Boutry, X. Wallart, S. Bollaert, A. Cappy, and V. Bayot, Phys. Rev. B **66**, 241305 (2002).

[32] C. M. Marcus, A. J. Rimberg, R. M. Westervelt, H. P.F., and A. Gossard, Phys Rev Lett **69**, 506 (1992).

[33] A. S. Sachrajda, R. Ketzmerick, C. Gould, Y. Feng, P. J. Kelly, A. Delage, and Z. Wasilewski, Phys. Rev. Lett. **80**, 1948 (1998).

[34] R. P. Taylor, R. Newbury, A. S. Sachrajda, Y. Feng, P. T. Coleridge, C. Dettmann, N. Zhu, H. Guo, A. Delage, P. J. Kelly, et al., Phys. Rev. Lett. **78**, 1952 (1997).

[35] T. M. Fromhold, C. R. Tench, R. P. Taylor, A. P. Micolich, and R. Newbury, Physica B: Condensed Matter **249-251**, 334 (1998).

[36] J. A. Nixon, J. H. Davies, and H. U. Baranger, Phys. Rev. B **43**, 12638 (1991).

[37] M. A. Topinka, B. J. LeRoy, S. E. J. Shaw, E. J. Heller, R. M. Westervelt, K. D. Maranowski, and A. C. Gossard, Science **289**, 2323 (2000).

[38] M. A. Topinka, B. J. LeRoy, R. M. Westervelt, S. E. J. Shaw, R. Fleischmann, E. J. Heller, K. D. Maranowski, and A. C. Gossard, Nature **410**, 183186 (2001).

[39] M. A. Topinka, R. M. Westervelt, and E. J. Heller, Physics Today **56**, 47 (2003).

[40] J. P. Bird, K. Ishibashi, Y. Ochiai, M. Lakrimi, A. D. C. Grassie, K. M. Hutchings, Y. Aoyagi, and T. Sugano, Phys. Rev. B **52**, 1793 (1995).

[41] C. V. Brown, A. K. Geim, T. J. Foster, C. J. G. M. Langerak, and P. C. Main, Phys. Rev. B **47**, 10935 (1993).

[42] K. Ishibashi, K. Nagata, K. Gamo, S. Namba, S. Ishida, K. Murase, M. Kawabe, and Y. Aoyagi, Solid State Communications **61**, 385 (1987).

[43] K. Ishibashi, Y. Takagaki, K. Gamo, S. Namba, S. Takaoka, K. Murase, S. Ishida, and Y. Aoyagi, Journal of Vacuum Science & Technology B: Microelectronics and Nanometer Structures **6**, 1852 (1988).

[44] R. P. Taylor, M. L. Leadbeater, G. P. Whittington, P. C. Main, L. Eaves, S. P. Beaumont, I. McIntyre, S. Thoms, and C. D. W. Wilkinson, Surface Science **196**, 52 (1988).

[45] A. K. Geim, P. C. Main, P. H. Beton, L. Eaves, S. P. Beaumont, and C. D. W. Wilkinson, Phys. Rev. Lett. **69**, 1248 (1992).

[46] C. W. J. Beenakker and H. van Houten, *in Solid State Physics (eds. Ehrenreich, H. & Turnbull, D.)* (Academic Press, Boston, 1991).

[47] J. Klem, W. T. Masselink, D. Arnold, R. Fischer, T. J. Drummond, H. Morkoç, K. Lee, and M. S. Shur, Journal of Applied Physics **54**, 5214 (1983).

[48] D. K. Maude, J. C. Portal, L. Dmowski, T. Foster, L. Eaves, M. Nathan, M. Heiblum, J. J. Harris, and R. B. Beall, Phys. Rev. Lett. **59**, 815 (1987).

[49] R. P. Taylor, R. Newbury, R. B. Dunford, P. T. Coleridge, A. S. Sachrajda, and J. A. Adams, Phys. Rev. B **51**, 9801 (1995).

[50] D. Zwillinger and E. i. Chief, *Standard Mathematical Tables and Formulae* (CRC Press LLC, Florida, 1996).

[51] R. A. Jalabert, H. U. Baranger, and A. D. Stone, Phys. Rev. Lett. **65**, 2442 (1990).

[52] D. N. Armstead, B. R. Hunt, and E. Ott, Phys. Rev. E **67**, 021110 (2003).

[53] J.-P. Bouchaud, A. Georges, J. Koplik, A. Provata, and S. Redner, Phys. Rev. Lett. **64**, 2503 (1990).

[54] G. M. Schlesinger, G. M. Zaslavsky, and U. Frisch, *Lévy Flights and Related Topics in Physics* (Springer-Verlag, 1995).

[55] R. Crook, C. G. Smith, A. C. Graham, I. Farrer, H. E. Beere, and D. A. Ritchie, Phys. Rev. Lett. **91**, 246803 (2003).

[56] D. A. Wharam, T. J. Thornton, R. Newbury, M. Pepper, H. Ahmed, D. G. Frost, J. E. F.and Hasko, D. C. Peacock, D. A. Ritchie, and G. A. C. Jones, J. Phys C **21**, L209 (1988).

[57] B. J. van Wees, H. van Houten, C. W. J. Beenakker, J. G. Williamson, L. P. Kouwenhoven, D. van der Marel, and C. T. Foxon, Phys. Rev. Lett. **60**, 848 (1988).

[58] D. K. Ferry and S. M. Goodnick, *Transport in Nanostructures* (Cambridge University Press, New York, 1997).

[59] A. P. Micolich, R. Taylor, A. G. Davies, J. B. Bird, R. Newbury, T. Fromhold, A. Ehlert, H. Linke, L. D. Macks, W. R. Tribe, et al., Phys Rev Lett **87**, 036802 (2001).

[60] P. M. Mooney, J. Appl. Phys **67**, R1 (1990).

[61] E. Calleja, A. Romero, S. Fernández de Avila, and E. Muñoz, Semicond. Sci. Technol **8**, 206 (1993).

[62] P. M. Mooney, J. Appl. Phys **67**, R1 (1990).

[63] P. Viktorovitch, Journal of The Electrochemical Society **136**, 1431 (1989).

[64] R. B. Beall, J. B. Clegg, J. Castagnè, J. J. Harris, R. Murray, and N. R. C., Semicond.Sci. Technol **4**, 1171 (1989).

[65] D. Inoue, S. Matsushita, K. Matsumura, M. Sawada, K. Yodoshi, and Y. Harada, Solid-State Electronics **41**, 1475 (1997), proceedings of the Topical Workshop on Heterostructure of Microlectronics.

[66] P. A. Lee, A. D. Stone, and H. Fukuyama, Phys. Rev. B **35**, 1039 (1987).

[67] J. P. Bird, H. Linke, J. Cooper, A. P. Micolich, D. K. Ferry, R. Akis, Y. Ochiai, R. P. Taylor, R. Newbury, P. Omling, et al., physica status solidi (b) **204**, 314 (199y).

[68] M. Switkes, A. G. Huibers, C. M. Marcus, K. Campman, and A. C. Gossard, Applied Physics Letters **72**, 471 (1998).

[69] A. M. See, O. Klochan, A. R. Hamilton, A. P. Micolich, M. Aagesen, and P. E. Lindelof, Applied Physics Letters **96**, 112104 (2010), 1003.0240.

[70] O. Klochan, J. C. H. Chen, A. P. Micolich, A. R. Hamilton, K. Muraki, and Y. Hirayama, Applied Physics Letters **96**, 092103 (2010), 1002.2998.